PhD in Astronomy, Astrophysics and Space Science
XXXVI cycle

Planetary environments: exosphere modelling and a new particle detection study

Supervisors
Dr. Anna Milillo
Dr. Elisabetta De Angelis
Dr. Alessandro Mura
Prof. Dario Del Moro

Canditate
Martina Moroni

A. A. 2022/2023

Alla mia famiglia e
a tutti voi che mi avete
sempre supportato e sopportato

Abstract

The thesis presents a study of the Mercury and Earth exospheres. For Mercury, we study and model the source and loss processes of the exosphere and compare the simulation results with observational data. For the Earth, we focus on the investigation of interactions between the plasma and Earth's exosphere using the Energetic Neutral Atom (ENA) imaging technique, studying and testing a new ENA detector generation.
We use the 3D Monte Carlo model of the Hermean exosphere from *Mura et al. (2007)* to investigate Mercury's exosphere. In detail, we upgrade the model to better describe the Micro-Meteoroids Impact Vaporization (MMIV) process as source of Mercury's Ca. The in-situ observations of Mercury's Ca exosphere, performed during the MESSENGER/NASA mission, exhibited very high energies, with a scale height consistent with a temperature $> 50{,}000$ K, originated mainly on the dawn-side of the planet. It was suggested that the originating process is due to MMIV, but previous estimations were not able to justify the observed intensity and energy. The most likely origin of this exospheric element may be a combination of different processes involving the release of atomic and molecular surface particles. We simulate the 3-D spatial distribution of the Ca-bearing molecule and atomic Ca exospheres generated through the MMIV process including the meteor stream contribution from comet 2P/Encke. We show that the morphology and intensity of the Ca exosphere are consistent with the available MESSENGER observations if we consider a cloud quenching temperature < 3750 K. The comet contribution seems to be underestimated and requires further investigations. Our results can be useful in the exospheric studies and in the interpretation of active surface release processes, as well as in the exosphere observations planning for the ESA-JAXA BepiColombo mission that will start its nominal mission phase in 2026.
With the aim to have a complete picture of the solar wind-magnetosphere-exosphere interactions in the Earth's environment, we investigate the expected ENA signals for a possible instrument on board a LEO spacecraft. We focus on the gas detector, used for the first time for ENA applications, and realize a model to simulate the sensor baseline and its performance. A prototype of this new generation ENA detector for space instruments has been tested in Ion-ENA beam facility at the IAPS (Institute for Space Astro-

physics and Planetology) in Rome, demonstrating the capability of our setup to detect ions and ENA particles in a low energy range at low pressure. The successful demonstration of the feasibility of this innovative instrument for ENA/Ion detection makes it extremely attractive for a future space mission.

Contents

Introduction

The exosphere is a thin gaseous atmospheric layer that surrounds a planet or natural satellite where atoms and/or molecules are gravitationally bound, but where the gas density is so low that the particles are collision-less.
The lower limit of an exosphere is the boundary between collisional and non-collisional regimes, usually called exobase. It is defined as the altitude where the mean free path of atmospheric constituents, i.e. the average length of a path covered by a particle between subsequent collisions *(Hastings and Garrett 1996)*, is equal the scale height, the height where density decrease by a factor 1/e from the value at the surface in an isothermal atmosphere *(Chapman and Cowling 1952)*.
Planetary exospheres are built up by three different populations of particles *Chamberlain (1963)*: those that travel on ballistic orbits returning to the atmosphere through the exobase, those that are in quasi-trapped satellite orbits and those that are escaping. The latter are generated when the kinetic energy provided by the collisions goes up to the escape energy, allowing the particles to overcome the planetary gravitational field and be lost in space.
On planets with dense atmospheres, such as the Earth, the exosphere is the uppermost atmospheric layer, where the gas density becomes lower and lower. However, there are several bodies in the Solar System that do not have dense atmospheres. Natural satellites like the Moon and low gravity close-in planets like Mercury have an exosphere without a denser collisional atmosphere underneath. In these cases the exospheres are called 'surface-bounded exospheres', because directly in contact with the surface. The study of the origin of the exospheric particles, the relevant physical source processes, and their loss from the exosphere into interplanetary space provides important clues on Sun to planet interaction and on planetary evolution, that are fundamental

to understanding the current state of the Solar System.
A full characterization of the environment requires a comprehensive study of the exosphere under different conditions, using a variety of instrumental techniques, systematic observations and different models.
The aim of this work is to study the two main cases of the exospheres of Mercury and Earth. On the one hand, we study and model the generation and loss processes of Mercury's exosphere, showing the simulation results that will be compared with observational data. On the other hand, we investigate the applications of the neutral atom imaging to the environments of Earth, studyng and testing a new generation of detectors and showing the main laboratory results obtained during the activity carried out at the IAPS (Institute for Space Astrophysics and Planetology) of Rome.
Mercury's exosphere is continuously refilled and depleted through processes acting both on the surface and within the planet's environment *(Milillo et al. 2005; 2020)*. The surface release processes are strongly driven by external factors such as the solar irradiance, the solar wind, solar energetic particles (SEPs) and the micrometeoroid flux precipitating onto the surface, as well as internal factors like the planet's physical and chemical properties. Several Earth-based telescopes have provided evidence of the highly variability of Mercury's Na exosphere. There have been several dedicated space missions from Mariner 10 between 1974 and 1975 to the NASA/MESSENGER (MErcury Surface, Space ENvironment, GEochemistry, and Ranging) mission. MESSENGER visited Mercury in the period 2008-2015, providing in-situ measurements of Mercury's exosphere and allowing the study of the seasonal variations of metals such as Mg and Ca. The mission added a consistent amount of data, but a global description of the planet's exosphere is still not available. The ESA BepiColombo mission will study Mercury orbiting around the planet from 2025. For this reason, it is important to have a modelling tool ready for interpreting observational data and for testing different hypothesis on the release mechanisms.
In order to study Mercury's environment, we simulate the Na and Ca exospheres, discuss the different exospheric processes responsible for these elements and compare the different exospheric spatial distributions. The exospheric Monte Carlo model by *Mura et al. (2007)* used in this study includes a combination of different exospheric source and loss processes, such as the release of atomic and molecular surface particles and the photodissociation of exospheric molecules and provides simulations of distribution of atomic and molecular exospheric components. We reproduce the spatial distribution of

the Na exosphere starting from the same model assumptions as in *Mura et al. (2007)*, and then we modify the model with the scope to provide a refined 3-D density distribution of Mercury's Ca and CaO exospheres generated through meteoroid impacts.
Furthermore, in the idea that there are different approaches to study planetary exosphere, we also study the remote sensing of Energetic Neutral Atoms (ENA) resulting from the interactions between plasma and planet exosphere. ENA measurements are recognized as a powerful tool to remotely study various global plasma phenomena in space. At the end of '80, ENA imaging opened a new window on space plasmas investigation with a promise to qualitatively improve our understanding of global magnetospheric and heliospheric processes.
We study and model the ENA sources in the Earth's environment, with the aim of obtaining a complete picture of the solar wind-magnetosphere-ionosphere interactions and analysing the expected ENA signals for a possible instrument on board a LEO spacecraft. We focus on the gas detector, used for the first time for ENA applications, and realize a model to simulate the sensor baseline and its performance. A prototype of this new generation ENA detector for space instruments has been tested in Ion-ENA beam facility at IAPS, demonstrating the capability of our setup to detect ions and ENA particles in a low energy range at low pressure.
The thesis is organized as follows: in Chapter 1 we look at the characterization of different kind of planetary exospheres in the cases of Mercury and Earth. We study Mercury's exosphere in Chapters 2 and 3: in the former we provide details on the source and loss processes of the exosphere; in the latter we discuss the morphology of the Mercury's Na, Ca and CaO exospheres simulated by our model and compare our results with the available MESSENGER/MASCS observations. In Chapters 4 we talk about the elements of Earth's exospheric and magnetospheric processes and in Chapter 5 we model ENA sources in the planetary environment. In the final Chapter 6 we introduce the physics of the gas detectors, we describe the instrument model to evaluate the performances, the experimental activities and the results of preliminary tests on the prototype.

CHAPTER 1

Planetary exospheres

This chapter introduces the theory of planetary exospheres, discussing the two cases of the airless planetary environment with particular emphasis on Mercury's exosphere and the exosphere as the upper layer of the atmosphere, focusing on the Earth's environment. It will give an overview of what has been observed and learned about the two planetary bodies.

1.1 Surface-bounded exospheres: Mercury

Many airless bodies of the Solar System possess highly rarefied surface-bound exospheres that mediate transport of species about their surfaces and environment. Planets as Mercury and several large natural satellites such as the Moon, Europa, and Ganymede are surrounded by a tenuous exosphere where the densities are so small that the particles essentially do not collide with each other.
Since these bodies don't have a dense collisional atmosphere, it is not possible to define an exobase. The lower limit of the exosphere is the surface itself, that acts at the same time as source and sink for exospheric molecules. As a consequence, the exospheric composition is strongly linked to the composition and structure of the surface and particles of the surface-bounded exosphere have ballistic orbits that will take them back towards the planetary bodies or may freely escape from planetary gravitational field and be

lost in space.
It is possible to assume the exospheric density n as a function of the radial distance from the center of the planet r is

$$n = \zeta n_0 e^{-\frac{U-U_0}{kT}} \tag{1.1}$$

where

$$U = -\frac{GMm}{r} \tag{1.2}$$

In equation 1.1, n_0 and U_0 are the density and the gravitational potential energy at the surface, k is Boltzmann's constant, T is the absolute temperature; the factor ζ accounts for the fraction of the initial isotropic Maxwellian distribution that is actually present at a given altitude *(Chamberlain, 1963)*. Parameter U in equation 1.2 is the gravitational potential energy at the distance r for a particle of mass energy m for an exosphere in which only gravity acts on the particles; G is the gravitational constant and M is the mass of planetary airless body.
Surface-bounded exosphere is generated by the interaction of the surface with different drivers, such as ions, electrons, meteoroids, photons and thermal radiation. In general, the components of the exosphere can be divided into volatiles, refractories and molecules. Volatiles include elements that do not interact strongly with the surface, such as H and He, which are mainly of solar wind origin, or light gases as Na, K and Ar. These elements have been observed in both Mercury's and the Moon's exospheres. Refractories include species such as Ca, Mg, Al, all of which have very strong bonds with the surface minerals and thus need energetic processes to be ejected into the exosphere. The same energetic processes can release molecules in the exosphere, but they have not yet been detected, for example, in the Hermean environment.
In Mercury's case, planet environment is a complex system: it doesn't have an atmosphere and only a weak intrinsic magnetic field is observed. Its proximity to the Sun creates particularly extreme external conditions. The average speed of the solar wind is approximately 430 km/s and its density and the strength of the Interplanetary Magnetic Field (IMF) decrease with the square of the heliocentric distance, so that on average the density and IMF strength at Mercury are $\sim$10 times greater than those at Earth orbit

(Burlaga 2001; Slavin and Holzer 1981). The interactions between the solar wind and the planetary environment have an impact on the characteristics and dynamics of the exosphere. The study of the generation mechanisms, the compositions and the configuration of the Hermean exosphere provides crucial insight in the planet status and evolution.

Mercury's exosphere has been observed from Earth-based telescopes, which have provided a global view of the planet environment. Given the background noise arising from sunlight reflected by the planet's surface and sunlight scattered by Earth's atmosphere, they could be complemented by in-situ measurements from spacecraft, providing opportunities to investigate the dynamics of Mercury's exosphere.

During the three flybys of Mercury by Mariner 10 between March 1974 and March 1975, the spacecraft's Ultraviolet Spectrometer made robust measurements of H and He and made a tentative detection of O *(Broadfoot et al., 1976)*. These observations were followed a decade later by discoveries with Earth-based telescopes of exospheric Na and K *(Potter and Morgan, 1985, 1986)*. Subsequently, *Bida et al. (2000)* reported the discovery of exospheric Ca from observations with the High Resolution Echelle Spectrometer (HIRES) at the Keck I telescope.

During the three flybys of Mercury by the MESSENGER spacecraft (January and October 2008, September 2009), measurements by the Mercury Atmospheric and Surface Composition Spectrometer (MASCS) instrument *(McClintock and Lankton, 2007)* yielded detections of exospheric Mg *(McClintock et al., 2009)*, Ca *(Vervack et al., 2010)*, Al and Mn *(Vervack et al., 2016)*.

Since its discovery in 1985, Mercury's exospheric Na has been the most studied species both from ground-based observatories and from space.

Earth-based observations have provided a large dataset of images in which recurrent patterns are observed: a high-latitude double peak in both hemispheres of Mercury is the most common Na emission pattern *(Potter et al., 2006; Leblanc et al., 2008; Mangano et al., 2015)*. *Mangano et al. (2015)* categorized the observed emission patterns in a large data set (2009–2013) taken by the Télescope Héliographique pour l'Etude du Magnétisme et des Instabilités Solaires (THEMIS) solar telescope. They confirmed that the most common emission pattern show the presence of high latitude enhancements in both the northern and southern hemispheres 2 peaks (2P) with a prevalence of the first one, typically tens of percent greater than the emission at lower latitudes. The study shows also that peaks often persist for several

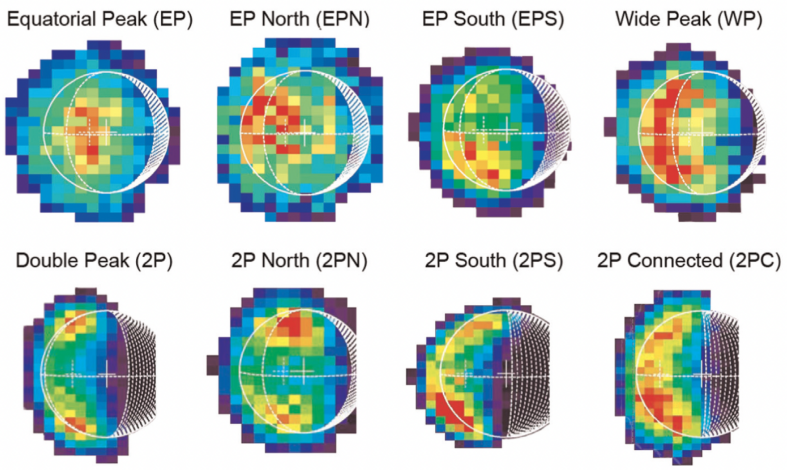

Figure 1.1: Examples of Na emission patterns identified in the Hermean exosphere seen during a set of images collected from 2009 to 2013 with the THEMIS solar telescope (Mangano et al. 2015). Top figures show a single peak located on the equator, shifted or elongated (EP, EPN, EPS, WP), while the bottom ones reproduce the hight latitude double peaks of Na emission (2P, 2PN, 2PS, 2PC)

hours, or even days. The exospheric emission may also peak at low latitudes near the subsolar point, where the Sun's rays strike the planet exactly perpendicular to its surface along the equator (EP), shifted in the northern or in the southern hemisphere (EPN, EPS) or a wider spot elongated in the north-south direction (WP) (Fig. 1.1).

Potter et al. (2006) performed a statistical analysis based on 1997–2003 data and concluded that the distribution of Na emission over the surface was generally non-uniform and variable. They reported that about one third of the observations show north/south asymmetries and the observed random excess emission suggests an external cause not correlated with any characteristic of the planetary orbit or planetary geochemistry. They also analyzed their data in terms of dawn/dusk asymmetry and concluded that the dawn side of the exosphere is usually brighter than the dusk side. This effect seems to be more visible for small TAA up to about 140°, while at larger angles the dawn enhancement is no longer dominant as the planet is close to aphelion up to about 240°, after which it increases but not to values as large as before aphelion (Fig. 1.2). It is suggested that the Na exosphere at Mercury may peak in density at the dawn due to early morning Na ejection and progressive

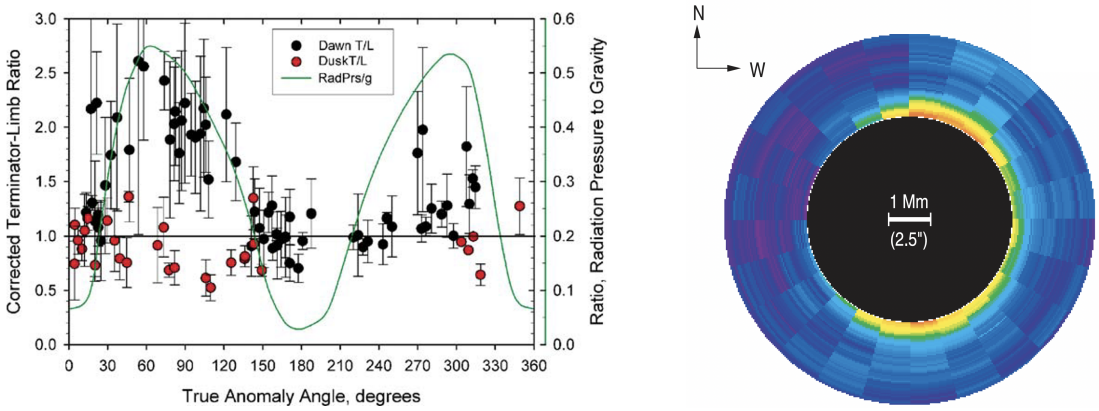

Figure 1.2: Ground based observations of Mercury's Na exosphere: the left panel shows the variation of the terminator-to-limb ratio of Na emission as function of TAA, where the data for the dusk terminator are marked by red circles, while data points for the dawn terminator are filled circles (Potter et al., 2006). Right panel shows an observation during the transit of Mercury across the solar disk in May 2003 with the Vacuum Tower Telescope (VTT) at the Observatorio del Teide, Tenerife. The excess absorption is mainly concentrated near the polar regions and it is evident also a dawn/dusk asymmetry in the Na emission (Schleicher et al., 2004)

depletion of Mercury's dayside surface with increasing local time.
The dawn prevalence with respect to the dusk in the outbound orbit phase has been confirmed by other statistical and case studies *(Sprague, 1992; Schleicher et al., 2004; Cassidi et al., 2016; Milillo et al., 2021)*, see Figure 1.2 and 1.3.

These observations are complementary to those made by MESSENGER from orbit around the planet that characterized the seasonal and annual behavior of the Na exosphere *(Cassidy et al., 2015; 2016)*. The specific observational configuration of the analysed data from the southern apoherm of MESSENGER allows the equatorial mapping of the exosphere. The observations show a repeatable seasonally varying equatorial Na exosphere. *Cassidy et al. (2016)* showed that the Na enhancement rotates with the surface and peaks near the sunlit cold pole longitudes of Mercury, i.e. the equatorial region where the average temperature is colder (left panel of Fig. 1.3).
These results have been confirmed by the analysis of the THEMIS ground-based observations by *Milillo et al.; (2021)*, which provided a view of the equatorial asymmetries of the Na column density along Mercury's orbit (right

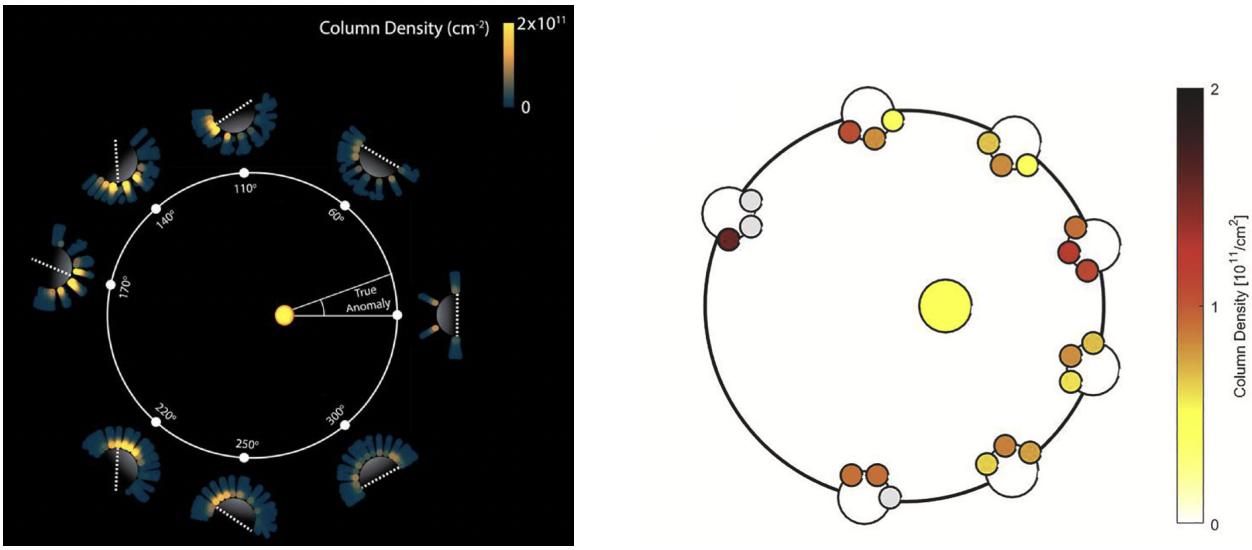

Figure 1.3: Observed Na column density projected onto Mercury's equatorial plane over the course of a Mercury year: the left panel shows the variation of Na enhancements in the cold pole longitudes (white dashed lines) (Cassidy et al., 2016); the right panel shows the asymmetries of the Na exosphere obtained from the THEMIS dataset (Milillo et al., 2021)

panel of Fig. 1.3). The supported scenario is that there is a migration of Na towards the night side with a preferential condensation on the coldest surface and that these atoms are redistributed when the surface is again exposed to sunlight. Furthermore, the explanation of this seasonal peak variation also seems to be consistent with the preferential impact of meteoroids on Mercury's surface at the same longitudes (*Mura et al.; 2023*). Hence, the Na enhancement at these longitudines could be due to an additional external source.

Another important feature observed in the Na exosphere is a tail in the anti-sunward direction. It varies from a few up to more than 1000 Mercury radii along the planet's orbit according to the radiation pressure (see section 2.10) *(Potter and Killen, 2008; Schmidt et al., 2010)*. During MESSENGER's Mercury flybys, UVVS, sensor of the MASCS instrument *(McClintock and Lankton, 2007)* on board the MESSENGER spacecraft *(Solomon et al., 2007)*, observed the Na exosphere by obtaining profiles of the tail *(McClintock et al., 2008; 2009; Vervack et al., 2010)* extending over the nightside of the planet. Images constructed from three flybys M1, M2 and M3 observa-

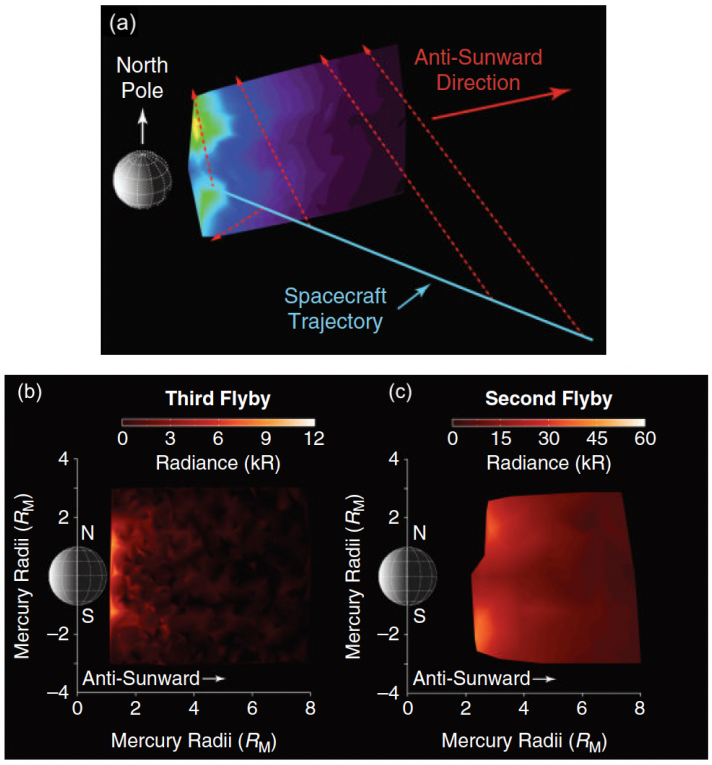

Figure 1.4: Comparison of the Na tail observations from the three MESSENGER flybys of Mercury: panel (a) reconstructs the image of the UVVS observation geometry during the first flyby M1; panels (b) and (c) show the observed column Na emissions from M2 and M3 projected onto the plane containing the Sun-Mercury line, where the x-axis points in the anti-sunward direction, z is perpendicular to the orbital plane of the planet (McClintock et al., 2008; Burger et al., 2012)

tions of the Na tail are shown in Figure 1.4: it is observed that exosphere is pushed and transported in anti-sunward direction with a brightening of the exosphere above the poles in all three observations.

Other ground-based campaigns of exospheric Na observation are planned. In particular, recently an observation campaign has been performed, focusing on contemporary observation during the new mission BepiColombo flybys at Mercury (2023 campaign described in the Appendix A).
Whereas the Na component of Mercury's exosphere has been regularly observed, the Ca detections are much more limited in time because the emission is fainter and at a wavelengths that are more difficult to observe from the

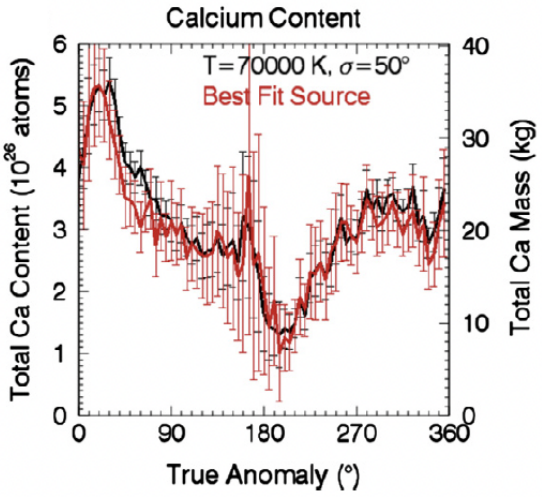

Figure 1.5: Exospheric Ca content in terms of total number of atoms and total Ca mass as a function of Mercury TAA comparing the best-fit to UVVS observations (red line) and the source rate determined by Burger's model using a source with a fixed temperature T = 70,000 K and width σ = 50° (black line) (Burger et al., 2014)

Earth than the Na. In-situ measurements with UVVS provided the first high spatial resolution observations of exospheric Ca during spacecraft flybys of Mercury that exhibited very high energies, with a scale height consistent with a temperature up to 50,000 K. *Burger et al (2012; 2014)* simulated these data with a model of exospheric source processes to reproduce this persistent and extremely hot Ca exosphere. They concluded that the Ca source is located exclusively on the dawn-side of the planet with a seasonally, not sporadically, variable content.

Furthermore, *Burger et al. (2014)* fitting the UVVS observations over two years (March 2011-2013) obtained the variations of the total Ca exospheric component with heliocentric distance in term of total Ca atoms as function of True Anomaly Angle (TAA), i.e. planet position on its elliptical orbit with the angle between its radius vector and the perihelion position (Fig. 1.5). The plot reproduces a peak at perihelium and a minimum value at aphelion with an excess emission in the plot shortly after Mercury passes through its perihelion at TAA $\sim 25°$.

The flyby observations revealed several key features of the Ca exosphere,

which indicated substantial differences from the sodium exosphere. While both exospheres present a pronounced dawn-dusk asymmetries with the dawn being more intense, Na shows the brightest emission at northern and southern latitudes and Ca is brightest in the equatorial region. These different distributions may be caused by a combination of different source and/or loss processes.

1.2 Atmosphere-bounded exospheres: the Earth

In the case of planetary bodies with dense atmospheres, the air pressure at any height in the atmosphere is due to the force per unit area exerted by the weight of all of the air lying above that height. Consequently, atmospheric pressure decreases with increasing height above the ground. If the upward-directed pressure gradient force is equal to the downward-directed force due to gravitational attraction that acts on a thin layer of air, the gas is in hydrostatic equilibrium. The static condition is expressed by the Navier-Stokes equation as the balance between the vertical pressure gradient and gravity

$$\Delta p = -g\rho \tag{1.3}$$

with the density ρ and the standard gravity g. In the isothermal approximation it is possible to assume a pressure profile like

$$p(z) = p(0)e^{-\frac{Z}{H}} \tag{1.4}$$

where p(0) is the surface pressure and the atmospheric pressure p falls off exponentially with vertical height z at a rate given by the scale height H, that depends on the mean molecular mass. In this equilibrium conditions, the exosphere, as the uppermost layer of planetary atmosphere, gradually fades into outer space and there is no clear upper boundary (Fig. 1.6).
In the case of the Earth, the altitude of the exobase, i.e. lower boundary of the exosphere, varies from about 500 to 1000 km. The atomic neutral hydrogen H is the most abundant element in the planet exosphere above $\sim$ 1500 km and it is constituted of a gravitationally bound halo called the H geocorona *(Shklovsky,1959)*. The expanded presence of exospheric H in the high atmosphere of the Earth can be observed trough ultraviolet (UV) observations, via the H Lyman-alpha emission line at 121.6 nm produced by scattering of solar Lyman-α radiation by H atoms.

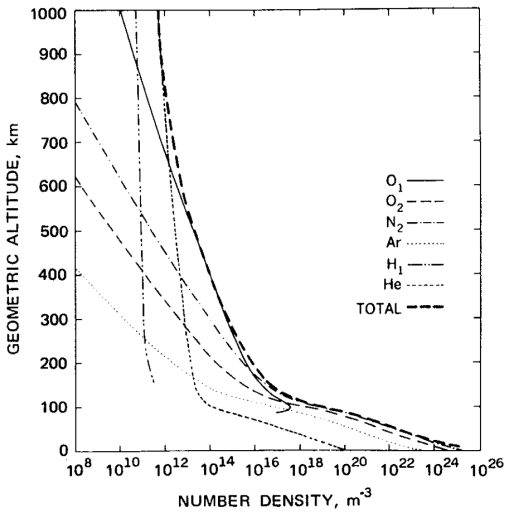

Figure 1.6: Number density of species in the upper atmosphere as a function of altitude (Emmert et al., 2020)

Several spacecraft missions provide extensive geocoronal observations to describe the extension and properties of Earth's environment.
The first observations of the terrestrial exosphere were carried out by the Mariner 5 missions at a distance of 37 R_E (1 R_E= 6.371 km) *(Wallace et al., 1970)* and by Apollo 16 at a distance of 60 R_E *(Carruthers and Page, 1972)*, where images of the geocorona were captured by astronauts from the lunar surface revealing an exospheric extension of 15 planetary radii (Fig. 1.7).
Observations carried out by the GEO instrument on board the IMAGE satellite *(Fuselier et al., 2000)* found that the H density distribution shows a cylindrical symmetry around the Sun-Earth line with an enhancement in the anti-solar direction towards the geotail, characterised by higher H densities on the night side of the Earth. The SWAN-SOHO mission *(Baliukin et al., 2019)* and the Lyman Alpha Imaging Camera on board the Japanese spacecraft PROCYON *(Kameda et al., 2017)*, further confirmed the presence of this extended component, revealing an exospheric extension of more than 38 R_E in the antisolar direction.
Reconstruction of the global H distribution, obtained from Lyman-α Detector (LAD) data on board the TWINS (Two Wide-angle Imaging Neutral-atom Spectrometers) mission (June 2008) *(Bailey and Gruntman, 2011)* revealed a number of asymmetries: a day-night asymmetry, showing an enhancement

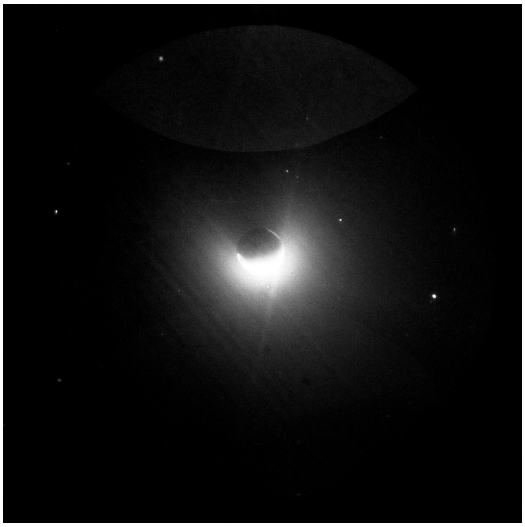

Figure 1.7: Earth's geocorona as viewed from the surface of Moon, acquired during the Apollo 16 mission (April 1972) (Carruthers et al., 1976)

of geocorona in the anti-solar direction; a seasonal north-south asymmetry, which occurs as solar illumination differs between the summer and winter polar regions; a dawn-dusk asymmetry, which is less prominent than the others. A complete knowledge of the global exospheric density distributions enables a better understanding of the Earth's atmospheric evolution through gravitational escape as well as numerous solar-terrestrial interactions (*Gronoff et al., 2020; Dandouras, 2021*) .

CHAPTER 2

Elements of Mercury exospheric processes

The exosphere generation is the result of the complex relationship between planetary bodies and external environment, a synergy of more than a single process to account by observational evidence.
For a planet with a collision-dominated atmosphere, a population of particles that enters from below the exobase supplies the exosphere. In contrast, a surface-bounded exosphere is supplied both by incoming sources, including the solar wind (H and He), micrometeoroids and by particles released from the surface through a variety of processes that include sputtering by solar wind ions, desorption by solar photons and electrons, impacts by micrometeoroids, and thermal desorption of surface materials *(Milillo et al., 2005)*.
Source processes are balanced by loss processes, which include photoionization and photodissociation of molecules, ionization followed by transport along magnetic field lines, acceleration by solar radiation pressure, Jeans escape and also sticking to the planet surface. These mechanisms have different efficiencies depending on the species and how they are bonded with other molecules on the surface and/or in planet environment. The main source and loss processes from a planetary body will be discussed in this chapter.

2.1 Thermal Desorption

Thermal desorption (TD) is due to the atoms thermal energy exceeding the binding energy at the surface and it is responsible for the release of volatile species present on the upper surface layers of regolith grains into the exosphere.
The amount of released material depends strongly on the Sun's photon flux, which is $3 \cdot 10^{15} cm^2/s$ at 1 AU, in the infrared range and on the surface temperature (in the range of 100-700 K at Mercury). For Mercury, given the high temperatures at and near the sub-solar point, volatile species like Na or K can be released in the planet exosphere by TD process. Applied to planet's regolith, this implies that the Na atoms will be very quickly thermally desorbed leading to a significant surface's depletion in the afternoon of Mercury *(Hunten and Sprague, 2002)*. The TD process produces 0.03 - 0.05 eV Na atoms *(Yakshinskiy et al, 2000)*, whereas the escape energy for Na from Mercury's surface is 2.07 eV; hence, the desorbed atoms remain close to the surface and do not contribute significantly to planetary loss, because the velocity of released atoms is generally lower than escape one. So, TD is expected to be the most efficient desorption process at low zenith angles, producing a very dense exosphere in the dayside, but in the same time, this process is not effective in global loss from the planet, since the fraction of particles that escape is well below 1 % on average *(Killen et al., 2004)*.

2.2 Photon-Stimulated Desorption

The PSD process results from the desorption of neutral atoms or ions induced by photon bombardment of the planet surface. Principally the process depletes the most volatile species, as Na and K, because the photon energies mainly in UV range are not high enough to release the most tightly bounded atoms.
Laboratory experiments by *Madey et al. (1998)* and *Yakshinskiy and Madey (1999)* have been fundamental to the understanding of the PSD release process for Mercury and the Moon. The authors studied Na atoms that can be released via PSD from surfaces that simulate lunar silicates. They clearly demonstrated that PSD is a non-thermal process, the atoms desorption is the result of an electronic excitation resulting from the absorption of a UV photon at the surface. Although of lesser importance for the exospheres of

Mercury and the Moon, laboratory work on the PSD of water molecules from lunar surface material has also been observed *(De Simone and Orlando 2014, 2015)* H_2O as released element via PSD.
The PSD depends strongly on the Sun's irradiance, in fact the intensity of the flux of ejected particles varies with the UV photon flux. The latter is scaled to the square of the heliocentric distance, hence is variable along Mercury's eccentric orbit. The release efficiency depends on the surface composition and mineralogy, and on the surface density concentration by atomic fraction. PSD is likely to be the dominant source process of exospheric Na at Mercury *(Wurz and Lammer, 2003)*. The largest PSD fluxes of Na occur near equatorial latitudes on the dayside when the flux of solar photons is high, while there is no photon flux on the nightside. The maximum released Na flux is expected to occur at the sub-solar point.
Since the TD process is also a function of the photon flux, there is a direct competition between these two processes. The TD release for Na is more efficient at temperatures of sub-solar point. It is therefore expected to dominate over the PSD there, but the PSD in a more energetic process and it is expected to be able to reach higher altitudes.

2.3 Electron Stimulated Desorption

The airless body's surface environment is continuously bombarded by solar radiation and electrons, that are absorbed by the surface and causes heating and alteration of the dayside surface area. Electrons in the order of tens of eV can cause electronic excitations that also lead to Electron Stimulated Desorption (ESD) where the absorption of an energetic electron leads eventual release of an atom or molecule from the planetary surface *(McLain et al., 2011)*.
In addition to PSD experiments with adsorbed Na and K atoms on lunar silicates, *Yakshinskiy and Madey (1999)* also studied ESD as one possible source process contributing to the planet exosphere. ESD and PSD are considered to be similar non-thermal mechanism because electronic processes cause desorption of the atoms via electron or photon excitation. Electron fluxes for electrons with energies of about 12 eV are about $10^9 cm^{-2} s^{-1}$, these are several orders of magnitude smaller than the photon flux. For this reason, ESD is not the main release process for adsorbed surface elements like Na or K compared to PSD at least in the dayside. It could be much more relevant

in the nightside.

2.4 Ion Sputtering

The impact of energetic ions on a airless bodies surface causes the release of atoms or molecules via sputtering. This process is called Ion Sputtering (IS) and it is the result of the nuclear interaction of a projectile ion with the target material, which is the case for the rocks and regolith on Mercury's and the Moon's surface *(Wurz et al., 2022)*. Refractories elements are generally responsive only to the most energetic processes like IS and meteoroids impact (section 2.8) *(Milillo et al., 2020)*. The products arising from this particle bombardment depend on the composition and chemical structure of the planet surface. The process reproduces more or less the local surface composition on an atomic level and could play a role in the refilling of the exosphere.
Ion sputtering has been suggested as the source of rapid variations in Mercury's Na exosphere *(Potter and Morgan, 1990; Killen et al., 2001)*. In the Hermean environment, the ions precipitating onto the surface could be of solar wind or planetary origin. In fact, ions circulating inside the magnetosphere could eventually precipitate onto the surface. However, the sputtering directly induced by these two populations are expected to be effective in different regions *(Ip, 1993)*, namely at high latitudes in the dayside sector in the former case and mid-latitudes in the latter case.
Observations of the Na exosphere exhibit very often two high-latitude peaks usually located in both hemispheres, along the subsolar meridian; they could differ in intensity and/or extent. The morphology of the two-peaks of Na intensity seem related to the interaction of the solar wind particles with the intrinsic magnetic field of the planet that drives them into preferred regions of the surface, as the foot prints of the magnetic cusps *(Mura et al 2005; Potter et al. 2006)*. The intensity of the ion flux depends on the magnetospheric configuration, which, in turn, depends on both the intrinsic magnetic field of Mercury and variable external parameters, such as the IMF, solar wind velocity and density *(Raines et al., 2014; 2022)*.
Statistical studies *(Lammer and Bauer ,1997; Potter et al., 2002a)* and Earth-based observations *(Mangano et al., 2015)* (Fig. 1.1) have shown that the double peak patterns often persist for several hours, or even days, supporting the idea that quasi-steady SW ion precipitation through the polar

cusps plays a key role in Na exosphere generation. Futhermore, *Massetti et al., 2017* suggest that intensity variations on a timescale of 10 min of Na exospheric emission from both the northern and southern hemispheres seem to be compatible with the response time of the Na exospheric release, as induced by impulsive events consistent with ion precipitation.

2.5 Ion Back Scattering

When the precipitating solar wind particles impact the planet's regolith, ions can be neutralized and come into close collision with target molecules on the surface. As a result, a fraction of the ions can be backscattered from the surface as neutral atoms. This process is called Ion BackScattering (IBS).
The products arising from this particle bombardment depend on the surface composition and from the ion's impact energy. It is reasonable to expect that lighter ions are backscattered more effectively than heavy ions, considering the conservation of momentum assuming elastic collisions with free target atoms or molecules *(Plainaki et al., 2010)*.
The observations by the CENA (Chandrayaan-1 Energetic Neutral Analyzer) sensor onboard Chandrayaan-1 (*Bhardwaj et al. 2005, 2010; Barabash et al. 2009*) and the IBEX mission *(McComas et al. 2009)* have provided new insights into the ENA environment around the Moon as consequence of back scattering processes. Since the Moon is not shielded by a global magnetic field or by an atmosphere, solar wind plasma impinges onto the lunar surface almost unhindered. A fraction of the impinging solar wind ions is backscattered as energetic neutral atoms. Since these backscattered neutral particles are not affected by any electric or magnetic fields, each particle's point of origin on the lunar surface can be determined in a straight-forward manner allowing to create energetic neutral atom maps of the lunar surface. Figure 2.1 shows the map of lunar hydrogen ENAs from observations by CENA: local variations in this map express the fact that the lunar surface is not a homogeneous sphere. The darkest regions in the map could be explained by the presence of magnetic anomalies and/or the formation of mini-magnetospheres on the lunar surface *(Wieser et al., 2010; Vorburger et al. 2012)*, which could shield the impinging solar wind ions.

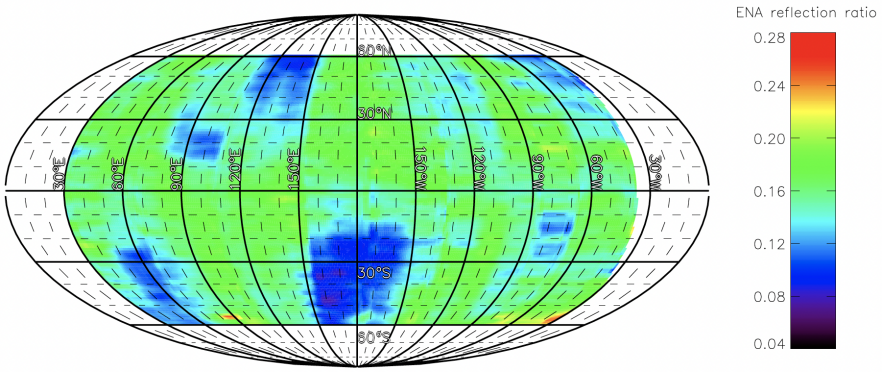

Figure 2.1: Global ENA albedo map of the lunar surface observed by CENA sensor onboard Chandrayaan-1. Map reproduces the ENA reflection ratio as the percentage of solar wind ions that are backscattered from the lunar surface as neutrals (Vorburger et al. 2013)

2.6 Chemical sputtering

We discussed in previous sections that the impact of energetic ions (solar wind or magnetospheric ions) on the surface affects the topmost layer of the regolith inducing sputtering of surface material with the direct release of atoms from the surface. It is important to consider that ion impacts can also cause chemical alteration of the surface.
The precipitating ions could be responsible for chemical sputtering, which breaks existing chemical compounds on the surface and creates new ones, and can also increase the diffusion rate by creating defects in the structure of the surface grains, a process known as ion, or radiation, enhanced diffusion *(Killen et al., 2004)*.
For example, production of Na and water by proton sputtering of Na-bearing silicates onto Mercury surface is considered products of the chemical sputtering *(Potter, 1995)*. Part of the solar wind protons are implanted into the regolith and are neutralized there: H reacts with the Na-bearing rock and Na atoms are liberated from their chemical bounds in the crystal through the chemical reaction

$$2H + Na_2SiO_3 \rightarrow 2Na + SiO_2 + H_2O$$

Since the ion penetration is close to the surface, the atomic Na is produced near the surface and can be easily released into the exosphere either

by TD or by PSD processes *(Yakshinskiy and Madey, 2000; 2004)*.
Furthermore, the chemical sputtering of Na causes also the production of water and groups of molecules (OH, H_2), which are a compound in the Mercury exosphere that was discovered by FIPS instrument on board MESSENGER *(Zurbuchen et al., 2008)*.

2.7 Enhanced diffusion

A possible source of exospheric element may depend on ion enhanced diffusion. The impact of ions onto the surface causes an increase in temperature, resulting in a rapid diffusion of particles to the top of the regolith and greater escape to the exosphere *(Sizmann, 1978; Starostin,2006)*. On Mercury, it has been observed that the local PSD rate is higher in the areas of intense proton precipitation and this effect could be due to the enhanced diffusion process *(Killen et al., 2004; Mura et al., 2009)*.
This conclusion is supported by the observed abundances of the lunar atmosphere as it moves within the Earth's magnetosphere. *Sarantos et al. (2008; 2010)* have shown for the lunar exosphere that the ion enhanced diffusion during certain phases of the planetary orbit enhances the efficiency of other exospheric source processes for volatile elements. In particular, the increase in relative efficiency of the PSD due to the bombardment of the lunar surface by the plasma sheet ions during the passage through the Earth's magnetotail is shown to be about two times higher than that due to solar wind ions.
The correlation between an enhancement of the exosphere and an increase in plasma precipitation on the regolith surface could also be consistent with Mercury observations.
Regardless whether the physical process could be chemical sputtering or enhanced diffusion, the effect is that plasma precipitation gives "fresh" particles to the surface that can later be desorbed by PSD or TD.

2.8 Micro-Meteoroids Impact Vaporization

Planetary bodies are subject to a constant meteoroids bombardment on their surfaces and atmospheres as they move along their orbits.
We talk about impact vaporization process for the case of airless bodies, as Mercury, where meteoroids impact the surface, producing impact debris and generating surface release into the exosphere. Exospheric formation through

MMIV process depends both on the impact velocity and on the directionality of incoming flux with respect to the planet's motion and also on the mass and size of impactors.
The bombardment of Mercury's surface by micro-meteoroids derives from different sources, as Main Belt Asteroids (MBA); Jupiter Family Comets (JFCs), generally comets with orbital periods below 20 yr and inclinations below 30°; Halley Type Comets (HTCs) with orbital periods beetwen 20 and 200 yr; and Oort Cloud Comets (OCCs) with orbital periods larger than 200 yr *(Pokorny et al. 2018)*.
MBA meteoroids dominate the flux at Earth orbit, in comparison to particles from cometary sources *(Ceplecha 1992)* while, approximately, only 17 % of mass influx at Earth originating from MBAs is recorded at Mercury. Instead, meteoroids originating from short period comets, as JFCs, dominate the inner Solar System *(Nesvorný et al.2010, 2011a)*. This family of meteoroids intersects Mercury's orbit with low eccentricities orbit, slightly higher compared to those of MBA meteoroids ($0.2 > e_{JFC} > e_{MBA}$). JFC meteoroids have a wider distribution of eccentricities, which weakens the gravitational focusing and leads to higher mass accretion on Mercury as compared to that at Earth *(Pokorny et al. 2017; 2018)*. As a consequence of the low eccentricity orbits of MBA and JFC, the meteoroids have low relative impact velocities, $V_{imp} < 70\ kms^{-1}$ at Mercury perihelion (panels (a) and (b) of Fig. 2.2) and $V_{imp} < 50\ kms^{-1}$ at aphelion.

The source populations namely HTCs and OCCs have impact velocities at Mercury as high as $95kms^{-1} < V_{imp} < 120kms^{-1}$ at perihelion (panels (c) and (d) of Fig. 2.2) and $75kms^{-1} < V_{imp} < 90kms^{-1}$ and are less influenced by planet's orbital motion. The long-period comets are not considered to be a dominant part of the inner solar system meteoroid budget in terms of mass flux, but at the same time the high impact velocity of these particles makes them relevant for the morphology of the Mercury exosphere resulting an important exospheric source in terms of the impact vaporization *(Pokorny et al. 2017; 2018; Janches et al. 2021)*.
In conclusion, Mercury is exposed to the constant precipitation of small size particles ($< 100\ \mu$m) that impact into the regolith of planet at a mean velocity of 30 km/s *(Cintala, 1992)* with also a less frequent component of fast particles with velocity in the range 80 -110 km/s (Fig.2.3) *(Pokorny et al. 2018)*. So, the exosphere is continuously replenished under the action of these micro-meteoroid impacts.
Larger impactors with size $>$ 2 cm arrive with a much broader impact veloc-

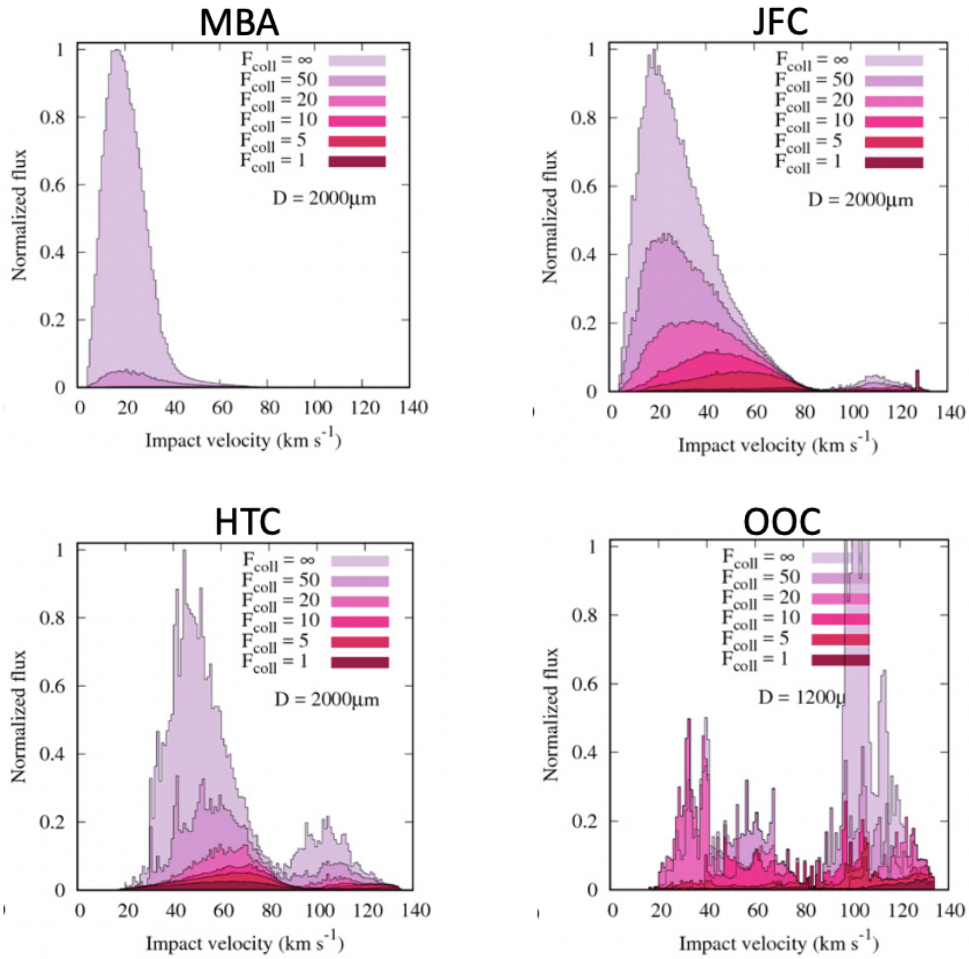

Figure 2.2: Distribution of impact velocities for MBA, JHC, HTC and OCC meteoroids with dimension D for TAA= 0°. Different collisional lifetime multipliers factor F_{coll} are represented by the range of colors (Pokorny et al. 2018)

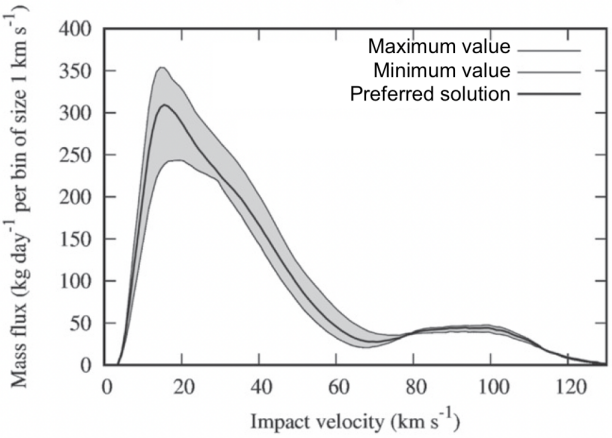

Figure 2.3: Distribution of averaged mass flux as function of impactors velocities is provided as total accumulated mass over one Hermean year divided by number of days. Gray area and thin black lines representing interval boundaries, while the thick black lines shows the preferred solution for Pokorny et al 2018' model

ity distribution at Mercury, ranging from 4 to around 40 km/s *(Marchi et al. 2005)*, causing local enhancement of exospheric density. Nevertheless, the larger particles are likely of little significance for the study of the permanent exosphere content because they can produce significant local enhancements but are infrequent *(Mangano et al., 2007)*.
Signature of major meteoroid impact have been observed by MESSENGER. A transient enhancement of Mercury's exosphere was observed by FIPS (Fast-Imaging Plasma Spectrometer) instrument onboard the MESSENGER spacecraft, which detected heavy ions of planetary origin from a plume probably caused by a meteoroid impact event (*Jasinski et al., 2020*). Furthermore, UVVS observations also show other cases of exospheric enhancements at Mercury's nightside due to a meteoroid Impact (*Cassidy et al., 2021*).

2.8.1 Special focus on Ca generation process

Differently from exospheric volatiles species like Na, refractories species like Ca and Mg are expected to be released from the surface by more energetic processes such as MMIV and/or ion sputtering *(Killen et al, 2010; Wurz and Lammer, 2003)*. In-situ observations of Ca Mercury exosphere with MESSENGER/UVVS instrument showed very high energies, a scale height

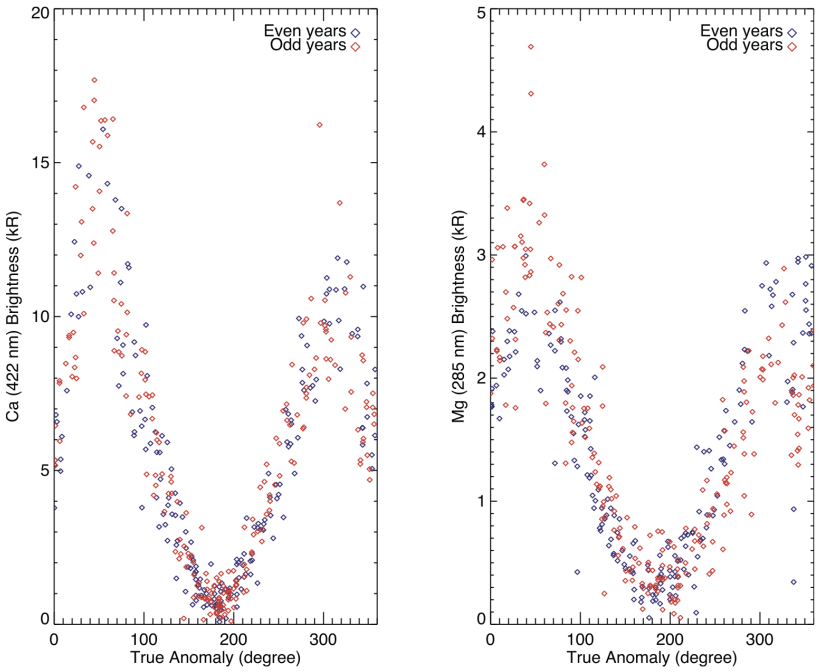

Figure 2.4: Seasonal variations of the Ca (left panel) and Mg (right panel) emissions from different Mercury years derived from MESSENGER observations (Chaufray et al. 2022)

consistent with a temperature up to 50,000 K and a dawn enhancement with a pronounced dawn–dusk asymmetry *(Burger et al., 2012; 2014; Merkel et al., 2017)*, that is consistent to the directionality of micrometeoroids impact. This Ca component seems quite well reproduced year by year. While the Mg component seems slightly variable for odd or even orbits. This is explained with the exposure of a Mg reach region to the micrometeoroid impacting flux *(Merkel et al., 2018; Chaufray et al., 2022)* (Fig. 2.4).

In addition to the seasonal exosphere, transient events have been observed on Mercury's nightside by monitoring the exospheric atomic emissions of Na, Mg and Ca. The observations show sudden enhancements of Na and Mg, but no evidence of enhancement for the Ca component (*Cassidy ei al., 2021*), consistent with the idea that Ca is bound in molecules in the impact vapor and the molecules are undetectable to UVVS *(Killen et al. 2005; Berezhnoy 2018)*.

The observations provide an interesting case on which we focus our study

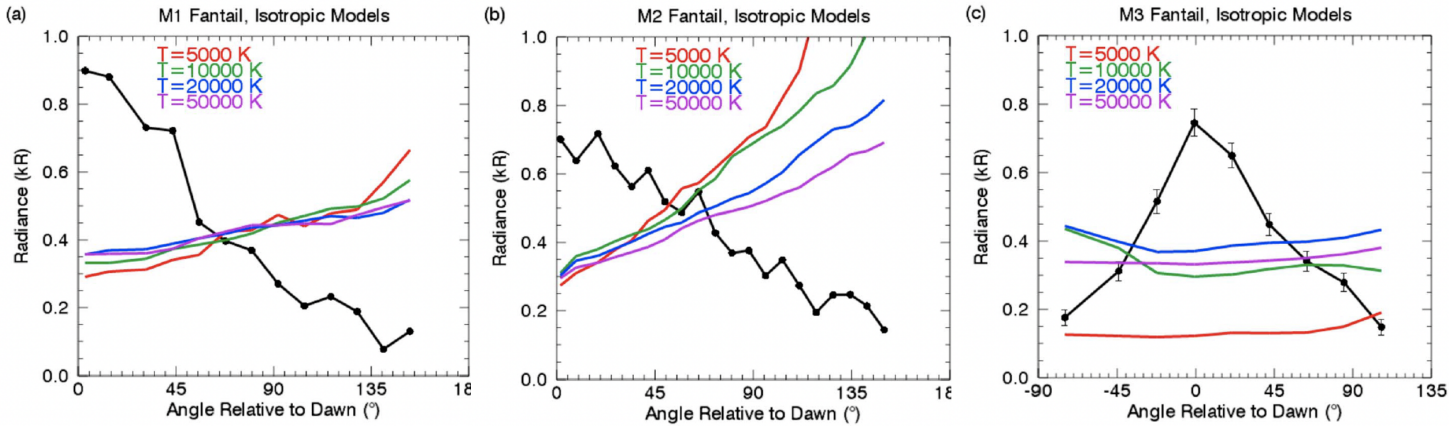

Figure 2.5: Comparison of UVVS fantail data from the three flybys M1, M2 and M3 (black line) (panel (a), (b) and (c) respectively) with model simulations having sources isotropically distributed over Mercury's surface for temperatures ranging between 5000 and 50.000 K (Burger et al., 2012)

to investigate the possible pathways that produce the observed high-energy Ca exosphere and the generating mechanism of this element in Mercury exosphere. The exospheric Ca model by *Burger et al., 2012* reproduces this persistent and extremely hot Ca exosphere. They first considered the exosphere that results from an isotropic source of Ca, i.e. one that is uniform over Mercury's surface, comparing the UVVS tail data from all three flybys with model simulations (Fig. 2.5). It is evident that an isotropic source is not consistent with the data, it does not reproduce the tail measurements for any of the flybys. The authors suggested that there is a substantial dawn enhancement in the Ca source. To simulate this enhancement, they modeled the data under the assumption that all the Ca is emitted from a region on the surface centered at the dawn, equatorial point, reproducing dawn–dusk asymmetry (Fig. 2.6).

The total Ca content, obtained through a best fit to the UVVS observations in the Figure 1.5, varies by a factor 5 due to the changing Ca photoionization lifetime, between 1380 s at perihelion and 3120 s at aphelion, showing a peak at TAA= 0° and a minimum value at TAA = 180°.
The excess emission near TAA $\sim 25°$ was attributed to the vaporization of surface material induced by the impact of a meteor stream, possibly resulting from Comet Encke *(Killen and Hahn, 2015; Plainaki et al., 2017)*. The origin of this high-energy, asymmetrically distributed population still needs

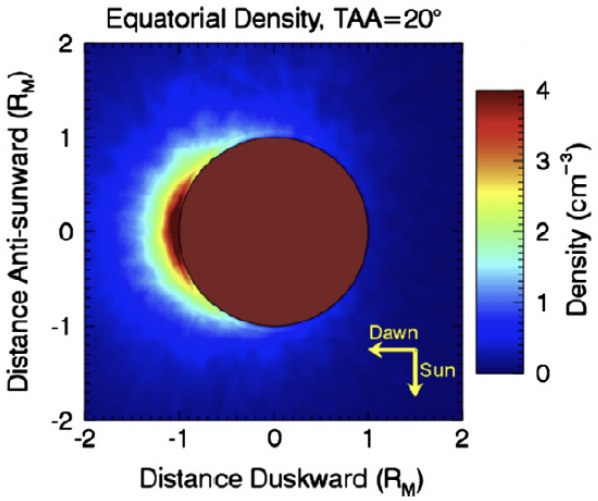

Figure 2.6: Simulation results of Ca exospheric component by Burger's model: Ca density in Mercury's equatorial plane at TAA = 20°, based on best-fit model for a source with temperature T = 70,000 K and width σ = 50° (Burger et al., 2014)

to be fully explained. *Killen (2016)* examined different possible pathways responsible for ejecting Ca from Mercury's surface to the exosphere. To explain the observed Ca energization, ion sputtering is not considered as the primary source process for Ca: in fact, thought it could explain the high energy of observed Ca, it could not reproduce the measured spatial and temporal variation that is linked to the ion precipitation onto the surface.
The collisions between meteoroids and planetary surface are followed by volatilization and expansion of the impact-produced cloud of refractory metals and, for the Ca bearing minerals at Mercury surface, the most likely involved compounds are $Ca(OH)_2$, CaOH, and/or CaO. The Ca atoms are produced via subsequent photolysis of these molecules considering the additional energy imparted to Ca products equal 0.9 eV, 0.3 eV, and 0.6 eV, respectively *(Berezhnoy, 2018)*. The final products after the impact depend on the quenching temperature of the expanding cloud that is expected to be in the range 3000 - 4000 K. Exact temperature, photolysis lifetimes of the produced molecules and excess energy during different photolysis processes are still not well constrained by observations.
At temperatures $\leq$ 3750 K in the impact-produced cloud $Ca(OH)_2$ dominates over both atomic Ca, CaO and CaOH, while at higher temperatures

it is considered that the predominant form of the initial calcium ejecta is CaO *(Berezhnoy, 2018)*. A two-step process is suggested in which the initial Ca-bearing molecules ejection by MMIV is followed by a second process that dissociates these molecules, and produces highly energetic atomic Ca as observed during MASCS measurements.
The CaO molecules can be dissociated in the exosphere by different processes. It was shown that electron-impact dissociation cannot reproduce the observed Ca tangent column density of 5 -15 $\cdot 10^8 cm^{-2}$ as in *Burger et al. (2014)*. In fact, the solar wind electron flux is estimated between $10^8 - 10^9 cm^{-2}s^{-1}$ *(Gershman et al., 2015)*, the e-impact dissociation cross section is of the order of $0.4 \cdot 10^{-16} cm^2$ at 1 keV *(Miles et al., 2015)* and the lifetime of neutral Ca as the photoionization lifetime at Mercury is between 1380 s at perihelion and 3120 s at aphelion. As a result, the column density of Ca would be $< 10^5 cm^{-2}$ *(Killen, 2016)*, which is orders of magnitude too low compared with the observed Ca one. The spontaneous dissociation of CaO could also be a possible pathway for producing Ca, but the energy in the products is less than 1 eV/atom and is not enough to accelerate the atomic Ca to the altitudes where it is observed. The photodissociation of the released CaO molecules by MMIV could explain the dawn-dusk asymmetry of the exosphere, because the molecules are preferentially ejected into the exosphere in the dawn side by impact vaporization and subsequently dissociated by photons. But the resulting Ca cannot acquire the observed high energies T $\sim$ 50000 K, so it contributes for the low energy Ca component in the planetary exosphere. Hence, these processes are not good candidates to cause the release of energetic Ca into the Mercury exosphere.
Killen 2016 suggested that the most likely origin of extremely energetic Ca seen in Mercury's exosphere is CaO non-equilibrium dissociative ionization produced by impact vaporization, followed by neutralization of Ca^+.
Plainaki et al. (2017), starting from the same assumptions in *Killen (2016)* and from the maps of stream impactors onto the surface in *Christou et al. (2015)*, where only $< 1\%$ of the vapor is ionized and dissociates, modeled the 3D distribution of the Ca exosphere after the crossing of the comet 2P/Encke dust stream. The simulated Ca distribution was consistent with the geometry and the vertical profile of the MESSENGER/ UVVS observations, but not with the intensity. In fact, the estimated Ca column abundance produced by shock-induced dissociative neutralization was $< 4 \cdot 10^7 cm^{-2}$, lower than the observed one by up to 2 orders of magnitude. This disagreement is reasonably related to the uncertainty in the definition of some parameters

and assumptions used in their model, as also suggested by the same authors *(Plainaki et al., 2017)*. The strong dependence of some of the modeled quantities on specific input-parameters, which in turn describe the actual nature of the phenomenon in action, shows the complexity in the interpretation of the Ca-observations.
In addition to this, *Berezhnoy (2018)* analyzed the chemistry of formation of molecules and dust grains in the cloud produced after collisions by meteoroids: it was found that the molar fraction ratio between the atomic and molecular Ca-bearing component is 1:3 at quenching temperature of 3000 – 3500 K if the initial temperature and pressure of the impact-produced cloud are 10000 K and 10000 bar, respectively.
In the section 3.6 we will further investigate the Ca exosphere generation by applying our exospheric model.

2.9 Photoionization and photodissociation

Photoionization is a physical process where an ion forms via the reaction between a photon and an atom or a molecule. This can occur when the energy of a photon is greater than the ionization energy of the atom or molecule. The resulting ion can be in various states of excitation and may emit radiation as it relaxes to its ground state. The photoionization rate is proportional to the number density of neutral gases, solar irradiation and the photoionization cross-section of the chemical species, that is a function of the energy of the photon.
Photodissociation is a physical process in which a chemical compound is broken down due to the action of photons. To have enough energy to break up a molecule, the photon is likely to be an electromagnetic wave with the energy of visible light or higher, such as ultraviolet light and X-rays and gamma rays. The resulting products from photodissociation process could be charged or neutral.
The difference between these processes is that photoionization is a major loss process of the atmosphere and exosphere in sunlight, whereas photodissociation could be considered a loss process when the products of reaction are charged, but in the case of neutral products photoionization contributes to replenish the planet exosphere.

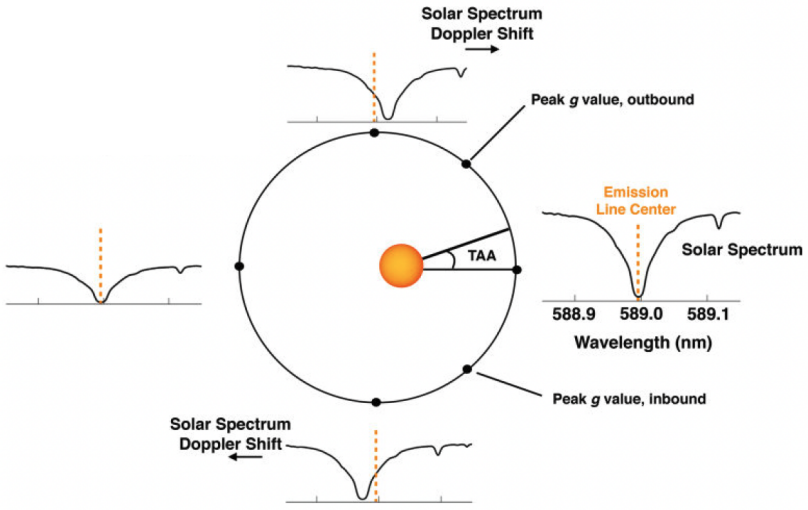

Figure 2.7: Doppler shift effect on the solar spectrum around the D2 line of Na (rest wavelength of 588.995 nm) as a function of TAA. The spectrum shows a deep absorption of the solar Fraunhofer D-line near the rest wavelength of the transition (dashed yellow line). As Mercury orbits around the Sun, the radial component of planet velocity begins to increase, causing the solar spectrum to shift towards longer and shorter wavelengths and reaching a maximum shift at TAA = 90°and at TAA = 270° (Solomon et al., 2018)

2.10 Radiation pressure effect

The loss of neutral particles in an exosphere can also be measured by observing the tail generated by the acceleration of specific species, particularly alkalis, in the anti-solar direction due to the radiation pressure effect. When an atom is released from the planet surface, there are two forces acting on it, gravity and solar radiation pressure. The radiation pressure acceleration is the result of scattering of solar photons, which could be strong enough to accelerate atoms to escape velocity, producing a long anti-sunward tail (*Beth et al., 2016*). It is a function of the photon flux and of the solar photon scattering probabilities (g-value) (*Killen et al., 2009; 2022*).
In the specific case of Na, the effect of radiation pressure also depends on the velocity of the particle with respect to the Sun *(Smith and Marconi, 1995)*. As the planet orbits around the Sun, the effect of radiation acceleration can be seen in the variability of the intensity of the exospheric Na lines as they move around the deep of the solar Fraunhofer D-lines.
At Mercury, the radiation pressure acceleration can't be neglected and acts

differently on different species. Atoms with a surface ejection velocity of at least 2 km/s can acquire the additional velocity needed to reach the escape velocity of 4.25 km/s and thus begin their journey down-tail *Ip,1986; Smyth,1986; Smyth and Marconi,1995).*
It is effective in accelerating some species like Na *(Ip, 1986; Smyth, 1986).* Each time a Na atom scatters a solar photon, it recoils in the anti-sunward direction, shaping a tail that was observed out to about 16 Mercury radii *(Potter et al., 2002).* The observed Na intensity in the exosphere is modulated by the velocity of Mercury with respect to the Sun and by the variation of radiation pressure acceleration, which varies by more than an order of magnitude at Mercury due to the eccentric planet orbit. The combination of these factors shows a minimum Na emission at perihelion and aphelion, when the heliocentric radial velocity of the planet is zero. Meanwhile, the radial component of the planet's velocity increase along Mercury's orbit, causing the solar spectrum to shift towards longer and shorter wavelengths and reaching the maximum shift at the mid seasons at TAA equal to 90° and 270°, respectively *(Smyth and Marconi 1995; Baumgardner et al., 2008; Schmidt et al., 2012)* (Fig. 2.7). This demonstrates that Na tail is highly variable along Mercury's orbit and its extent strongly depends on the TAA.

2.11 Sticking

The surface released particles following ballistic trajectories could re-impact the surface. After re-impact, they may be re-emitted or they may stick. These particles may adsorb to the surface long enough to partially or fully adapt to the local surface temperature and then be re-emitted. Sticking to the surface results in loss from the exosphere but not from the regolith.
Sticking coefficient is the term used in surface physics to describe the ratio of the number of adsorbate atoms (or molecules) that stick to a surface to the total number of atoms that impinge upon that surface during the same period of time. The coefficient is a function of surface temperature and of the kinetic energy of the particles *(Yakshinskiy & Madey 2000; 2005).* It is also governed by the efficiency of the energy transfer between the incoming atom and the upper layer of the surface, which depends on various factors, including the capacity to bound to the surface materials. There are higher sticking probability of losing energy and being trapped for refractories, while volatile components are easily re-emitted.

CHAPTER 3

Modelling of Mercury's exosphere

In order to study Mercury's environment, we simulate the Na and Ca exospheres, discuss the different exospheric processes responsible for these volatile and refractory elements and compare the different exospheric spatial distributions. We describe the three-dimensional Monte Carlo model of the Hermean exosphere by *Mura et al 2007* (Virtual Activity (VA) SPIDER, Sun-Planet Interactions Digital Environment on Request, in the Europlanet-2024 programme), that includes all the major sources of generation and loss processes. In this work we reproduce the spatial distribution of Na exosphere and we upgrade the model to better describe the MMIV process to provide a refined 3D density distribution of the Ca Mercury exosphere, comparing our results with the available MESSENGER/MASCS observations.

3.1 Monte Carlo theory

Monte Carlo (MC) methods are a broad class of computational algorithms that rely on repeated random sampling to obtain numerical results. Their essential idea is using randomness to solve problems that might be deterministic in principle. In most cases, a system is evolved to a new state which is chosen from a randomly generated ensemble of possible future states. Then, using some criteria, this new state is accepted or rejected with a certain probability, that in general is the distribution of the unknown phenomenon.

This method, hence, calculates a series of possible relations that simulate the phenomenon under investigation. Calculation is well done if the average value of the simulated measurements is approaching to the true value.
Monte Carlo methodology is widely used in many different areas of science, often in physical and mathematical problems. In this work, we present a three-dimensional, single-particle Monte Carlo model of the Hermean exosphere, which has the advantage that different particle release processes from Mercury's surface can be modeled *(Mura et al., 2007)*. The model calculates the trajectories of particles ejected from which we obtain the spatial and energy distributions of exospheric particles. Furthermore, an analytical model is obtained by fitting the numerical data with parametric functions. In this way, it is possible to model the exosphere of Mercury for each source separately and we can investigate the role of each physical source independently of the others. The variability of surface or external conditions can be reproduced by changing physical quantities in the functions describing the source processes and, for each set of values, a different numerical simulation can be performed. In this way, a clear picture of the effects on the exospheric density due to different causes will emerge.

3.2 Modelling of surface release processes

The Monte-Carlo model includes, among the processes responsible of the formation of Mercury exosphere, the following ones:

- *Photon-Stimulated Desorption* results from the desorption of neutrals or ions induced by photon bombardment of the surface. The neutral flux of atoms extracted from planetary surface can be described as

$$\phi_{PSD} = Nc\phi_{\gamma}\sigma cos(\alpha) \tag{3.1}$$

  where ϕ_{γ} is photon flux, σ is the PSD cross-section, N is the surface density, c is fraction of the species, α is the angle from the sub-solar point, flux is obviously zero for $\alpha > 90°$. The intensity of the flux of ejected particles from Mercury due to PSD release is proportional to the total flux of proton precipitating onto the surface, so ϕ_{PSD} is a function both TAA, scaled to the square of heliocentric distance, and the assumed source velocity distribution. The energy spectrum of the

emitted atoms has a Maxwellian Boltzmann flux distribution function of energy E:

$$f(E) = \frac{E}{(k_B T)^2} e^{-\frac{E}{k_B T}} \tag{3.2}$$

- *Thermal desorption* is related to the binding energy of the atom on the surface and to the vibrational frequency of this bound atom, such that neutral flux of thermal desorption is given by:

$$\phi_{TD} = \nu N c e^{-\frac{U_{td}}{k_B T}} \tag{3.3}$$

where ν is the vibration frequency of the adsorbed atoms, T is the surface temperature and U_{td} the binding energy. The evaporated particles are in thermal equilibrium with the surface and the energy distribution of species ejected by TD process follows a Maxwell-Boltzmann flux distribution given by:

$$f(E, \theta) = 2cos\theta \frac{E}{(k_B T)^2} e^{-\frac{E}{k_B T}} \tag{3.4}$$

where θ its angle respect to the normal to the surface that takes into account the roughness of the surface.

- In *Ion Sputtering* process to reconstruct the H^+ flux onto the planetary surface we use a Monte-Carlo model of proton circulation in Mercury's dayside magnetosphere *(Mura et al., 2005; 2007)*. The precipitation region depends on IMF components that are an input of the model. The magnetic field is reconstructed by adapting a Tsyganenko T96 model of the Earth to Mercury's case *(Massetti et al. 2003)*. The distribution function of the ejection energy usually peaks at few eV *(Sigmund, 1969)*, and can be empirically reproduced by the following function:

$$f_s(E_e, T) = c_n \frac{E_e}{(E_e + E_b)^3} [1 - (\frac{E_e + E_b}{T_m})^{\frac{1}{2}}] \tag{3.5}$$

where E_b is the surface binding energy of the atomic species extracted, E_e the energy of emitted particles, c_n the normalization constant and Tm the maximum transmitted energy during the collisions. The resulting neutral differential flux is:

$$\frac{d\phi_n}{dE_e} = Y_C \int_{E_{min}}^{E_{max}} \frac{d\phi_I}{dE_i} f_s(E_e, E_i) dE_i \tag{3.6}$$

where Y is the process yield, ϕ_I the ion flux and E_i the impact energy.

- To evaluate the planet exosphere produced by a *Micro- Meteoroids Impacts Vaporization* event, we use the model to reconstruct the dynamical evolution of the exospheric particles produced by the impact. The *Mura et al. (2007)* model considers the initial velocity of the test particle with random direction and intensity according to the Maxwellian distribution:

$$f(v) = e^{-\frac{m_x v^2}{2k_B T}} \tag{3.7}$$

where m_x is the mass of the ejected particle x with a temperature T. *Cintala (1992)* introduced a function that describes the volume V of target material melted or vaporized by a projectile of mass μ and velocity v as:

$$V(v, \mu) = \frac{\mu}{\rho_p}(c + dv + ev^2) = V_p(c + dv + ev^2) \tag{3.8}$$

where ρ_p and V_p are the density and volume of projectile, respectively, while c, d and e are coefficients that depend on both the temperature of the soil and the composition of the projectile. For a species x the rate of the impact-vaporized mass $\frac{dm_t}{dt}$ $[\frac{part}{s}]$, as derived from equation 3.8, is given by

$$\frac{dm_t}{dt} = \frac{C_x}{Z_x}\frac{\rho_t}{\rho_p}\frac{dm_p}{dt}(c + dv + ev^2) \tag{3.9}$$

where C_x and Z_x are the numerical abundance in the regolith and the atomic number of the species x, respectively; the ρ_t is the density of the target and $\frac{dm_p}{dt}$ $[\frac{kg}{s}]$ the stream mass influx on Mercury's surface. The model requires the quantity $\frac{dm_t}{dt}$ as an input. In the *Mura et al. (2007)* simulations, the MMIV process was only responsible for the generation of atoms in Mercury exosphere, assuming a uniform distribution of the impact-vaporized mass.
In this work we model both the molecular and atomic exospheres generated by the MMIV process and estimate the mass ejected by meteoroid impact from the equation 3.9.

3.3 Modelling of loss processes

The source processes are balanced by loss processes, that reduce the concentration of elements in the exosphere

- In the *photoionization* process, photons eject one or more electrons from an exospheric particle turning it into an ion. In the model, each particle is assigned a photoionization lifetime τ, which depends on the species and varies along the planetary orbit. This loss processes do not remove particles, but they are taken into account by decreasing their assigned weight by a factor $e^{-t/\tau}$ for each step as a function of the parameter τ. The probability of the atom or molecule to be photoionized is calculated according to the position of the particle, in daylight or in darkness. In the shadow of the planet, no photoionization occurs and this process reduces the exospheric density on the dayside. The trajectories of the ionized particles are not calculated, but they are considered a net loss to the global amount of planetary exosphere.
  Instead, the released atomic groups (mainly after MMIV) can be further dissociated by *photodissociation* processes, thereby gaining energy. The extra energy of the products is different for each compound and it is converted into excess velocity, which is added to the velocity of the released molecules. The trajectories of the atoms are calculated until they end at the surface, or when they are too far from the planet. The photodissociation rate is considered to be equal to the inverse of the photoionization lifetime and is a function of the species and also the position of the planet. As with the photoionization process, the probability of dissociation of the molecules is calculated according to the position of the particle.

- The *radiation pressure acceleration* is function of the photon flux, g-values and of the amount of the Doppler shift out of the Fraunhofer features *(Smyth and Marconi, 1995)*. For an atom at Mercury, the magnitude of the acceleration due to radiation pressure is given by

$$a_r = \sum_i \frac{h g_i}{m \lambda_i} \tag{3.10}$$

  where h is Planck's constant, λ_i are the resonant transitions, and g_i are the g-values of each transition. Because radiation pressure depends on

the number of incident photons, obviously $a_r = 0$ for atoms in Mercury's shadow.
In this work, we assume two different approaches to estimate the radiation pressure for Ca and Na atoms.
We apply the equation 3.10 in the specific case of Ca atoms on Mercury *(Burger et al., 2012)*, and estimate the acceleration as

$$a_r = 0.28 \frac{g_{0352}(v_r)}{d^2} \tag{3.11}$$

where d is the distance of Mercury from the Sun in astronomical units (AU), and g is the g-value at 0.352 AU as a function of the radial velocity v_r relative to the Sun (*Killen et al., 2009; 2022*).
Hence, the radiation pressure acceleration for Na atoms is calculated using the empirical relation *(Mura et. al, 2012)*

$$a_r = \frac{1.25 \cdot 10^{24}}{r^2}[1 - 0.4525e^{-35.457\Delta\lambda^2} - 0.48388e^{-2.4467\Delta\lambda^2}] \tag{3.12}$$

where r is the distance from the Sun and $\Delta\lambda$ is the wavelength Doppler shift as a function of each particle's velocity v_x respect to the Sun according to the relation $\Delta\lambda = \lambda\frac{v_x}{c}$. The coefficients of the empirical formula are obtained by the optimization of *Smyth and Marconi (1995)* data.

3.4 Particles Dynamics

The model computes single-particle trajectories to reconstruct the spatial distribution of some components of the neutral exosphere of Mercury. A weight is assigned to the test-particle and, each time a test-particle crosses a grid cell, it is accumulated in the result matrix. The weight factor assigned to the Monte Carlo test particle is also continuously controlled along the trajectory, to take into account the loss processes of photodissociation and photoionization. At each time step, we calculate the probability for the molecules to dissociate, according to the position of the test particle, in dayside or in nightside, and we change the weight accordingly. Finally, the element density inside each grid cell is calculated taking into account the

number of test particles that have been accumulated in the cell, their weight factor, the time that each test particle actually experiences inside the cell and the volume of the cell.
The trajectories of particles are calculated by using the full equation of motion, including gravity force in Mercury reference frame and radiation pressure acceleration. The acceleration due to the radiation pressure acts differently over different species. It is believed to be relevant for Na, and negligible for Ca.
The test-particle trajectory ends at the surface of the planet. The exact value of the sticking coefficient for different species is not completely constrained. *Leblanc and Johnson (2010)* considered a sticking coefficient < 1 for Na, but we assume a conservative condition in the model and do not consider bouncing process (sticking factor $= 1$). Trajectory also ends if particles are too far from the planet, assuming that for this distance the planet gravity will not be enough to bound particles. Other loss processes is the photoionization that is taken into account by reducing particles weight. We usually trace the trajectories of one million test particles for each run using classical equations of motion and we assume that the variability of the surface or external conditions can be reproduced by changing parameters in the functions describing the source processes (section 3.2), and that a different numerical simulation can be performed for each set of values.

3.5 Modelling of Na exosphere

Ground- and space-based observations have shown that the spatial distribution of the Na Mercury exosphere varies between a configuration with two high-latitude enhancements in both the northern and southern hemispheres on the dayside of the planet and a configuration with a single bulge at the subsolar point *(Potter et al., 1999; Killen et al., 1999; Mangano et al., 2009, 2015; Orsini et al., 2018)*.
These different configurations can not be attributed to the effect of a single process, so it has been suggested that a multi-process mechanism *(Mura et al., 2023)* involving different processes is required to produce the observed spatial distribution.
As volatile species, the Na atoms are not strongly bound to the regolith and the Na surface composition is depleted by thermal and photon-stimulated desorption and by ion sputtering due to solar wind precipitation. To inves-

tigate the effect of these surface ejection processes on the morphology of the Mercury's exosphere, we reproduce the *Mura et al. (2007)* results simulating the Na exosphere generated by each process separately.
In the model, the trajectories are calculated by integrating the classical equations of motion, including gravitational force of the planet and the acceleration due to radiation pressure. In the Mercury's exosphere, Na is strongly subjected to radiation pressure. The atomic acceleration can be up to 54 % of the surface gravity and is a function of the photon flux and of the radial velocity of the test particle, so it is necessary to calculate this acceleration for each test particle step (eq. 3.12). Along the eccentric orbit of Mercury, the radiation pressure acceleration varies and at the same time also the photon flux, which is $3 \cdot 10^{15} cm^2/s$ at 1 AU, is scaled as $\frac{1}{r^2}$. Since the photon flux increases the surface release rate and it does not change the velocity distribution of the released particles, we have performed simulations with a constant value of the photon flux, equal to that at the Sun-Mercury distance assumed equal to be 0.38 AU.
In our simulations, the numerical element abundance c in the regolith is assumed to be uniformly distributed and equal to 5.3 atomic percent, while the regolith density N is equal $7.5 \cdot 10^{14} cm^{-2}$ (*Killen et al., 2001*).
Following the equation 3.1, we estimate the neutral Na flux assuming a PSD cross section of $2 \cdot 10^{20} cm^2$ *(Yakshinskiy et al., 1999)* and a surface temperature $T = 1500$ K. Instead, concerning TD, the process competes with PSD and sputtering, depleting the Na atoms in the surface layers of grains. Like PSD, TD depends strongly on the solar irradiance, as this affects the surface temperature, so the highest TD rate is expected to be close to the subsolar point. To include this effect in our simulation, the Na production rate from the equation 3.3 shows that the process is related to the $U_t d$ binding energy of the atom at the surface, which has a gaussian distribution between 1.4 and 2.7 eV, with a most probable value of 1.85 eV *(Leblanc et al., 2003)*, and to the vibrational frequency of this bound atom, which we set at $10^{13} s^{-1} of$ (*Hunten et al.,1988*).
Infine, we simulate the IS process due to solar wind protons by estimating the Na rate from the equation 3.6. According to the equation, it is necessary to know the ion flux to the planetary surface. Solar wind protons are expected to precipitate in the dayside cusps and the H^+ flux onto the surface of Mercury can exceed values of $10^9 cm^{-2} s^{-1}$ *(Massetti et al., 2017)*. The intensity of the H^+ flux depends on the magnetospheric configuration, which, in turn, depends on both the intrinsic magnetic field of Mercury and variable

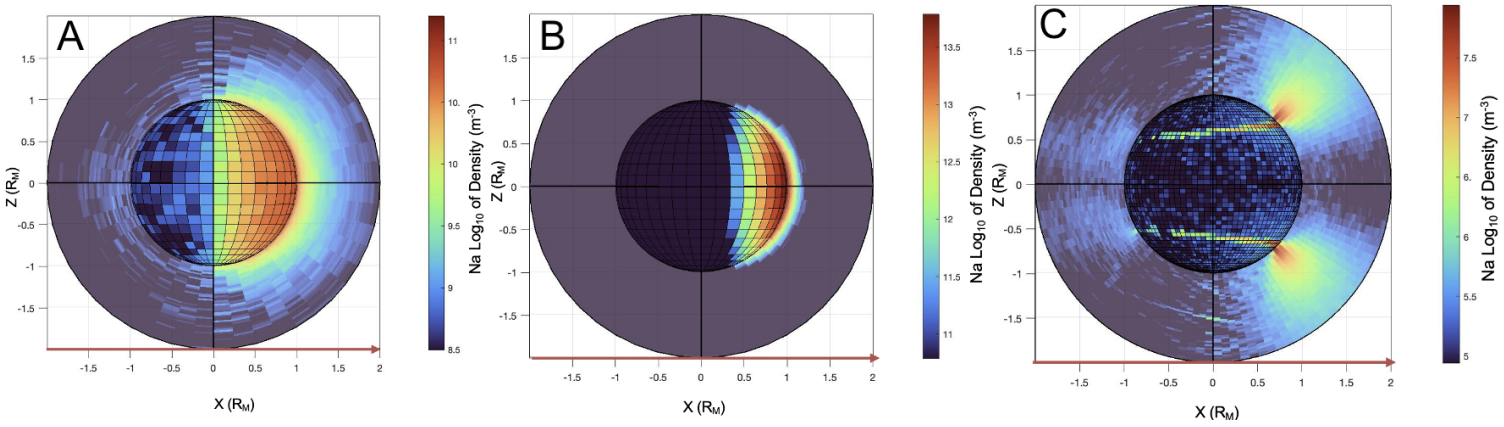

Figure 3.1: Exospheric Na density at TAA=0° for different release processes: photon-stimulated desorption (A); thermal desorption (B); ion-sputtering (C). The x and y axes are oriented according to the Mercury Solar Orbital (MSO) coordinate system. In this MSO frame, x is directed from the planet's center to the Sun (red arrow), y is in the plane of Mercury's orbit and positive opposite to the planetary velocity vector, and z is positive toward north.

external parameters, such as the Interplanetary Magnetic Field (IMF), solar wind velocity and density.

Using these assumptions, we run the simulations and show the results in terms of the total exospheric Na content at Mercury generated by PSD, TD and IS processes (Fig. 3.1).

The PSD exospheric distribution, panel A, it is distributed on the dayside where the surface is exposed to an intense flux of photons with a maximum density about $5 \cdot 10^{10} m^{-3}$.

On the dayside also the Na population from TD process is also present. As for the PSD, the TD depends strongly on the Sun's irradiance, since this affects the surface temperature, so that the highest TD rate is close to the subsolar point. Panel B shows that the desorbed atoms remain close to the surface. The very dense exosphere in the dayside with a maximum value about $5 \cdot 10^{13} m^{-3}$, makes TD as the most efficient desorption process at subsolar low altitude, but at the same time it is not effective in the global loss from the planet.

Panel C shows the Na exosphere produced by H^+ sputtering, which shows two maxima with densities up to $10^8 m^{-3}$ in the dayside at approximately $\pm$

45 of latitude, where we expect an enhancement of proton precipitation. As local characteristics, the double peaks in the dayside due to plasma precipitation are consistent with Na observations.
This analysis gives a picture of the effects on the exospheric Na density due to different source processes giving an view of the global loss from the planet.

3.6 Model assumptions for Ca exosphere generated by MMIV

3.6.1 Global Micro-Meteoroids Impact Contribution

By considering the new studies on the MIV release process (*Killen, 2016; Plainaki et al; 2017)*, we modify the exospheric model *(Moroni et al, 2023)*. In the simulations, the energetic Ca atoms are generated by instantaneous process from dissociative recombination, so test particles are described in the same section as launched from the surface. Ca and O test particles, as products of CaO photo-dissociation (section 2.8.1), are initialized by assuming that the photolysis process results in an extra energy, which is translated into an excess velocity for Ca and for O in the rest frame of the original molecule. These two excess velocities are given a randomly chosen direction and are added to the velocity of the parent CaO molecule.
The trajectories of particles ejected after impacts are calculated by using the full equation of motion, including gravity force in Mercury reference frame and radiation pressure acceleration. Since Ca atoms in Mercury' exosphere are highly energetic, with an extreme velocity with respect to the planet *(Burger et al., 2014)*, the doppler shifts of the lines could be different than what it would be when Ca is at rest with respect to the planet. For this reason, we did include the radiation pressure calculation in our model (eq. 3.11), by using the values given by *Killen et al. 2009* and *Burger et al. 2012*. In the model, in addition to the Ca resonance line at 422,7 nm, also the lines at 272.2 nm and 456.7 nm are included in the radiation pressure calculation although they contribute less to the total effect *(Burger et al., 2012)* and we calculate the acceleration due to the radiation pressure estimating it at each step of the test-particle trajectory.

We investigated in detail the effect of radiation pressure acceleration, that acts in the anti-sunward direction and produces an increase of exosphere density in the night side and a reduction in the dayside. As a probe of this we

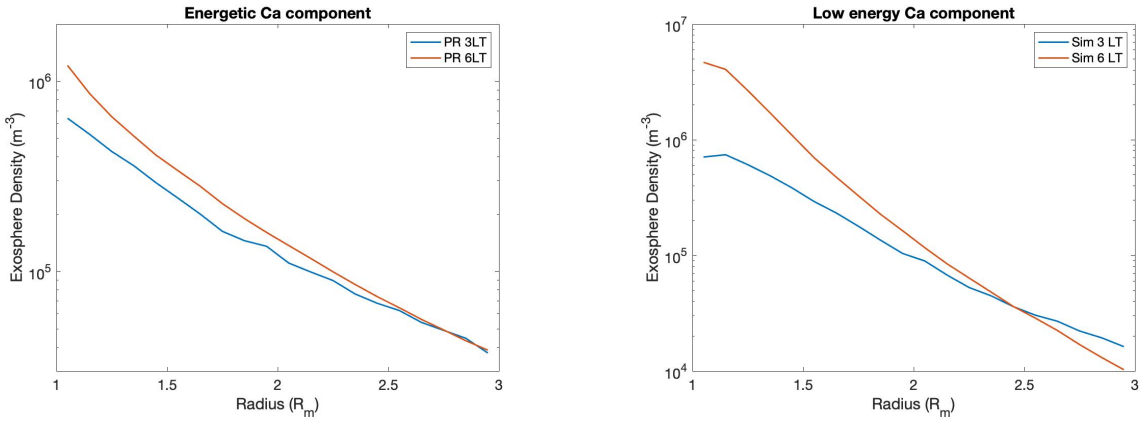

Figure 3.2: Comparison of the vertical density profiles for the low energy (left plot) and energetic Ca (right plot) components as a function of altitude expressed in Mercury radii at TAA = 60° for local time equal to 3 hr (Blu lines) and 6 hr (red lines)

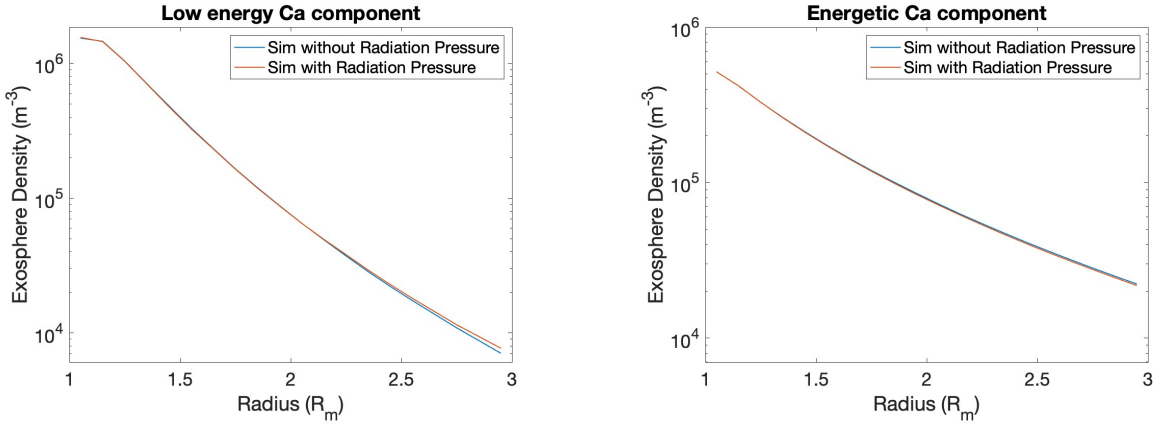

Figure 3.3: Comparison of the vertical density profiles for the low energy (left plot) and energetic Ca (right plot) components as a function of altitude expressed in Mercury radii at TAA = 60°, assuming the radiation pressure effect (red lines) and removing this force from the model (blue lines)

reproduced the vertical density profiles for low energy and energetic Ca components in the interval 1 - 3 Rm at TAA = 60° (Fig. 3.2), where the radial component of the velocity is close to its maximum along the orbit and we compared the results obtained for Local Time equal 3 hr (night-side) (blue lines) and 6 hr (dawn) (red lines). From the profiles we can observe low value of Ca density at low altitudes in the night-side, while the 3 hr profiles becomes more intense than the 6 hr ones at higher R_m. So, the model reproduces the radiation pressure effect that accelerate particles in the dayside towards the tail. At the end, to evaluate the effect of the radiation pressure on the final results, we show in Figure 3.3 a comparison of the vertical profile for low energy and energetic Ca components in the interval 1-3 Rm at TAA = 60° between the assumption of the radiation pressure effect (Red Lines) and removing this force from the model (Blue Lines). We concluded that this modelling effort produced very little refinement of the simulated Ca profiles (the difference between the Ca profiles with or without radiation pressure ranges from 0 % at the surface up to $\sim$ 14 % at 3 R_m).
In order to simulate the Ca Mercury exosphere, we assume the numerical Ca abundance in the regolith equal to 3.5% atomic percent *(Killen, 2016)* and we suppose that all the Ca is bounded to O, as CaO. The MESSENGER/X-Ray Spectrometer (XRS)-derived maps *(Weider et al. 2015)* showed that there are some regions where the Ca content on the Mercury's surface can be as high as 0.07, but for simplicity we assume a homogenous value for the Ca abundance.
In the plume after the impact, we must consider that a fraction of Ca-containing species is in the gas phase and part is in the solid phase as dust. The ratio between content of species in the gas phase to the total amount of Ca-containing species in gas and solid phases, is estimated to be lower than 0.05 *(Berezhnoy et al. 2011)*. From this percentage we evaluate the fraction of atomic Ca and molecular CaO involved in the different processes. The resulting components at quenching temperature are considered in the ratio of 1:3 *(Berezhnoy, 2018)*.

We first assume an isotropic source of Ca over Mercury's surface, making a comparison between such source and data observations. Subsequently, we suppose an asymmetric particles precipitation as discussed in *Pokorny et al. (2018)* (Fig. 3.4). In this work they compute the total mass ejected via micro-meteoroids that impact the surface and, in this paper, we consider only the percentage of Ca bearing particle abundance. Then, we simulate the exospheric energetic Ca component generated by the shock-induced non-

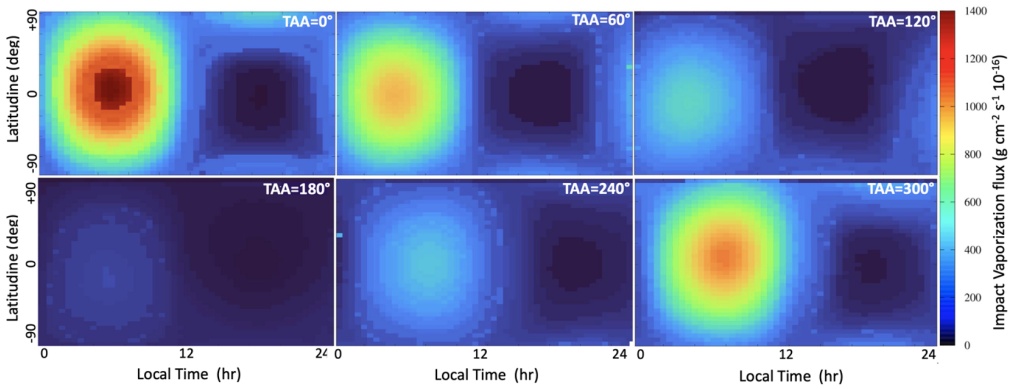

Figure 3.4: Maps of impact vaporization flux for six different TAAs by Pokorny et al. (2018)

equilibrium dissociative ionization process followed by the neutralization. The efficiency of the neutralization process decreases with decreasing temperature of vapor cloud, so the bulk of the process should occur just after the initial impact, i.e. in timescales negligible with respect to cloud expansion *(Killen, 2016)*. Hence, we assume that the velocity distribution of a fraction of total Ca immediately released to the exosphere during impacts of meteoroids is reproduced by the Maxwellian velocity distribution at 50,000 K *(Burger et al. 2014)*.

The photo-dissociation of the CaO molecules generate the low energy Ca component. In this work we examine and compare two different studies: on the one hand, at quenching temperatures $\leq$ 3750 K $Ca(OH)_2$ dominates over both atomic Ca, CaO and CaOH *(Berezhnoy, 2018)* and it is valid to assume as the main Ca-containing compound in the impact-produced cloud. At 1 AU CaO photolysis lifetime is estimated between 140 s and 3000 s *(Valiev et al., 2017)*; we adopted lifetime $\tau_{CaO} = 140s$ *(Valiev et al, 2016, Berezhnoy,2018)* and we assume that the CaO in the exosphere is produced by a subsequent photolysis processes of $Ca(OH)_2$ and then Ca(OH) (lifetime equal 2000 s and 600 s, respectively) *(Berezhnoy 2013; 2018)*. Starting from the photo-dissociation of these molecules, we estimate a final CaO dissociation time $\tau_{Ca-bearing} \sim 270s$, calculated at Mercury distance as the sum of scaled lifetimes of each reaction. This value is shorter than the ballistic time of molecules 760 s *(Killen, 2016)*, so we expect that the fraction of CaO molecules photolyzed is close to unity. In the model we consider the

additional energy of Ca atoms during $Ca(OH)_2$, CaOH, and CaO photolysis (0.9 eV, 0.3 eV and 0.6, respectively) and the photodissociation of molecules would result in a total energy gain of about 1.8 eV for Ca *(Berezhnoy, 2013; 2018)*. From these assumptions, a low energy Ca component is ejected with temperature equal $\sim$ 20 000 K (details in Table 3.1).
On the other hand, at quenching temperatures $\geq$ 3750 K, we assume that the fraction of Ca-bearing particles is ejected as CaO at T $\sim$ 4000 K. CaO lifetime is about $\tau_{CaO} \sim 10^4 s$, equal to the inverse of the photodissociation rate ($7.5{\cdot}10^{-5} s^{-1}$ near the perihelion) and it is function of the orbital distance, and photodissociation of molecules would result in an energy gain of about 0.8 eV for Ca *(Killen, 2016)* (details in Table 3.2).
The Ca photoionization lifetime, τ_{Ca}, at Mercury varies from 1380 s at perihelion to 3120 s at aphelion *(Burger et al., 2014)* and in the current simulations we have assumed this parameter as a function of the orbital distance of the planet. A summary of the model assumptions is given in Table 3.3.

Molecules	**Reactions**	**Life time** $\tau(s)$	**Energy (eV)**	**T products**
Quenching T				$\leq$ 3750
$Ca(OH)_2$	$Ca(OH)_2$ +h ν = CaOH +OH	200	0.9	$\sim$ 10000
$Ca(OH)$	$Ca(OH)$ +h ν = CaO + H	60	0.3	$\sim$ 3000
CaO	CaO +h ν = Ca + O	14	0.6	$\sim$ 7000

Table 3.1: Photolysis lifetimes $\tau(s)$ calculated at Mercury distance, energies and temperature of metal-containing products of photolysis of Ca-containing species. Assumptions from Berezhnoy (2013; 2018) and Valiev et al. (2016)

Molecules	**Reactions**	**Life time** $\tau(s)$	**Energy (eV)**	**T products**
Quenching T				$\geq$ 3750
CaO	CaO +h ν = Ca +O	10000	0.8	$\sim$ 10000

Table 3.2: Photolysis lifetimes $\tau(s)$ calculated at Mercury distance, energies and temperature of metal-containing products of photolysis of Ca-containing species. Assumptions from Killen (2016)

CaO and Ca Abundance		
Element Abundance	**Value (%)**	**References**
Surface composition Ca	3.5	*Killen et al 2014*
Ca-containing species gas phase	5	*Berezhnoy et al 2011*
Molecular Ca as CaO	75	*Berezhnoy, 2018*
Atomic energetic Ca	25	*Berezhnoy, 2018*
Parameters of process responsible for Ca exosphere formation		
Energetic Ca component	**CaO component**	**Low energy Ca component**
	Cloud Quenching Temperature $\leq$ *3750*	
T_{Ca}= 50 000 K t=t_0^* $\tau_{Ca} \sim ns$ Ca fraction at t_0 = $3.5\% \cdot 5\% \cdot 25\%$	T_{CaO} = 13 000 K t=t_0^* $\tau_{Ca-bearing} \sim 270s$ CaO fraction at t_0 = $3.5\% \cdot 5\% \cdot 75\%$	T_{Ca} = 20 000 K t=t_0^*+ 270 s τ_{Ca} ∼ from 1380 s to 3120 s
	Cloud Quenching Temperature $\geq$ *3750*	
Ca fraction at t_0 = $3.5\% \cdot 5\% \cdot 25\%$	T_{CaO} = 4000[1]K t=t_0^* $\tau_{CaO} \sim 10000^1 s$ CaO fraction at t_0 = $3.5\% \cdot 5\% \cdot 75\%$	T_{Ca} = 10 000 K t=t_0^*+ 10000 s τ_{Ca} ∼ from 1380 s to 3120 s

*t_0 = meteoroid impact time

Table 3.3: Assumptions used for the simulated energetic Ca component derived from the dissociative ionization and neutralization of Ca^+ and the low energy Ca component generated by the photodissociation of the released Ca-bearing molecules. References: 1-assumptions of Killen (2016)

3.6.2 Comet stream contribution

Burger et al. (2014) studied the Ca seasonal variability from the analysis of MACS measurements showing a persistent enhancement in Ca emission after Mercury passes through its perihelion, near TAA ∼ 25°, and identified a minor peak in the Ca source rate at TAA ∼ 160°.
A plausible hypothesis to explain the Ca excess was attributed to the vaporization of surface material induced by the impact of a meteor stream, possibly resulting from Comet Encke *(Christou et al., 2015* and *Killen and Hann, 2015*). 2P/Encke is related to several strong meteor showers, the so-called Taurid complex *(Whipple, 1940; Porubcan et al., 2006).* It has the shortest orbital period among periodic comet families equal 3.3 years at 0.026 AU from Mercury orbit, so the planet should intercept its meteoroid stream *(Christou and Asher, 2009).*

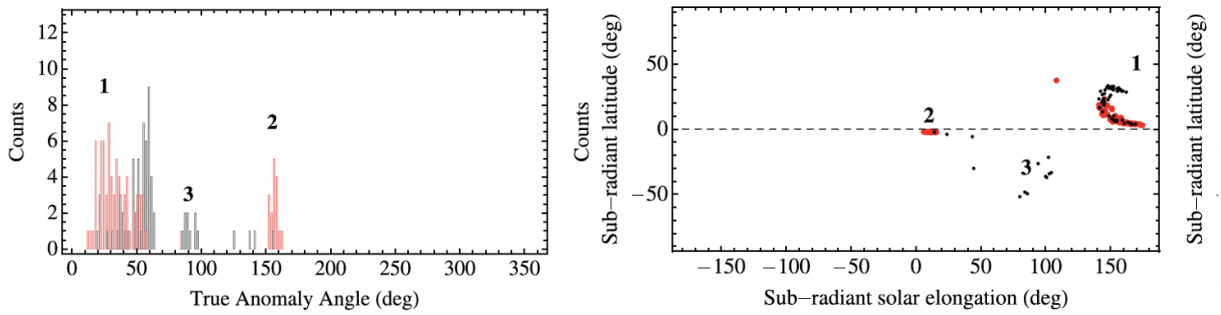

Figure 3.5: Spatial geometry of slow (red) and fast (black) population from comet Encke that impact Mercury surface: number of particles as a function of the TAA (left panel); particles distribution on Mercury surface (right panel), the dashed horizontal line represents planet's equatorial plane (Christou et al., 2015)

Christou's works established that meteoroids ejected 1-2 $\cdot 10^4$ years ago by a possibly Encke progenitor broke up impacting the Mercury surface. They suggested the presence of two different kind of population: particles ejected with v_{ej} <10 m/s are called "slow" population, and particles with 10 < v_{ej}< 100 m/s are identified as "fast" population. It is possible to reconstruct the arrival geometry of these different population as illustrated in Figure 3.5 from *Christou et al. (2015)*. Slow particles have arrival velocity at Mercury in the range 32 - 37 km/s and generate a group after perihelion at TAA between 10° and 60° (Group 1) and another near aphelion at TAA $\sim$ 150° (Group 2). Instead, fast particles produce two groups with TAA $\sim$ 60° and TAA $\sim$ 90° (Group 3). In any case slow ones dominate in number. The right panel shows Mercury surface and the point of particles impact: position of Group 1 agrees with Ca enhancement and particles arrive from the antisolar direction at north of the equator, while Group 2 impact planet surface in the dayside. Starting from the assumptions about the Ca generation processes described in section 3.6.1, we assume a quenching temperature < 3750 K and we reproduce spatial distribution of Ca components generated through MIV caused by the comet Encke's stream particles intersecting the orbit of Mercury. The assumed exospheric population released from the surface upon meteorite impact includes CaO molecules, responsible of the low energy Ca generation, and the energetic Ca component.
We simulate the bombardment of planet surface considering only the slow population of Group 1 and Group 2 to reproduce the Ca enhancement at

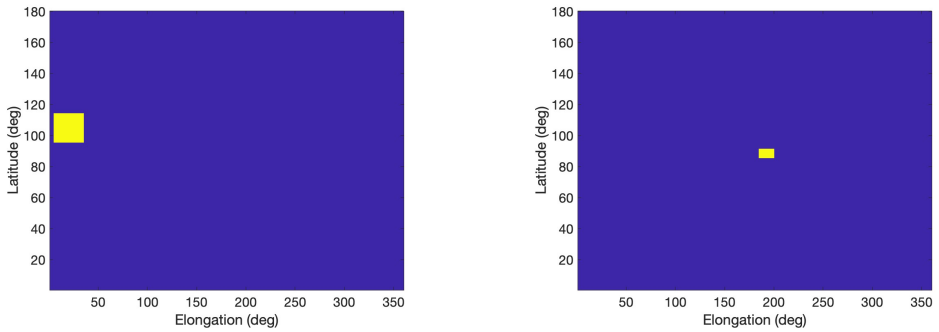

Figure 3.6: Replication of the impact directions for Encke's stream particles from a specific area upon the Mercury surface estimated by Christou et al. (2015)

TAA = 30° and 150° due to the contributions from the stream. We estimate the rate of impact-vaporized mass (eq. 3.9) assuming a total stream mass influx on Mercury's surface equal to 10.5 g s^{-1} and meteoroid impact velocity v = 35 km/s (*Christou et al., 2015).* The impact meteoroid directions were estimated by *Christou et al. (2015)* assuming that particles are emitted from a specific area upon the surface extending from 5° to 23° in latitude and from 145° to 175° in solar elongation (elongation = 0° corresponds to the planet-Sun direction) for Group 1, while the Group 2 is located in the planet surface extended from -5° to 0° in latitude and from 5° to 20° in solar elongation (Fig. 3.6).

3.7 Ca simulation results

In order to reproduce the Mercury Ca exosphere in Figure 3.7 we show the simplest case: the simulated CaO exosphere (left panel) released by micrometeoroids impacts and the subsequent Ca exosphere (right panel) generated from photodissociation of the molecules assuming that the precipitating particles have a uniform distribution on the surface. Our results suggest that an isotropic Ca source with temperatures of 50000 K creates exospheres with densities up to $2 \cdot 10^6 m^{-3}$ with a uniform distribution in the x-y plane, showing no dawn-dusk asymmetry, so it doesn't reproduce the spatial distribution that is observed by UVVS. An isotropic exospheric model, therefore, cannot actually describe the observed persistent, high-energy source of calcium, enhanced in the dawn equatorial region of Mercury, has to be considered, as

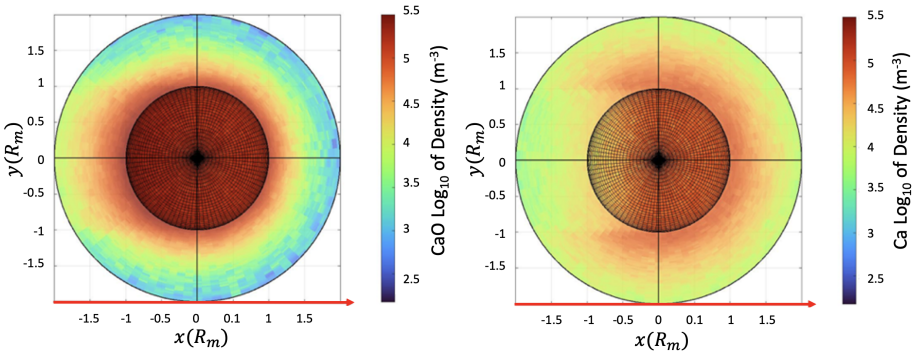

Figure 3.7: Simulations of CaO (left) and low energy Ca (right) exospheres at TAA=0° by micrometeoroid impacts assuming a uniform distribution of the ejected species. The x and y axes are oriented according to the MSO coordinate system (see Fig. 3.1 caption)

previously suggested also by *Burger et al (2012; 2014)* (Fig. 2.6).

Then, we consider a non-uniform precipitation of micrometeoroids to the planet surface and, as explained in the model assumptions (Section 2.5.1), we use *Pokorny et al. (2018)* maps of impact vaporization flux (Fig 3.4) at different TAA in order to derive the released CaO and Ca components. In these maps, the most intense impact vaporization region is centered at the dawn terminator ($\sim$ 6 AM) both at perihelion and aphelion and it is slightly shifted when Mercury is moving along the orbit. The derived energetic Ca exosphere (T = 50000 K) generated from the dissociative ionization and neutralization of Ca^+, for 4 different values of TAA, is presented in Figure 3.8. Densities up to $10^6 m^{-3}$ are reproduced above the region of maximum emission located on dayside hemisphere, that shows an evident dawn-dusk asymmetry with highest densities when Mercury is at perihelium.

We then simulate the low energy Ca component generated by photo-dissociation of molecules. We show in Figure 3.9 the results obtained by assuming $Ca(OH)_2$ as the main Ca-containing compound in the impact-produced cloud.

The CaO exosphere is produced as a product of the subsequent photolysis processes of $Ca(OH)_2$ in Ca(OH) and then in CaO. In this case, the CaO density is up to $10^7 m^{-3}$ above the surface in the dawn hemisphere where the molecules are preferentially ejected. The subsequent photo-dissociation of CaO that generates the Ca exospheric contribution at T = 20 000 K

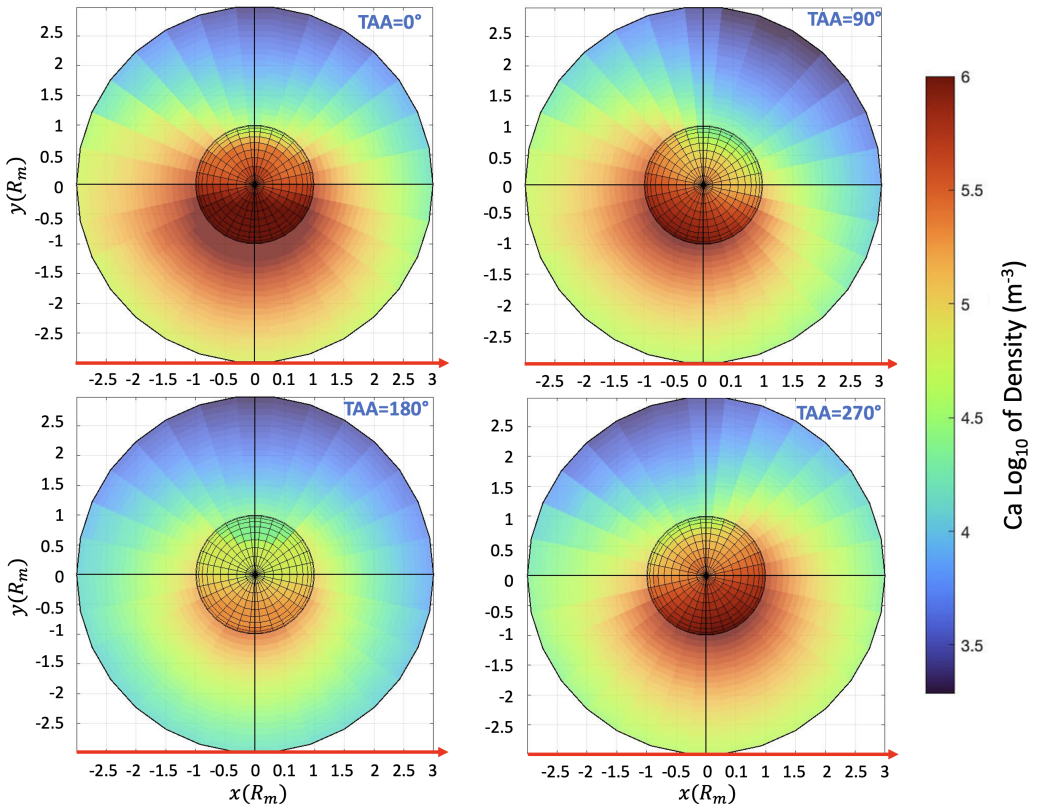

Figure 3.8: Energetic Ca component at T= 50,000 K at different TAA (0°, 90°, 180° and 270°) generated through impact vaporization and subsequent dissociative ionization and neutralization of Ca^+, assuming an anisotropic precipitation of meteoroids. The x and y axes are oriented according to the MSO coordinate system (see Fig. 3.1 caption)

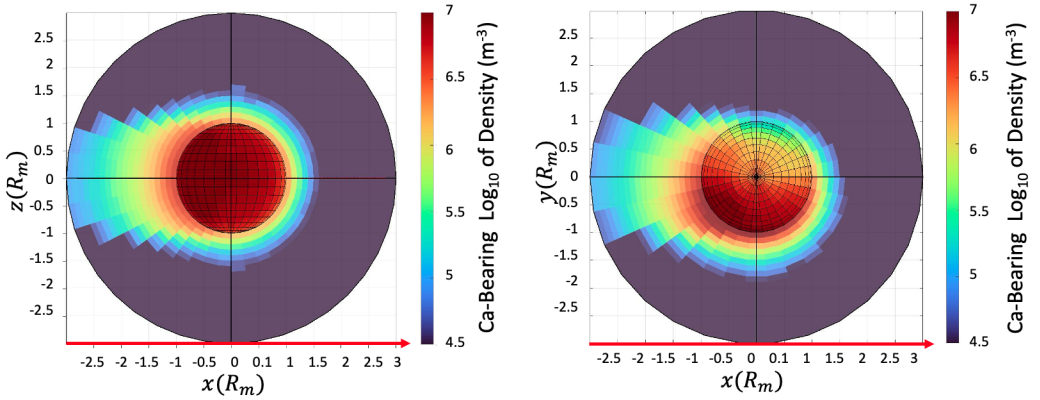

Figure 3.9: Spatial distribution of Ca-bearing molecular densities at TAA = 0° generated by MMIV, assuming an anisotropic precipitation of meteoroids (Fig. 3.4). The x and y axes are oriented according to the MSO coordinate system (see Fig. 3.1 caption). Left panel reproduces the dawn hemisphere of Ca-bearing exosphere and right panel shows the north pole of planet

(Fig. 3.10) with densities up to $10^7 m^{-3}$. The Ca enhancement is evident in the dawn-side where molecules are dissociated by sunlight and the trend of exospheric densities at different TAA shows the highest value at perihelion (TAA=0°) near dawn and a minimum value at aphelion (TAA = 180°). We can observe a different spatial distribution of two Ca components (Fig. 3.8 and 3.10): while the energetic component is distributed in the whole hemisphere at dawn following the micrometeoroid's precipitation, the photodissociation process responsible of low energy Ca depends on sunlight and generates a denser exosphere in a smaller region, mainly at post-dawn.

The 3D plot in Figures 3.11 shows the global Ca exosphere as the sum of both components, giving an overview of planet environment. There is an evident dawn-dusk asymmetry, as seen from the top-right figure (panel A) and from the midnight view (panel C), in agreement with the MESSENGER results; from dawn view (panel B), we can note that there is an enhancement in the post-dawn side where the two components maximize.
In Figure 3.12 we plotted the vertical profile of total CaO and Ca components in the interval 1-3 R_m at TAA = 0° above the dawn terminator making a comparison between simulation results obtained with assumption of quenching temperature of the cloud $\leq$ 3750 K (left panel) with the study at higher temperatures ($>$ 3750) (right panel). In the former, it can be noted that

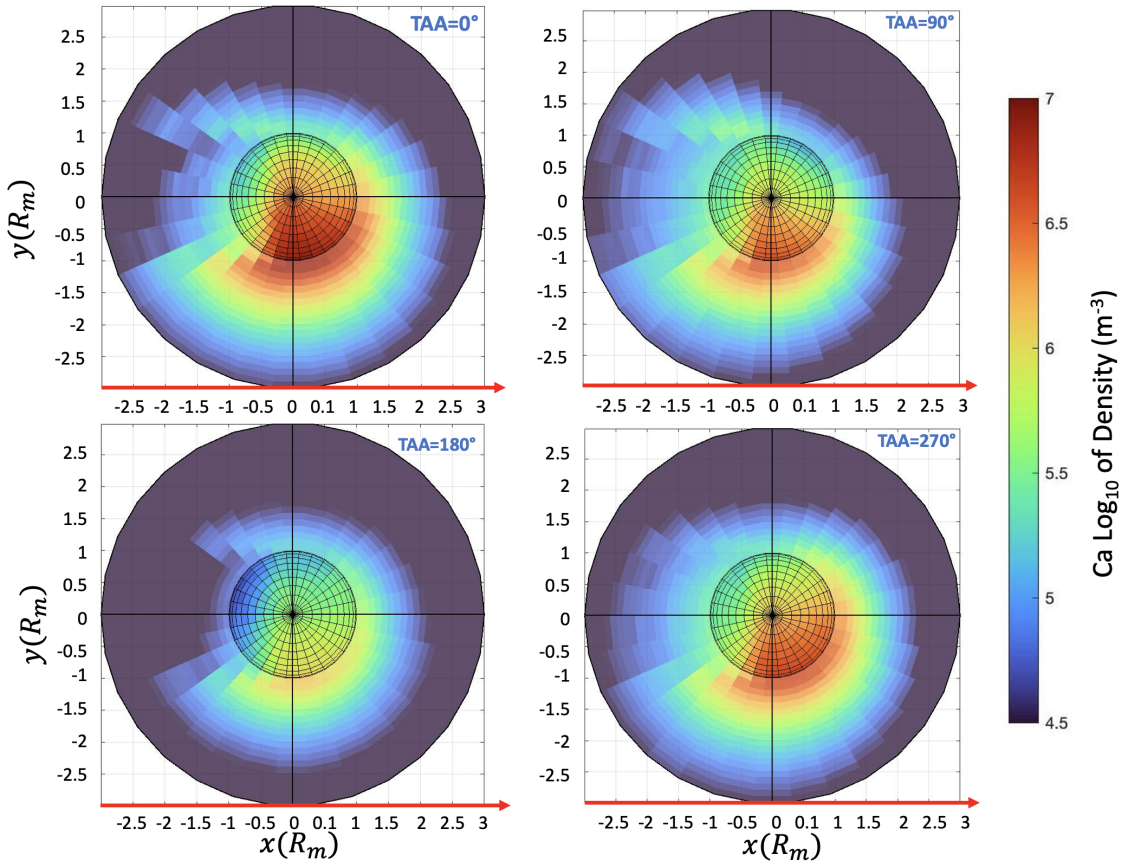

Figure 3.10: The low energy Ca exosphere of Mercury at different TAA generated through the photodissociation of the CaO component. The x and y axes are oriented according to the MSO coordinate system (see Fig. 3.1 caption)

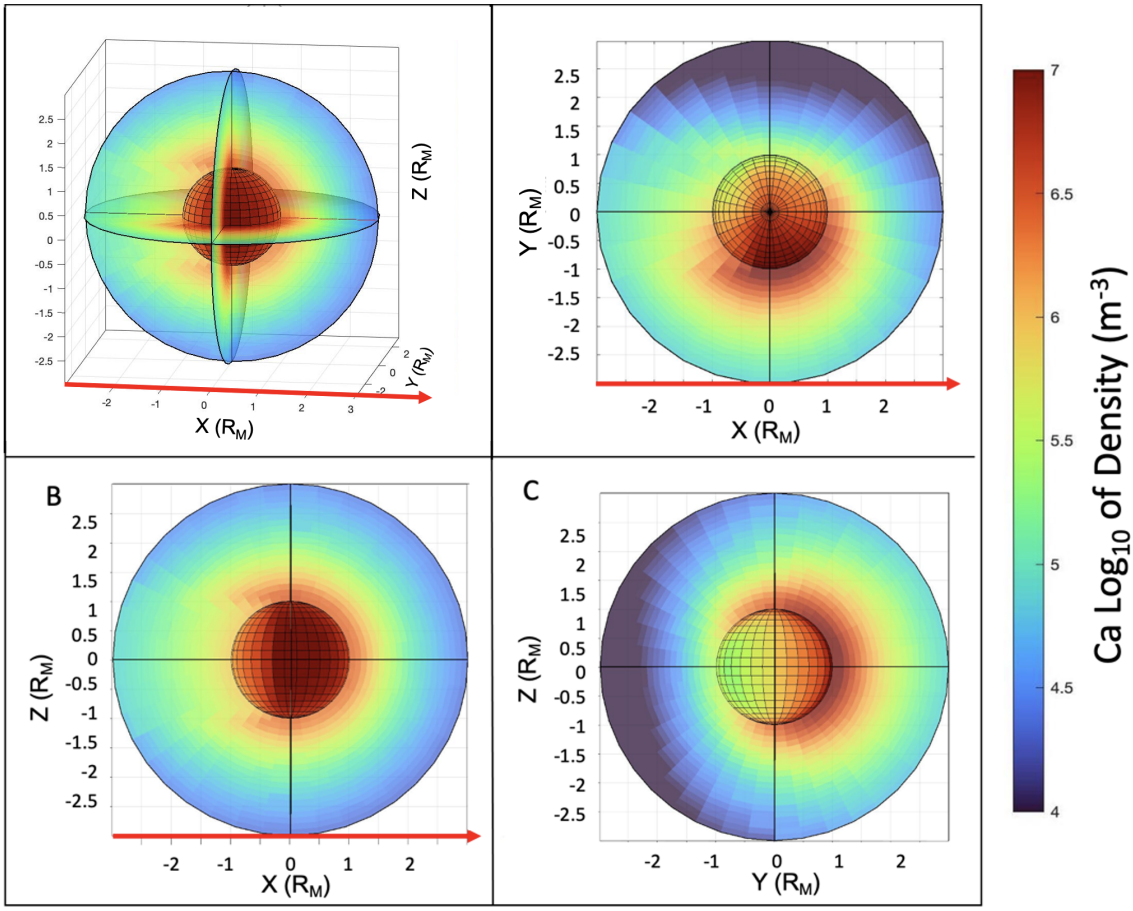

Figure 3.11: 3D plot of Ca exosphere considering the contributions of both Ca components at perihelion. Panel A-B-C represent the projection of planet's exosphere along the direction x-y-z oriented according to the MSO coordinate system (see Fig. 3.1 caption); red line points to the Sun

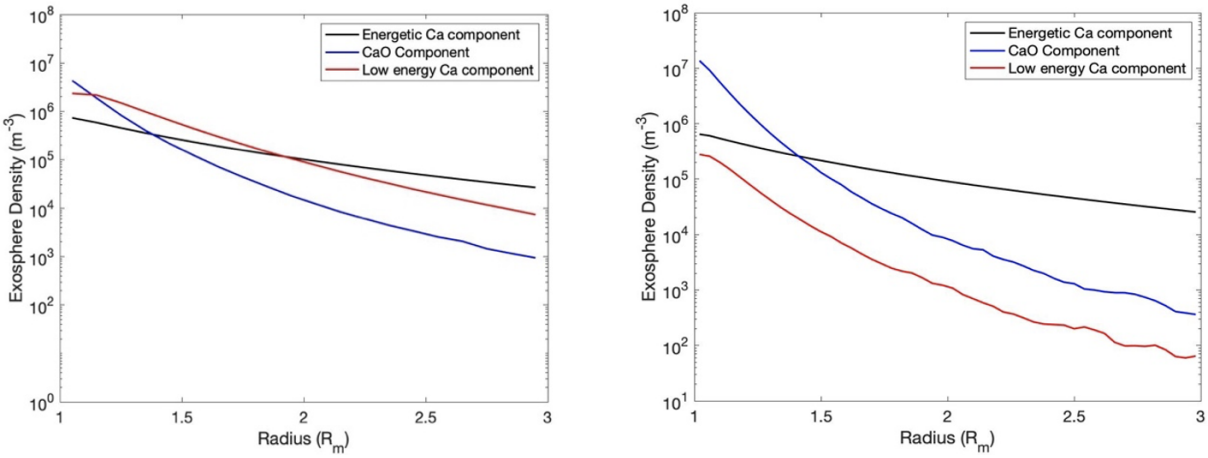

Figure 3.12: Vertical density profiles of the CaO and the Ca components in the range up to 2 R_m (Mercury radii) above the surface, at perihelion (TAA=0°) assuming a vapor cloud quenching temperature ≤3750 K (left panel) and > 3750 K (right panel)

the low energy Ca component, produced by the subsequent photolysis processes, dominates over the other at low altitudes (up to 2 R_m) but the trend changes at higher RM values showing that the energetic Ca generated by the non-equilibrium dissociative ionization and neutralization processes becomes denser. The resulting Ca exosphere is composed by two distinct populations at energy about 20.000 K and 50.000 K. Instead, in the right panel, the exosphere due to energetic Ca is denser than the low energy Ca at all altitudes, thus the Ca exosphere has a single predominant component, and the CaO exospheric profile is steeper.

Finally, our results of the MMIV-generated Ca exosphere are compared to the total Ca component as produced by the different processes with the profile by *Burger et al. (2014)* obtained through a best fit to the UVVS observations over two years (March 2011-2013).
If we plot the seasonal dependence of total Ca content in the exosphere (Fig. 3.13), model results are consistent with the UVVS observations in the approximation of a temperature cloud ≤ 3750 K and Ca-bearing photolysis lifetime $\tau_{Ca-bearing} \sim 270s$ (red line). At the contrary, the Ca exosphere estimation with higher temperature and photolysis lifetime assumptions (purple line) shows results lower by a factor of 2 than those obtained by *Burger et*

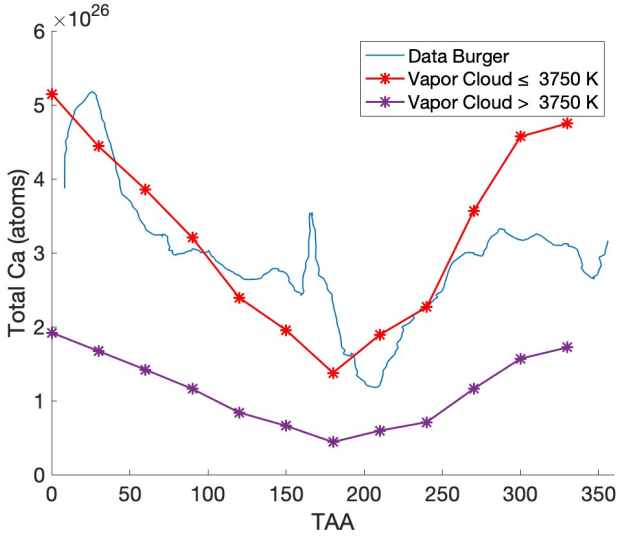

Figure 3.13: Comparison between the simulations results obtained in the approximation of temperature vapor cloud ≤ 3750 K (red line) and at higher temperatures (purple line) with the observations (Burger et al. (2014); blue line) along the orbit and, hence, TAA

al. (2014). The plots reproduce a peak at perihelium and a minimum value at aphelion. At aphelion photon flux is minimum, decreasing with the inverse square root of the distance, so that the Ca lifetime in the exosphere is the longest (lower photo-ionization) and the efficiency of photodissociation of CaO is the lowest. In the same orbit position, also the micrometeoroid flux is minimum, so that also Ca production via MMIV is the lowest. In the end, we have a combination of all these factors, a lower production rate and a lower loss rate. The final result is a less dense Ca exosphere.

The excess emission in the Ca profile by *Burger et al. (2014)* near TAA ∼25° and TAA ∼180° was attributed to the vaporization of surface material induced by the impact of a meteor stream, possibly resulting from Comet Encke *(Killen and Hahn 2015)*. We study the bombardment of the surface by particles from comet 2P/Encke simulating the expected spatial distribution of Mercury's Ca exosphere. We consider a precipitation of micrometeoroids located in the specific area according to *Christou at al. (2015)* (Fig. 3.6) and described in the section 3.6.2. We reproduce the Ca enhancement including both the low energy and energetic Ca component, respectively generated by photodissociation of molecules and by the dissociative ionization and neutral-

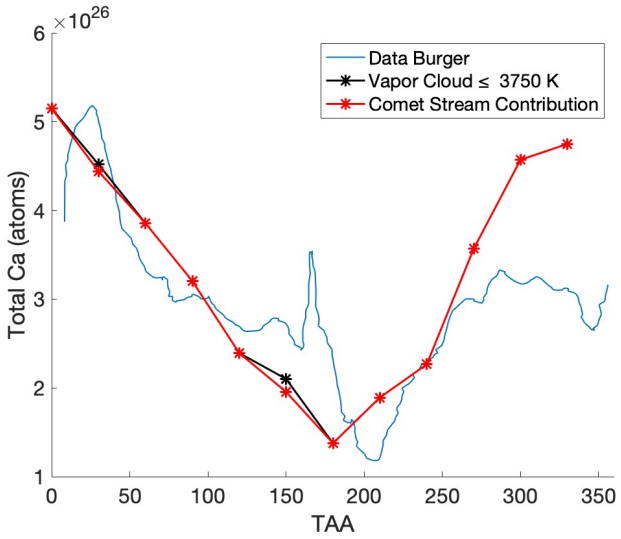

Figure 3.14: Comparison between the observations (Burger et al. (2014); blue line) and the simulations results obtained in the approximation of temperature vapor cloud $\leq$ 3750 K (red line) along the orbit and, hence, TAA , including the comet contribution (black line)

ization of Ca^{+}. In Figure 3.14 we plot the seasonal dependence of the total Ca content in the exosphere including the comet contribution, compared to the observations.
Although we use the same assumptions about the processes involved, the temperature cloud and the photolysis lifetime of the molecules, the simulated cometary contribution does not seem to be consistent with the data. We obtain values lower than the observations. The underestimation of the cometary contribution could be related to an underestimation of the impact velocity of the micrometeorites or of the total stream mass influx on the planet, or it could be due to not uniform surface Ca composition. Moreover, the arrival geometry of cometary particles could be different than assumed in our simulations. This study requires further investigations to find the set of input parameters able to reproduce the observed Ca content. Recently, *Chaufray et al. (2022)* suggest that the pick observed at TAA $\sim 25^{\circ}$ in Ca and Mg exosphere as obtained by MASCS observations could not be real, but it could be due to an artifact in the data analysis.

CHAPTER 4

Elements of Earth exospheric and magnetospheric processes

In order to study Earth's environment, we focus on the process of charge exchange between the exosphere and the magnetospheric ions, which produces Energetic Neutral Atoms (ENA). The ENA imaging technique is recognized as a powerful tool to remotely study global plasma phenomena in the planet environment attracted the interest both in the terrestrial and extraterrestrial space exploration missions. In detail, we give an overview of space missions dedicated to the ENA detection from different regions of Earth's magnetosphere, which have monitored the global dynamics and the spatial and temporal evolution of the plasma components.

4.1 The Earth's Magnetosphere

The Earth's magnetosphere is part of a dynamic, interconnected system that responds to solar and planetary conditions (Fig. 4.1). The magnetosphere is a cavity around Earth that is permeated by the magnetic field and composed by low density plasma. It protects the Earth from the direct impact of dense solar wind to the upper atmosphere. The dayside magnetosphere is constantly compressed by the solar wind and the boundary between the solar wind and the magnetosphere is called magnetopause *(Safrankova*

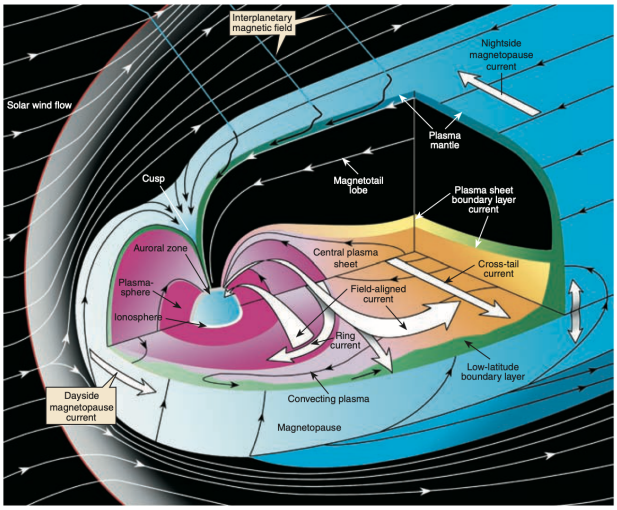

Figure 4.1: Three-dimensional scheme of the principal boundaries, regions, and current systems of Earth's magnetosphere (Kivelson and Russell, 1995)

et al. 2002). The location of the magnetopause is determined by the equilibrium between the magnetic and dynamic pressure of the solar wind with the magnetic pressure exerted by the magnetosphere. This balance keeps the dayside magnetosphere confined at about 10 R_E from Earth. However, the dayside magnetosphere is continuously contracting and expanding due to sudden changes in the solar wind dynamic pressure and IMF orientation. Meanwhile, in the nightside the magnetosphere is stretched out hundreds of Earth radii in anti-sunward direction, giving origin to the magnetotail. The magnetotail has been observed more than 200 R_E away from Earth *(Slavin et al., 1983)*.

Different regions can be identified in the Earth's magnetosphere. The first region is the bow shock *(Fairfield 1971)*. The magnetosphere acts as an obstacle to the solar wind and induces a bow shock in front of it. In this region the solar wind slows down, it is scattered and reflected. The region between the bow shock and the magnetosphere is called the magnetosheath and is composed of heated solar wind that flows around the magnetosphere (*Longmore et al., 2005*). The magnetosphere is populated by ion and electron of solar wind or planetary origin that circulate under the effect of variable magnetic fields. The magnetic field components and the currents combine with the different external conditions of the IMF and the solar wind making the

magnetosphere a highly dynamic environment. The inner region of the magnetosphere is known as the plasmasphere. The plasmasphere has a toroidal shape and is formed by closed magnetic field lines. The plasma inside the plasmasphere is composed of electrons and ions that are trapped by magnetic field lines and form a cold plasma (fews electronvolts) around the Earth up to 4 - 5 Earth radii, co-rotating with the Earth *(Lemaire and Gringauz, 1998)*. The plasmasphere is coupled to the ionosphere, the upper region (between 50 - 1000 km) of the atmosphere, which delimits its inner edge, while the outer edge of the plasmasphere is called plasmapause (*Carpenter, 1963*).
The magnetotail is the region on the nightside of the magnetosphere. It consists of two tail lobes, northern and southern, separated by the plasma sheet, and is constantly stretched by the flow of the solar wind. The tail lobes have a low plasma density while the plasma sheet is a region of hot high-density plasma. The plasma in this region can flow along the magnetic field lines from the nightside regions into the auroral region. The auroral zone is a ring around the northern and southern polar region where magnetospheric electrons and ions impact the upper atmosphere to produce visible airglows, the auroras *(Feldstein and Galperin, 1985)*. Close to the northern and southern poles of the Earth's dipole there are the cusp regions, where the solar wind can enter on the dayside of magnetopause along open magnetic field lines *(Sandahl, 2003)*.
In the Earth's magnetosphere, there are several plasma populations with different properties that build up and evolve. The charged particles in the magnetosphere are guided by magnetic and electric fields. The trajectory of ions and electrons is governed by the Lorentz force which makes the particles gyrate around magnetic field lines in helical orbits, moving also up and down along the field lines (Fig.4.2). The inner magnetosphere contains the Ring Current (RC) region, which forms in approximate toroid centered on the Earth. The RC consists of charged particles that longitudinally drift around Earth at distances between 3 and 8 R_E. The electrons drift eastward while the ions with energy of several tens of keV (mainly H^+, He^+, O^+ and N^+) drift westwards. These particles gyrate around and bounce along magnetic field lines and drift around the Earth in a timescale of hours.
During periods of intense solar activity, the strong variability of both the solar wind and the IMF can cause disturbances in the Earth's magnetosphere. When the IMF is southward, the Earth's magnetic field is anti-parallel to the IMF, as it is oriented from south to north at the dayside of the magnetopause. So, the Earth's field lines can spontaneously break and reconnect with those

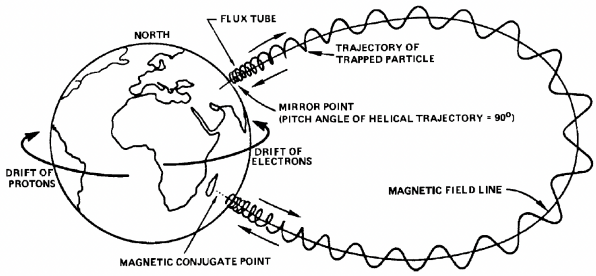

Figure 4.2: Planet's magnetic field dominates the magnetosphere and traps charged particles, which may be accelerated up to very high energies. Trapped charged particles gyrate about magnetic field lines, participate in drift motion, and form radiation belts

of the IMF. This process is called magnetic reconnection. The solar wind then drags the reconnected field lines from the dayside to the nightside, allowing the plasma to flow into the tail of the magnetosphere. During these solar events electric fields are induced inside the Earth accelerating particles towards the inner nightside magnetosphere. The particles begin to circulate around the Earth, inducing magnetic fields opposite those of the Earth. This creates a depression in the magnetic field. The sequence of all these events is called a geomagnetic storm and as solar activity increases, the storms become stronger.
The RC intensity is monitored by ground-based magnetometer stations as an indicator of geomagnetic activity. The effects of magnetic field depression is often interpreted as an enhancement of magnetospheric equatorial ring current. The storm-time disturbance index Dst *(Sugiura, 1964)* is designed to measure this phenomenon, evaluating the strength of magnetic storms.
The equatorial magnetic field variations on ground could provide global information. Nevertheless, detailed information related to the RC or other magnetospheric region, like shock front-side, cannot be easily derived from such indices. ENA detection could be the only way to give a global view of the dynamics of these populations.

4.2 Charge Exchange process

Charge exchange is a process that occurs when energetic ions interact with the atoms of the exosphere. In this process, schematically illustrated

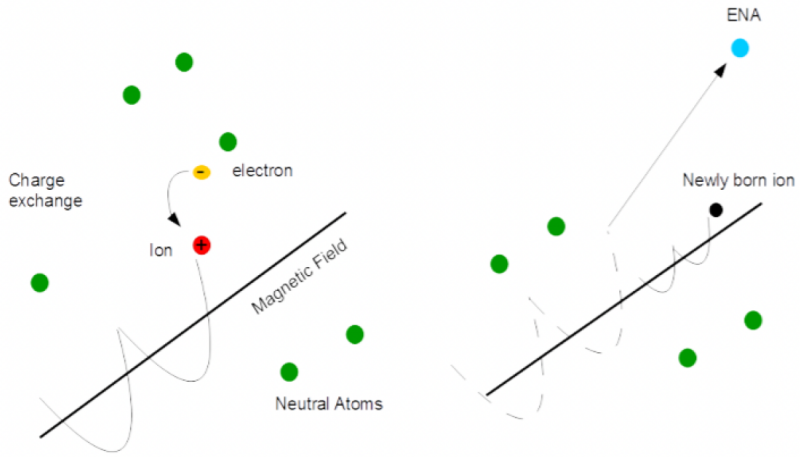

Figure 4.3: Charge exchange process: an ion along the magnetic field line (left) picks up an electron from a neutral atom and becomes an ENA (right). The ENA continues flying unaffected by the electric and magnetic fields (Futaana et al. 2011)

in figure 4.3, the energetic ion captures an electron from the cold neutral atom of the local exosphere. The result of this interaction is an Energetic Neutral Atom (ENA) and a thermal ion *(Hasted, 1964)*. In this process, a small amount of kinetic energy is exchanged between the neutral and the ion when the two species are of the same species or have similar ionization energy. For example, this happens when H geocorona interacts with protons or O^+ (photoionization energy $\sim$ 13 eV) producing a cold ion and an energetic neutral atom.

The newly created ENA has the same mass and approximately the same energy and the direction of the colliding energetic ion. The target is scattered at an approximately perpendicular angle with respect to the projectile path. Since it is no longer affected by magnetic or electric fields, ENAs can travel large distances through space with minimal disturbance, so that path can be considered straight lines, quite similar to the photon ones *(Orsini et al, 1998)*.

Investigations of environment dynamics can be achieved by the remote sensing technique, i.e the detection and monitoring of the physical characteristics of the environment by measuring reflected and emitted radiation at a distance. The main advantage of using global remote sensing, when compared to the direct ion detection, is that it is possible to have an instantaneous

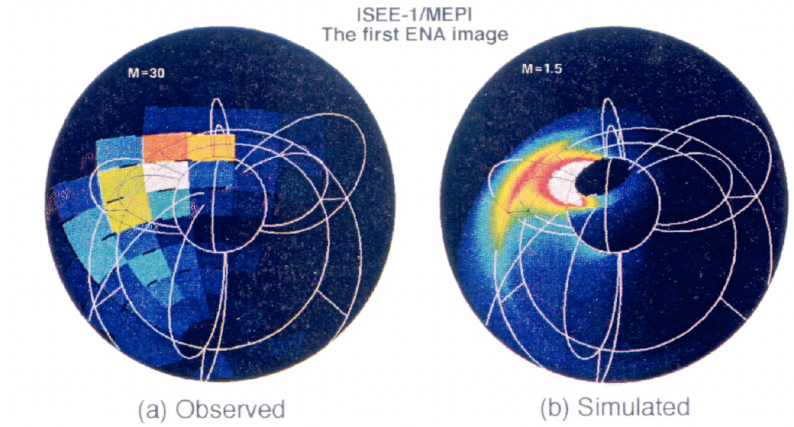

Figure 4.4: First ENA image was reconstructed from ISEE-1/MEPI data (Panel a). The circle shows Earth with examples of magnetic field lines for L = 3; Sun is to the right. Panel b reproduces the same image simulated using a ring current model (Roelof, 1987)

survey of the whole magnetosphere of a planet (*Gruntman, 1997; Wurz, 2000*). ENA imaging provides knowledge of the magnetospheric and heliospheric processes. Before the first ENA measurements, for example, most of the knowledge of plasma distributions in the magnetosphere came from in situ measurements, which could not provide the global information instantaneously, but only a statistical picture of it. Multi-spacecraft in-situ-measurements missions can in addition provide local space plasma parameters in three dimensions, allowing to derive gradients, curls and the divergence of these quantities *(Escoubet et al., 2015)*. Instead, the magnetospheric imaging mission are designed to provide a global view of the planet environment via ENA imaging. Therefore, in situ measurement missions and magnetospheric imaging missions are complementary. The locally measured parameters provide the "ground truth" and the local detailed ion distributions, whereas ENA images provide an instantaneous view of the magnetosphere and allow the local measurements with respect to the global context *(Vallat et al., 2004)*.

The presence of ENAs in the planet environment generated by the interaction of terrestrial ionospheric plasma with the local exospheric gas was discovered for the first time in 1950. *Meinel (1951)* detected a blue-shifted α-line during an intense auroral storm: the observations established that

protons precipitate into the upper atmosphere during the storm and must provide the primary energy source for the auroral emissions indicating that some precipitating H ions were being neutralized. However, it was not until 1987 that the first ENA image of a magnetic storm was constructed from measurements recorded with the ion detectors on board IMP 7/8 and ISEE spacecraft *(Roelof, 1987)* (Fig. 4.4). The satellites orbited out of the magnetospheric environment and detected some energetic particle flux coming from the Earth.
The potential of this technique to remotely study global plasma phenomena in space has attracted the interest both in the terrestrial and extraterrestrial space exploration missions. Missions such as NASA's IMAGE (Imager for Magnetopause-to-Aurora Global Exploration) mission *(Burch 2000)*, launched in 2000 and TWINS (Two Wide-Angle Imaging Neutral-Atom Spectrometers) *(McComas et al., 2009a)* , launched in 2006, are dedicated to ENA imaging of Earth's magnetosphere.
In addition, a dedicated ENA instrument was selected for the Cassini mission to study Saturn's magnetosphere, the INCA instrument *(Mitchell et al., 1993)*, and space missions such us Mars Express and Venus Express are dedicated to ENA imaging with ASPERA-3 and ASPERA-4 (*Barabash et al, 2004 and 2007)*).

4.3 Investigations of the Earth magnetosphere via ENA

The geocorona, which can be thought of as an extension of the upper atmosphere, overlaps with regions of the ring current and there is a possibility that energetic ions from the ring current may collide with a geocoronal hydrogen or oxygen atom. This collision causes a charge exchange and ENAs are produced and emitted, being one of the major cause of exospheric loss *(Fok et al., 1991; Dandouras, 2021; Yamauchi et al., 2022 and references therein)*. Space missions devoted to the ENA detection from different magnetospheric regions have monitored the global dynamics and the spatial and temporal evolution of the plasma components providing an image of the magnetosphere.

The IMAGE mission has provided a full range of ENA observations of the Earth's magnetosphere and the first comprehensive global images of the plasma populations in the inner magnetosphere. It has three neutral atom imagers on board the spacecraft in a high altitude and high inclination orbit

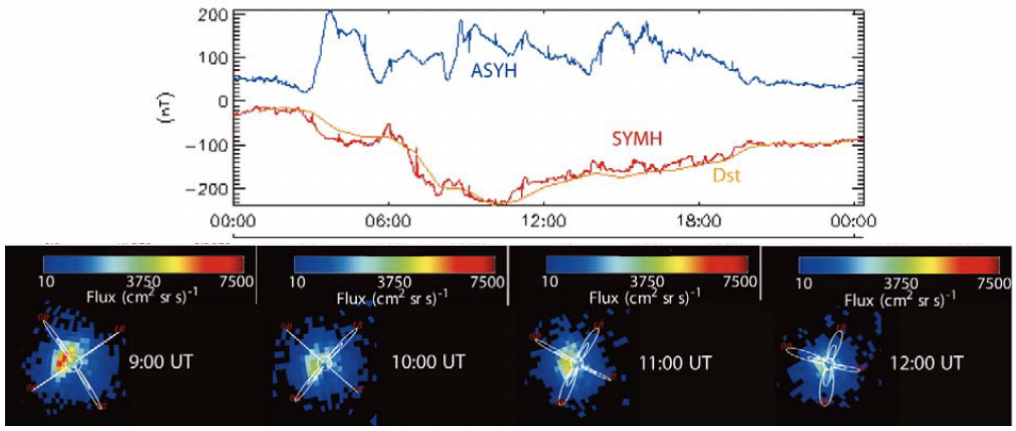

Figure 4.5: Ring current observations for the geomagnetic storm of 12 August 2000. The top panel shows Symmetric H-component (SYMH) (blue line) and Asymmetric H-component (ASYH) (red line) indices, that mainly represent longitudinal symmetric and asymmetric component of the RC, and Dst (orange line) for the entire day; the bottom panel shows the HENA data in term of ion flux ($[keV s\ sr\ cm^2)]^{-1}$) *(Fok et al., 2003)*

that continuously monitor the high-energy (HENA, 30–300 keV) *(Mitchell et al., 2000)* and medium-energy ions (MENA, 1–30 keV) *(Pollock et al., 2000)* of the ring current, and the low-energy plasmas (LENA, 10–300 eV) *(Moore et al., 2000)* in the ionospheric outflow. The space mission has shown how the ring current develops during magnetic storms and how ionospheric ions are injected into the ring current during substorms *(Burch, 2000)*. One of the results of the mission is shown in Figure 4.5. We can see the observed neutral atoms images during the geomagnetic storm of 12 August 2000: the top panel shows the geomagnetic indices for the storm, with a minimum around 10:00 UT, while the bottom panel shows a sequence of HENA images at different Universal Time (UT). The brightest image is clearly at 9:00 UT, before to the peak of the storm at approximately 10:00 UT. RC images obtained by the IMAGE satellite show the ion flux peak in the post midnight sector where ions are injected from the nightside and then drift westward toward dusk *(McIlwain, 1974)*. This study gives an global image of ring current effect taking advantage of a single instrument capabilities.

Another interesting process is the Low-Altitude Emission (LAE) ENAs, as the result of precipitating ions which undergo collisions and charge exchange with the oxygen exosphere. This signal was first observed by the Swedish

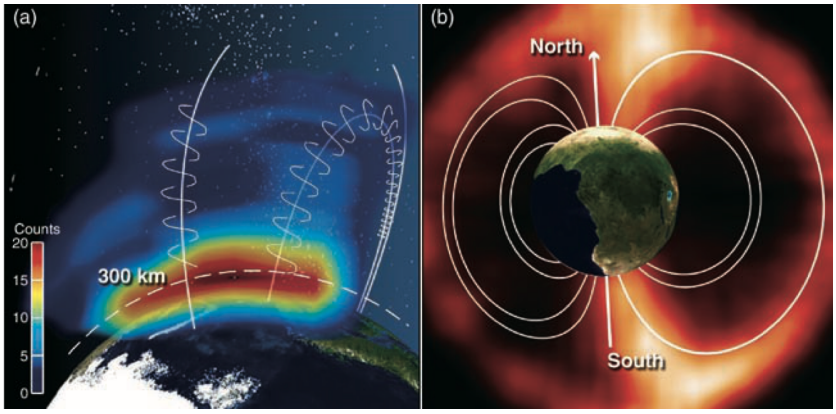

Figure 4.6: High-energy ENA images obtained by the ENA camera PIPPI (Prelude in Planetary Particle Imaging) onboard the microsatellite Astrid. Image of the interaction between the ring current and the upper atmosphere of the Earth (panel a); image obtained at a 1000 km altitude on the nightside looking down toward the Earth (panel b) (Brandt et al., 2005)

Astrid 1 spacecraft in a circular high-inclination orbit at an altitude of about 1000 km *(Barabash et al., 1997; Brandt et al., 1999)*. The Panel (a) of figure 4.6 shows an important detail of the ENA image where the maximum production of these particles is at an altitudine of 300 km, while an ENA image obtained from an equatorial, nightside point reveals the structure of the ring current in Panel (b).

LAEs have also been observed by the NASA TWINS mission *(McComas et al., 2009a)*, where two identical spacecraft were designed to image the magnetosphere simultaneously from two independent high-altitude, high-inclination platforms. The instruments were able to discriminate two different populations of ENAs, as shown in Figure 4.7. This is an example of ENA imaging during a megnetospheric storm on 22 July 2009 and shows emissions from the Ring Current (white line) coming from trapped ions in the inner magnetosphere, and LAEs (red line) as a result of precipitating ions which undergo charge exchange process with the oxygen exosphere. As the storm evolves, the intensity of the different emissions suggests that the LAEs have peaked before the RC. As the LAEs are produced where the geocorona is denser, the ENAs are produced more efficiently than the RC emissions, providing earlier indications. These observations could be important for space weather applications of ENA imaging, where early detection and measure-

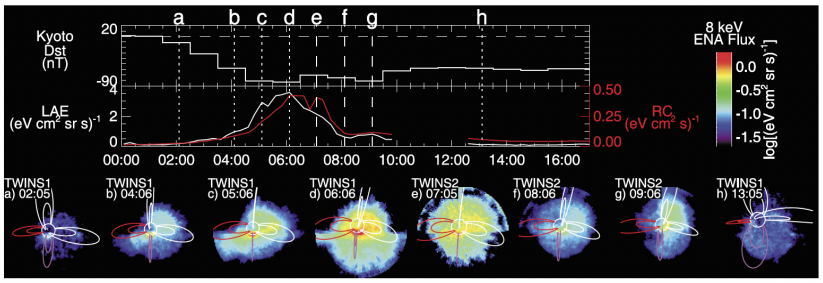

Figure 4.7: ENA emissions from storm in data 22 July 2009. From top to bottom panels: index Dst; the low-altitude (LAE) (white line) and Ring Current emissions (red line); times of the TWINS 1 and 2 images (Valek et al., 2010)

ment could allow a space storm tracking.

An additional signal comes from the compression of the magnetopause. This emission is pronounced during periods of high solar wind pressure, when the magnetopause has been pushed inward to a high geocorona density and thus the charge exchange between the two is intense *(Moore et al., 2000 and 2001)*. These particles are not involved in the energisation process and have low energies in the range between 10 eV to 1 keV. The low-energy neutral atom imagers, such as the LENA instrument on board IMAGE, are dedicated to observing neutral atoms produced by the charge exchange of magnetosheath ions with the hydrogen geocorona.

In order to have a global view of the solar wind-magnetosphere-exosphere interaction, *Connor et al. (2021)* reproduced modelled images of the Earth's environment that might be observed by a virtual spacecraft. They provide a polar view of the Earth's magnetosphere-ionosphere system: in figure 4.8, from top to bottom are dayside low-ENA images, nightside high-ENA images and auroral global images. The fist ENA signals reveal location of the bow shock and magnetopause; we can see how the maximum dayside signals move Earthward during the storm, revealing the distribution of dayside outer exosphere densities and their response to the event. In the middle panel, the fast-sunward plasma flows occur in the magnetotail, filling the inner magnetosphere with energetic particles as a result of nightside reconnection showing a distinct signal emission in this region. The polar view of the auroral region shows both dayside and nightside auroral brightening, revealing the connection between the magnetosphere and the ionosphere.

This work demonstrates the ability of the ENA imaging technique to provide

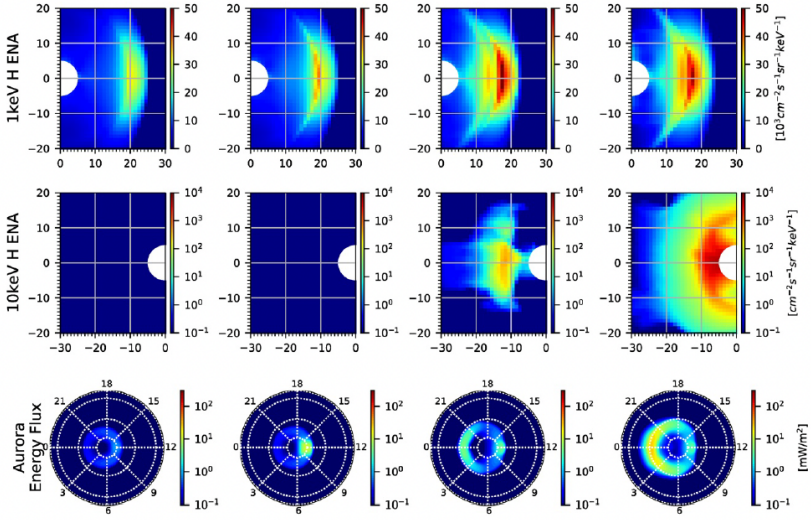

Figure 4.8: Ena emission polar-view images obtained from a virtual spacecraft: from top to bottom, there are dayside low-ENA images, nightside high-ENA images and auroral global images. The X and Y axes in the 1^{st}–2^{nd} rows are X_{gse} and Y_{gse} in R_e; the X and Y axes in the 3^{rd} rows are elevation and azimuth angles in degree with white dotted lines of magnetic local time (MLT) and magnetic latitude (MLAT) (Connor et. al 2021)

a complete picture of the solar wind energy flow from the bow shock through the magnetosphere and into the ionosphere. Presently, this technique has been used mainly from dedicated high altitude polar orbiting spacecraft, which do not allow a continuous and systematic monitoring, and a discrimination of the particle latitude distribution. The project Space WEAther Ena Radiation Sensors (SWEATERS) (riferimento appendice) aims at realising an innovative ENA sensor for Space Weather and plasma monitoring applications, based on gas detector technology. The space mission will include an ENA sensor in a Low Earth Orbit (LEO), which will allow to distinguish the dynamics of the magnetopause, the cusp and the RC in an innovative way.

CHAPTER 5

Modelling of Earth's environment

A model has been constructed to simulate the ENA generation in Earth's environment. This generation is generally due to magnetospheric plasma of different populations, including shock solar wind at the magnetopause but also ring current ions, which undergo charge exchange collisions with geocoronal neutral atoms. The ENA fluxes are the signature of the ion fluxes, weighted by the geocoronal density, and can be estimated as function of the ion energy and species and of the density and composition of the neutral gas, by integration along the line of sight of the instrument. The simulations reproduce the expected ENA signals for a specific LEO spacecraft configuration and determine the possible instrument requirements.

5.1 ENA signal simulations

In order to make an analysis of the expected ENA signals at a possible location of an instrument on board a LEO spacecraft, we built a model that simulates the generation of these particles in the Earth's environment, with particular emphasis on the RC and the front shock regions (bow shock, magnetopause). The relative importance of these signals is strictly related to the instantaneous configuration of the Earth's magnetosphere, *(Orsini et. al 2004, 2009)*, which can be reconstructed indirectly from real measurements of solar wind and magnetospheric parameters such as DST, Dynamic Pressure,

IMF and B-index.
The model is built in the following steps: a model for the RC in the equatorial plane is provided by *Milillo et al. (2001, 2003, 2004)*; in the following, we will use an expansions of the pitch angle, i.e. the angle between the particle velocity vector and the local magnetic field, to obtain the 3D distribution of the plasma; such an approximation requires a magnetic field model, which is provided by *Tsyganenko et al. (2015)* (T15). The supplementary information in the T15 package also provides real measurements of the solar wind and magnetospheric parameters, as well as the instantaneous shape of the bow-shock and the magnetopause. The exospheric model is taken from *Zoenchenn et al. (2015)* and the charge-exchange cross sections are given by *Lindsay et al. (2005)*. Finally, once the plasma and neutral populations have been modelled, the computation of the ENA signal is trivial and the ENA flux j_{ENA} will be obtained by line-of-sight integration

$$j_{ENA} = \int_{-\infty}^{0} j_{plasma}(E, l) N_n(l) \sigma dl \tag{5.1}$$

where, j_{plasma} is the differential flux of plasma, E is the energy, N_n and σ are the density of the neutral atoms and the cross section for the charge-exchange process, respectively; l is the distance along the direction of flight of the ENAs and the integral is taken from the spacecraft position back in time along the trajectory of the ENA.
In the following paragraphs, we describe the details of the model steps and show a feasibility study using the tool to analyse the 6 September, 2017 storm.

- **Ring current Model**
  The time-dependent version of the model by *Milillo et al. (2003, 2004)* gives the instantaneous estimated magnetospheric configuration for a given set of solar wind parameters that are used as inputs (i.e. Dynamic pressure and DST), and it is an evolution of the stationary empirical model of the equatorial proton fluxes by the same authors (*Milillo et al., 2001*).
  The model consists of several modules that reproduce the effects of different physical processes. The modules considered are those describing particle injection and diffusion in the equatorial magnetosphere are considered. The model provides an overall picture of the plasma distribution in the magnetosphere at the equatorial plane, thus allowing

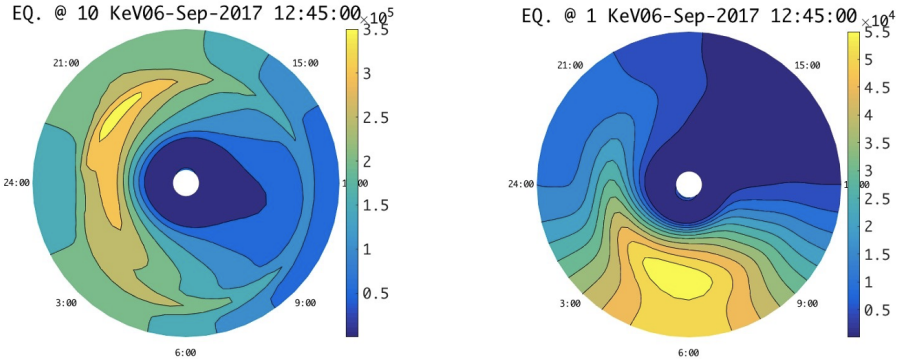

Figure 5.1: Equatorial proton flux distribution at 1 and 10 keV, units are cm-2 s-1 sr-1 keV-1

estimates of the main physical parameters, in our case the differential flux, as a function of particle energy.
As an example, we have applied the empirical model to a detailed analysis of the storm of 6 September 2017. In Figure 5.1 we show the resulting equatorial proton flux, when the DST and Pdyn parameters were 5.5 and 1.3 nPa, respectively.

From these values, to obtain the full 3D distribution of protons, we assume that the pitch-angle distribution at the equator has the so-called pancake shape. This distribution has a maximum flux at 90° pitch angle with a smooth decrease in flux towards the loss cone *(West et al., 1973)*. Given a point on the equator, we identify the magnetic field line that crosses this point by using the T15 model (section 5.1). The differential flux and the pitch-angle distribution on any other point of such line is obtained by assuming the conservation of the first adiabatic invariant:

$$\frac{K sin^2 \alpha}{B} = constant \tag{5.2}$$

where K is the kinetic energy, α is the pitch angle, B is the magnetic field intensity.

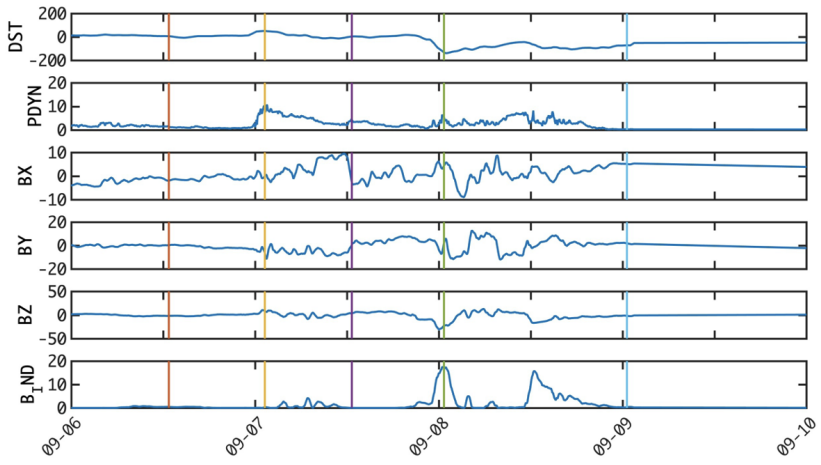

Figure 5.2: Magnetic field parameters during a geomagnetic storm (Sept. 2017).

- **Magnetic field model**

  The magnetic field model is provided by the T15 package from *Tsyganenko et al. (2015)*. The model of the Earth's magnetosphere is based on a large set of satellite data taken in the magnetosphere and in the solar wind during the period 1995 –2013, covering the distance range up to $\sim 60\ R_E$. The essence of the empirical magnetospheric modelling is to extract as much information as possible from spacecraft data about the configuration and time variation of the global magnetic field.
  Not only it is possible to reconstruct the magnetic field configuration for any possible set of parameters such as DST, Dynamic pressure, IMF and B index, but it is also possible to obtain time series of real data for these parameters in the past. As an example, we model the storm of September 2017 and we plot in Figure 5.2 the geomagnetic indices DST, Dynamic Pressure and IMF and B-index. The model also gives the shape of the magnetopause at any given time, as shown in Figure 5.3.

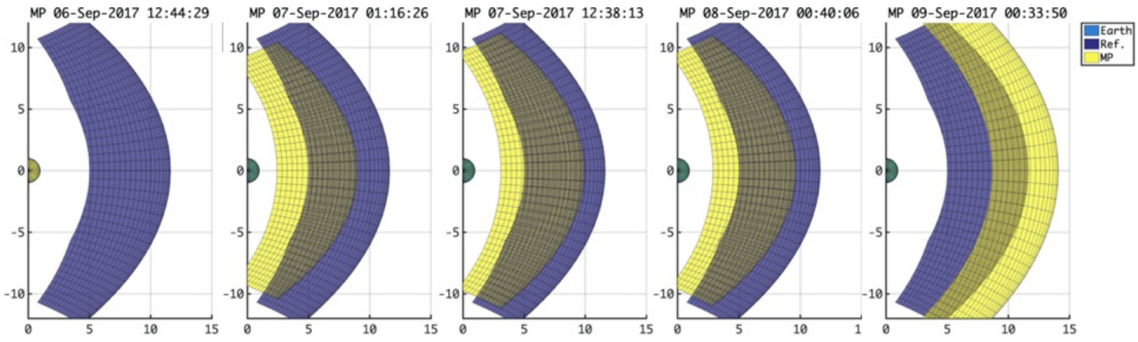

Figure 5.3: Position and shape of the magnetopause during the September 2017 storm

- **Exospheric model**
  The model for the exospheric densities is given by *Zoennchen et al. (2010; 2015)*, based on data measured by the Lyman-α detectors on board of the TWINS satellites. Neutral H atoms, as the main component of the terrestrial exosphere, produce the geocoronal Lyman-α glow by resonant scattering of solar Lyman-α radiation. The brightness of geocoronal Lyman-α column is proportional to the corresponding neutral H column density along a line of sight. The LADs detectors onboard the two TWINS satellites *(McComas et al., 2009)* have provided nearly continuous Lyman-α observations of the exosphere. These observations provide an important database for determining the 3-D density structure of the exosphere under different solar activities.
  In Figure 5.4 we show the modelled exospheric density profile as a function of distance from the Earth at the equator, (L-shell in Earth radii), showing how the trend decreases with increasing altitude.

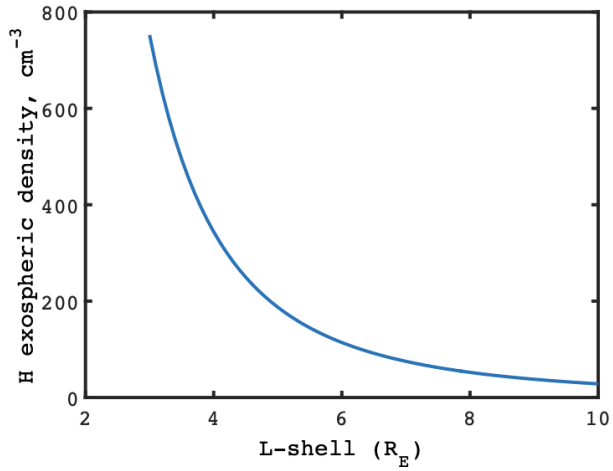

Figure 5.4: Exospheric density profile (Zoennchen et al., 2010)

5.2 Simulation results

We performed a simulation of the low altitude ENA emissions by using the models described in section 5.1. The goal is to simulate the ENA signal for an instrument on board a LEO orbiting spacecraft and to demonstrate the instrument feasibility to reach the scientific requirement.
A spacecraft in LEO orbit will be able to observe the evolution process of ENA sources, in addition to determining a global distribution pattern of the signals. A schematic view of the LEO orbit is shown in the figure 5.5. The satellite altitude of $\sim$ 500 km can be considered as a lower limit for the ENA detection, since at lower altitudes ENAs start to react with the atmospheric gas and are partly absorbed and partly scattered and can undergo multiple charge exchange interactions, changing from ion to neutral and vice-versa, due to the contiguously decreasing mean free path.
With a model of plasma distribution, of hydrogen exosphere and with the appropriate charge exchange cross section, we estimate the ENA flux that flows from such front shock region towards the Earth. The signal is due to those solar wind protons that are able to charge-exchange with the geocorona at high distances. The charge-exchange process here takes place mainly in the magnetosheath, were the solar wind has been heated, i.e. the solar wind kinetic energy is partially transformed in thermal energy, decreasing the plasma transport velocity and increasing its temperature. Furthermore, the plasma

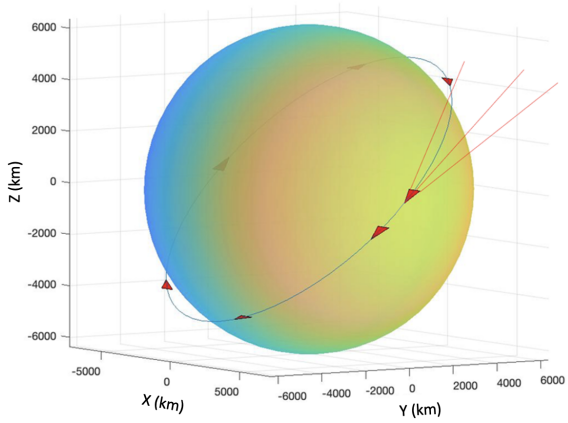

Figure 5.5: 3D view of LEO orbit, red triangles show a generic instrument on board the spacecraft where the red lines gives an idea about its field of view

bulk flow in the magnetosheath is more turbulent and deviated, following the local magnetopause contour. ENAs are then generated tangent to these parent ions deviated trajectories *(Longmore et al., 2005; Lavraud et al., 2013)*. To reflect into the simulations this aspect, we consider a temperature increase from an unperturbed solar wind condition to values greater than about a factor of 20 *(Spreiter et al., 1996)* to simulate the ENA outside the magnetopause. We implement a simplified model to demonstrate the feasibility of this study. In general, this signal is not very strong, because the exospheric density is too low at these distances. However, in the case of a particular intense solar wind event, the magnetopause can be compressed to lower distances, where the exospheric density is higher.
As an example, we have modelled the September 2017 storm and the compression of the magnetopause during this event. The figure 5.6 (panels (1)-(5)) reproduces the distribution of the ENA signal of the front-shock region that can be observed with a generic ENA sensor on a LEO spacecraft during the storm.

The present simulation results show an abrupt increase in the ENA signal during the geomagnetic storm, that peaks in in the night of 8 September (panel (4)) with the expected ENA flux in the range $10^2 - 10^4$ $(cm^2 ssr)^{-1}$, depending on the geomagnetic activity. These values are consistent with those previously simulated by *Connor et al. (2021)*.
As the simulated bow-shock signal is aspected on the dayside, the instrument must point towards the Sun direction to detect this signal. The Sun's light

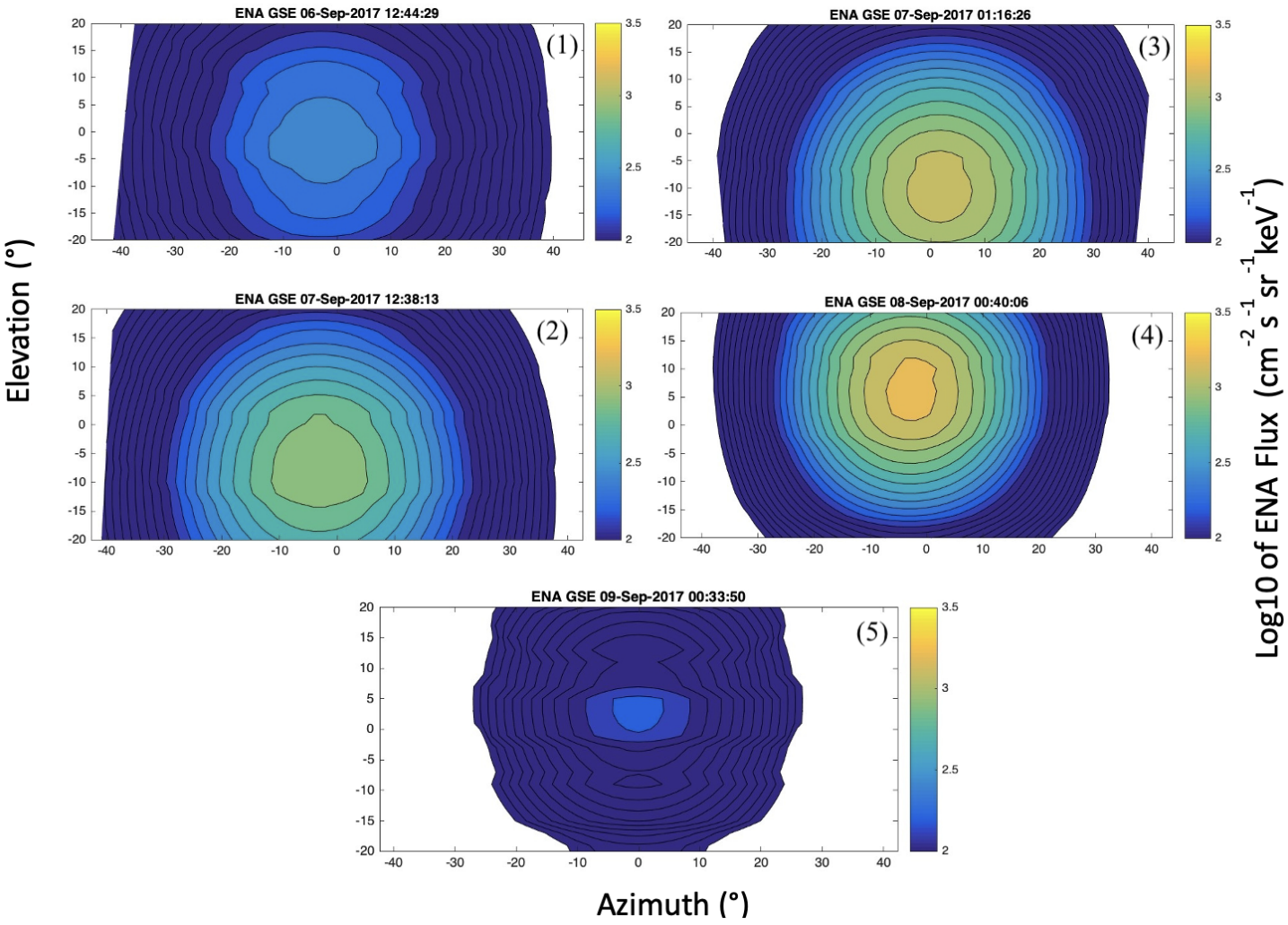

Figure 5.6: Model of ENAs signal in the front-shock region for a generic ENA sensor on board a LEO spacecraft in the case of the September 2017 storm. The X and Y axes are the elevation and azimuth angles in degrees, respectively, the GSE (Geocentric Solar Ecliptic) coordinate system, where the X-axis towards the Sun, the Y-axis is chosen to be in the ecliptic plane pointing towards dusk opposing planetary motion, and the Z-axis is perpendicular to the plane of the Earth's orbit around the Sun, positive to the north.

is the main source of UV photons, which can contribute to the background noise expected in the instrument. Therefore, the instrument should be able to shield and filter the UV signals.
It can be seen from simulations that a concept of an instrument that should/can detect and resolve ENAs with an angular resolution of about 10 degrees is plausible. This angular resolution makes it possible to distinguish between the ENA flow coming from the bow shock and that from the ring current. If there are an overlapping signals, the detector should discriminate the different energies of the particles to distinguish between the ENA populations. For example, ENA generated in the ring current region can be expected to have an energy between 10 - 100 keV, whereas ENA generated in the magnetopause will have a lower energy of about 0.5 - 5 keV. Tracking is also important to understand the energetic particle source of the storm. In conclusion the ENA detector must be able to provide the request information of energy and direction of particles in energy range of a few keV up to hundreds of keV.
A sensor with these characteristics, in a LEO orbit, can demonstrate the feasibility of this method of investigation. A possible configuration of a pair of sensors, with FoV perpendicular to each other, could investigate both sources towards the bowshock and towards the ring current. This way, spacecraft can realize continuous monitoring of low-altitude ENA emission sources and would be required to have full-time coverage.

CHAPTER 6

Present and future ENA detectors

The aim of this chapter is to present the analysis performed to test and evaluate a new type of detection for ENA signal able to accomplish the requested goal of a large energy range application and high spatial resolution in a unique sensor for LEO application presented in previous chapter. Several detector technologies have been considered and a MICROMEGAS (MICRO-MEsh Gaseous Structure) gas detetctor has been selected as candidate for a new instrument concept. As this is the first ENA application for a MICROMEGAS detector, it requires a study of a dedicated instrument design and it needs to be well investigated in terms of parameters and feasibility. In this chapter, a study on gas parameters optimization, such as the gas pressure and species, will be presented. A detailed activity of studies and instrument simulations are carried out at different beam energies both at atmospheric pressure and at low pressure to evaluate the instrument performance. Thanks to these studies, a prototype instrument is realized and tested to demonstrate the feasibility of ENA/Ion detection.

6.1 State of the art of ENA detectors

The interest in the development of ENA instruments for the ENA imaging requires the ability to detect these particles with good resolution in terms of mass, energy and direction. So, it is very important to select the appropriate detector in terms of requested scientific goals.
Different types of detectors are used for ENA particle detection: solid state detectors (SSD), microchannel plate (MCP) and channel electron multiplier (CEM). We briefly evaluate the techniques and capability of these detectors respect to ENA information returns. Solid-state semiconductor detectors can be used directly for detection of ENAs with energies higher than 10-20 keV. These detectors are capable of measuring the total energy of incoming particles and, combining this value with TOF (Time Of Flight) velocity measurement,it is possible to estimate the particle mass. An energetic particle penetrates the solid state detector and looses energy in Coloumb collisions with free and bound electrons *(Bertollini and Coche, 1968)*. The particle energy loss thus results in the creation of electron hole pairs. The charge carriers created by the energetic particle drift to the contacts of the opposite polarity. By measuring the total charge collected on a contact one can determine the total energy lost by a particle in the detector. For ENA imaging, SSDs have the big advantage that they can be immune to UV and EUV radiation, since the photon threshold is at 1.0 keV *(Gruntman, 1997)*, but low-energy ENAs (E $<$ 10 keV) cannot be directly detected by solid state detectors.
Another commonly used method for measuring neutral atoms at lower energies is to convert them into ions by passage through ultra-thin foils or reflection from a conversion surface and then analyze the ions energy using electrostatic analyzers. The detection of secondary electrons emitted from the interactions can be used in order to have a start signal for TOF measurements. The stop signal can be collected at the end of the electrostatic analyzer and velocity is evaluated by TOF .
So, the low energy particles can be registered by CEMs or MPCs detectors *(Rispoli et al., 2013)*. A CEM is a tube made of a slightly conducting glass *(Burrows et al.,1967)*. A high voltage applied between the tube ends creates an axial electric field inside the tube that allows the propagation and multiplication of an incoming electron. An MCP is a two-dimensional array of several millions identical miniature channel electron multipliers, closely packed parallel to each other *(Wiza, 1979)*.

This detectors have some limits: CEMs able to provide signals for ToF systems, but without energy and space resolution, instead MCPs are compact electron multipliers developed in a surface with high gain and high spatial resolution but without energy resolution.
New technologies have been developed to provide higher sensitivity, better angular resolution, and, most important, to extend the observable ENA energy range below several tens of keV, down to 1 keV. A challenge is to find a single detector able to provide the request information of energy, mass and direction for ENA investigation in the energy range from a few keV up to hundreds of keV. For this reason, a possible solution in gas detectors has been explored as a versatile technology for ENA detection and the feasibility to detect ENA at different energies is object of this work.

6.2 μ-megas detector

Since their development in '90s *(Giomataris et al., 1996)*, gas detectors have been used in several configurations, but only few space science studies and applications have been considered. For example, the MIMAC (MIcro-tpc MAtrix of Chambers) project was a multi-chamber detector with the goal to make a direct detection of non-baryonic Dark Matter and reconstruct the track of the recoil from the interaction between the particles and gaseous chamber *(Grignon et al., 2009)*. Another application of gas detector is aboard the IXPE (Imaging X-ray Polarimetry Explorer) mission, launched in December 2021. The space mission is dedicated to perform X-ray polarimetry on several astronomical sources thanks to a Gas pixel Detector (GPD) located at the focus of three X-ray telescopes.
This work presents a feasibility study of the application of gas detectors technology to ENA detection, focusing on MICROMEGAS (MICROMEGAS MICRO-MEsh GAseous Structure) detectors. These gas detectors have a two-stage parallel plate avalanche chambers able to detect the incoming particles by amplifying the charge generated by ionization processes in a gas volume. They consists of a gas cell, an anode, a catode and a thin metallic micro-mesh (Fig.6.1), that divides the gas volume in a drift and an amplification gap, respectively. In the drift region of several millimeters, between cathode and mesh, traversing charged particles or photons ionize the noble gas based mixture, primary electrons are generated and driven towards the micro-mesh by an electric field, typically ranging from 100 V/cm to 10

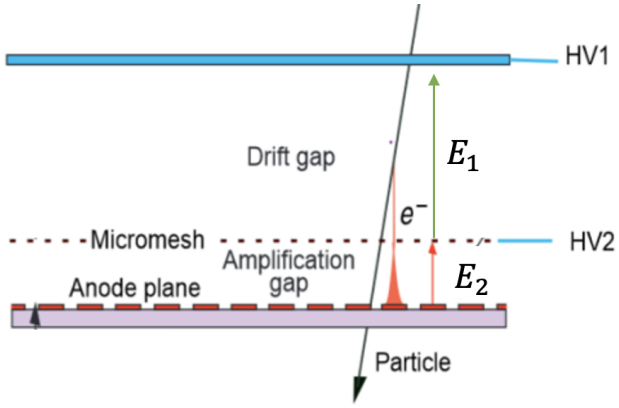

Figure 6.1: Standard MICROMEGAS scheme

kV/cm. The electrons reach the amplification region, the gap between the mesh and the anode with typical thickness of several tens of microns. Here an intense electric field of the order of several tens of kV/cm generates an electron avalanche. The charge movement can be measured on a readout structure at the anode, where the particle hit position as well as the timing can be precisely measured.
In these detectors, by applying potentials to the drift cathode, the mesh and the anode, electric fields are generated independently in the two regions, creating a two-stage parallel plate like setup. Furthermore, the particle track can be reconstructed to add significative information on direction of the incoming signal. These detectors have emerged as an outstanding gaseous detector due to their excellent counting rate, high spatial and time resolution, as well as its simplicity, low-cost and radiation resistance.

As this is the first ENA application for a gas detector, it needs to be well investigated in terms of parameter optimization. For our specific applications, the crucial parameters are the density (pressure) and the species (mixture) of gas inside the chamber, the drift fields and the mesh transparency and the entrance window of the detector. An evaluation of these parameters well be discussed in the next paragraph.

- **Pressure and gas mixture**

  The activity with MICROMEGAS detector is generally performed at atmospheric pressure. For our application, we want to study for the first time the detector performance assuming low pressure inside the

chamber. In fact, the pressure inside the cell is important in terms of track reconstruction of the particles. The mean free path of the ionization electrons under the electric field has to be detectable and for low energy particles it's on the order of several few of millimeter, so a low pressure is required to stretch the particle tracks.

MICROMEGAS detector prototype is constantly refilled with a mixture of gas and phenomenon of sparking should not be ignored. They can result from spontaneous breakdown due to mesh defects or induced by penetration of high-energy ionizing particles. The density of the primary ionization clouds in the drift gap resulting from gas recoil, can produce electrons and this is a limiting factor for sparking. While recoils deposit a small amount of total ionization, the ionization is deposited in a small volume of gas. If the charge density is high enough, a local electric field gradient can be produced, that can be large enough to induce a discharge. Reducing the gas pressure reduces the ionization density by extending the path, allowing the MICROMEGAS to achieve higher gains without sparking.

Stability against sparking in the beam is primarily a function of the quantity of quench gas in the mixture, as CO_2 or CH_4. The CO_2 has lower diffusion coefficient than CH_4 and a higher photo-absorption cross section. For example, the Ar-CO_2 mixture is stable against sparking and has a higher gain compared to the Ar-CH_4 mixture *(Snyder et al., 2017)*. Furthermore, the Ar-CO_2 mixture has great advantage over other gas mixtures because detectors operated in this mixture exhibit minimal aging effects compared to operation in carbon based gases like Isobutane.

It is possible to foresee the effect of low pressure and gas mixture on the particle path by running simulations with the SRIM (Stopping and Range of Ions in Matter) tool. The tool allows to study the effect of diffusion on the charge density by simulating a beam hitting a gas cell containing different mixtures at range pressure.

Gas detector has been simulated as a layer with different gas mixture observing the behavior of the particles inside the chamber. Figure 6.2 shows how long is the track of different ion beams (He and Ar) at 5 keV inside a gas chamber composed by different mixture as function of pressure. It is observed that as the gas pressure decreases, the track length increases and this behavior repeats for all the mixtures, so it is independent of the gas composition. The plot shows that in the

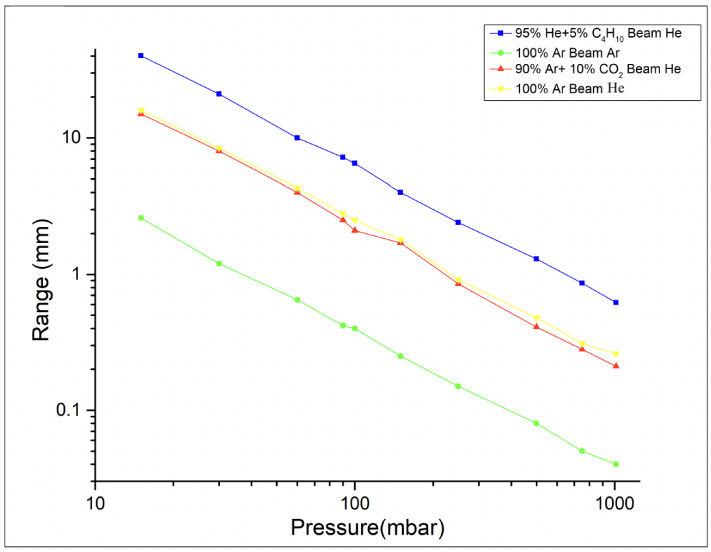

Figure 6.2: Track of different ion beams at 5 keV in a variety of gas mixtures as a function of the pressure

mixture composed of lighter gases, such as He (blue line), the path of the particles increases to 7 mm at 100 mbar, compared to the Ar-CO_2 mixture (red line) for which the track is 3 mm at the same pressure.

It's important to consider also the Ionization Quenching Factor (IQF), i.e. the fraction of energy released by a recoil in a medium through ionization compared with its total kinetic energy. This factor is important because it characterizes the percentage of particles energy that is involved for the ionization process, this value increases with increasing energy, but depends on beam, mixture and pressure of setup.
Considering the same gas mixtures, Figure 6.3 shows a plot of the IQF as function of the particles energy. At pressure 100 mbar, Ar-CO_2 mixture is better than the mixture composed of He, obtaining a greater percentage of the IQF for the energy range 1-5 keV. So, comparing the plots in the Figures 6.2 and 6.3 the conclusion is that in the mixture Ar-CO_2 the path of particles decreases but the ionization is more efficient.

- **Electric Field and Mesh Transparency**

  In the frame of parameter optimization the value of electric field is

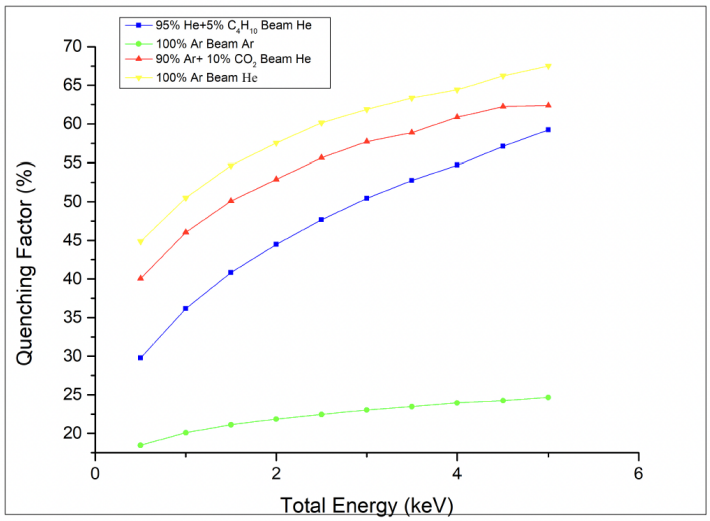

Figure 6.3: Ionization Quenching Factor (IQF) for different gas mixture at pressure 100 mbar as function of beam energy

crucial for the gas detector. In order to define the correct electrode voltage, we need to take into account the possible effect of mesh geometry and transparency.

Electrons from ionization processes move in the drift region between cathode and mesh and in the amplification region an avalanches are created, which can be detected by the readout electronics. Among the effects dependent on the drift field, the term Mesh Transparency is used as synonym for the transparency of the mesh for electrons.This describes the transmission of electrons into the high field region between mesh and anode.

Mesh Transparency strongly depends on the ratio $\zeta = \frac{E_{amp}}{E_{drift}}$ between electric fields in the drift and amplification region *(Geomataris et al., 1996)*.

When the ratio ζ is small, the field lines reach the mesh and in this case there is a low transparency. However, for hight values of ζ, the field lines of the drift region pass through the mesh in the gain region and reach the anode directly, allowing 100 % transparency.

This means that an increase in the drift field leads to a reduction in the detectable charge, i.e. the transparency of the mesh decreases as the drift field increases. This trend is due to the increase in the field lines

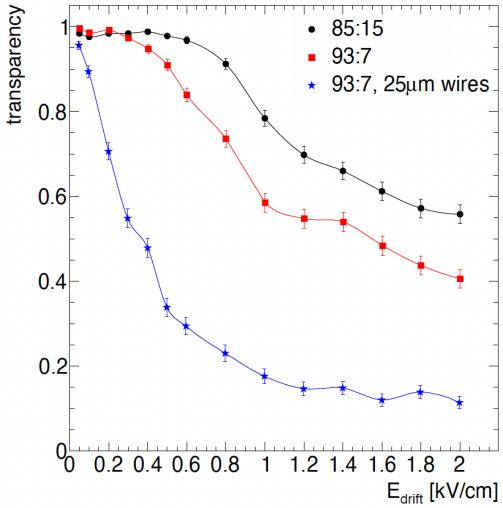

Figure 6.4: Electronic transparency of a mesh with a diameter of 18 µm (red line) and a diameter of 25 µm (blue line) as a function of the electric drift field for different percentages of Ar and CO_2 mixture at 20° C and 1013 mbar (Bortfeldt, 2014)

as the drift field increases, so that electrons following the field are lost on the mesh rather than entering the amplification region. It is also due to the transverse diffusion of electrons that do not strictly follow the field lines. This means that greater transverse diffusion increases the opacity of the mesh.

The Figure 6.4 shows the trend of the electronic transparency of the mesh for different mixtures of Ar and CO_2 *(Bortfeldt, 2014)*. It can be observed that the transparency decreases with the increase of the drift field and the maximum electronic transparency of the mesh is obtained for small fields. This could indicate that the high voltage conditions, i.e. high drift fields, are not suitable for measurements. When the detector operates at high voltages, the opacity of the mesh increases and the signal decreases.

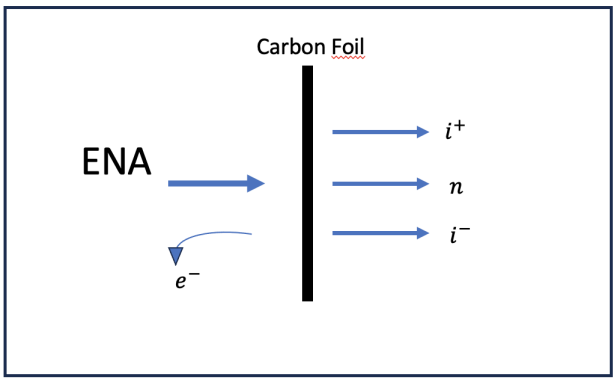

Figure 6.5: ENA- Carbon foil passage schematic

- **Entrance window**
  To date, MICROMEGAS detectors have been designed for HEP application or X-ray instruments, but the proposal to use these detectors for ENA detection requires a specific study of the entrance window.
  For ENA application, the instrument window has multiple tasks: it has to allow the entrance of the ENA in the requested energy range, 1-100 keV, it has to be able to ionize the ENA and it has to maintain the required pressure in the chamber. For this work, the best chosen candidate is an ultra-thin Carbon Foil (CF), used in several ENA space mission for the capability to efficiently ionize ENAs in the transmission (Fig. 6.5). The foils used in space are usually made of roughly a hundred atomic layers of carbon. The interaction of particles with CF also includes several adverse effects for the projectile that get out of the foil such as energy straggling and angular scattering, which usually act to reduce the sensitivity and overall performance of an instrument (*Allegrini et al, 2014; 2015*). The magnitude of these effects mainly varies with the incident angle, energy, mass of the incoming projectile and also with foil thickness. So, the aim is to use foils as thin as practically possible to minimize these effects. The nominal carbon foil thickness is typically quoted as an areal density ($\mu g\ cm^{-2}$) and values from 0.5 to 3 $\mu g\ cm^{-2}$ are typical for space plasma instruments.
  Also graphene is a challenge type of carbon foil that can be used: it is a promising solution to reduce energy straggling and angular scattering, but it needs maturity in terms of space application.

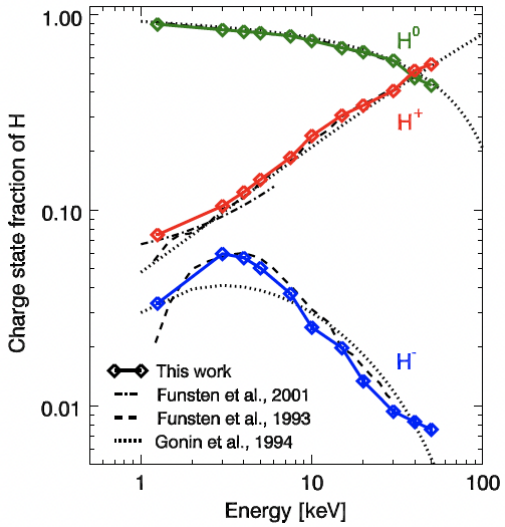

Figure 6.6: Charge state fractions of hydrogen after passing a carbon foil of nominal thickness of 0.5 $\mu g/cm^2$ (Allegrini et al., 2014)

In order to use these foils, it is important consider the charge exchange fraction, i.e. positive, neutral and negative charge states, for particles passage through the membrane. For example, Figure 6.6 shows the H charge fraction distribution as function of incident energy comparing the similar results for carbon and graphene foils *(Allegrini et al., 2014)*. As the projectile energy increases, the charge state distribution becomes positive as electrons are stripped off of the projectile, while there is a less significant fraction of negative ions.
In conclusion, it is important to consider a best compromise in terms of CF thickness, ionization efficiency and gas containment. The choice of the thickness has an impact on the scientific performance in terms of detectable particles energy, ionization efficiency, energy straggling and it is also important to take into account the gas containment respect chamber pressure *(Allegrini et al., 2014)*. This study will be one of the focal points of the ongoing work.

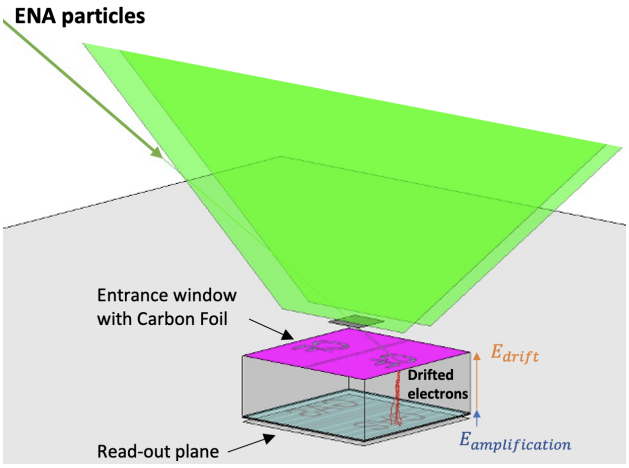

Figure 6.7: ENA instrument simulation shows 3 major sections: the entrance window, the gas cell and the readout system

6.3 Instrument Simulations

The study of the detector parameters and their optimization is implemented in a simulation activity with the aim of addressing the feasibility of the instrument. To reach this objective, it is developed a model to simulate the sensor and its performance for the ENA detection.
The PAOOLA code (Particle Analyzer Object Oriented LAnguage), that has been already successfully used for the simulations of the ELENA instrument aboard BepiColombo mission, was considered fruitful to model the gas detector. It is an Object-Oriented (OO) language written in MATLAB, which can however be compiled in C^{++} and then run free of license. The logic of the program is that every physical object is made to correspond to a class of programming objects, and every physical action that is possible with the material object corresponds a function in an OO language. For example, applying a particle object to a surface object will produce a scattered particle object, while if the particle object is applied to a gas cell object, will produce a cascade of electron objects.
The physical limits of this type of models are exclusively represented by the knowledge of the fundamental interactions between particles and between particles and solids, i.e. cross sections. For this reason, first of all, a database of cross sections and/or stopping powers was built. For this reason, the SRIM code was also used as an option to extract the cross sections.

The instrument concept is based on the required goal of ENA detection and consists of three specific sections: entrance window, gas cell, front-end/read-out electronics, which will acquire the charge signal. Figure 6.7 shows the instrument baseline modeled with the following objects: ENA enters in the instrument trough a dedicated section, i.e. the collimator-ion deflector (in green), devoted to define the field of view and also to rejected the background of charge particles with a deflector system. The gas-cell entrance window is an important element, where the ENAs have to be ionized passing through a thin membrane (pink surface) to convert the neutral particles into ions. The ionized ENAs enter into a first gas-cell stage (in gray), drift zone, where the particles lose energy by interaction with gas mixture and specific drift field allow to generate electrons, which continue down- wards. The amplification gap (the thin layer below in gray) is characterized by strong electric field, where the electrons are amplified and it is possible to generate a charge signal acquired by read-out system recording x-y position.
In the following sessions we will study the feasibility of the gas detector by simulating the main elements of the sensor, a specific entrance window and the gas chamber.

6.3.1 Entrance window section

For our specific gas detector applications, the best candidate for the detector window is an ultra-thin carbon foil due to its efficiency in ionizing ENA particles and also in maintaining the gas in the chamber.
We use the Matlab language to reproduce the CF object in PAOOLA code with the goal to establish a set of parameters to model the interactions of particles with CF. *Allegrini et al. (2014; 2015)* has provided ionization efficiency behaviour (Fig. 6.6) and derived a straight- forward empirical method to estimate the energy loss and straggling by measuring the scattering half width and applying semi-empirical relationships. The areal mass density Nd in $\mu g/cm^{-2}$, which is also an estimate of the foil thickness, is given by

$$Nd = 0.153 k_F \tag{6.1}$$

where N is the atomic density of the foil material, d is the thickness of the foil, and k_F is the foil constant as derived from its scattering distribution, for H and He is equal to 11.1 $\pm$ 1.5 and 29.1 $\pm$ 2.7, respectively. Energy loss as a function of incident energy for nominal foil thickness can be explain by

function

$$E_0 - E_1 = k\frac{Nd}{a_0 + a_1 E_0^{-0.4} + a_2 E_1^{0.25}} \tag{6.2}$$

where a_0, a_1, a_2 are the free parameters, a_0= -37.19, a_1 = 178.1, and a_2 = 9.236; N is the atomic density of the foil material, and d is the thickness of the foil, so Nd is the areal foil thickness in $\mu g/cm^2$; k, equal 19.9 for C atoms, is a unit conversion factor, E_0 is the incident beam energy, E_1 is the peak residual energy in keV.
The straggling Ω, which is the full width at half maximum of the energy distribution after the carbon foil, assuming a monoenergetic incident beam, is given by a similar expression:

$$\Omega = b_0 (kNd)^{b_1} E_0^{b_2} \tag{6.3}$$

where $b_0 = 8.3 \cdot 10^{-3}$, $b_1 = 0.70$, and $b_2 = 0.54$.
For the current work, we use the available data for ionization efficiency (Fig. 6.6) and these equations to evaluate the energy loss and straggling of particles passing through thin foils, in order to evaluate a concept instrument to be tested.

6.3.2 Gas chamber section

The gas chamber is the main element of the sensor: the impinging ENA can enter into the chamber, they are ionized in the transmission passing through the window and generate electrons in the gas; thanks to the specific voltage in the chamber, the generated electrons are drifted and collected in the read-out plane at the end of the chamber, allowing to have an efficient detection.
To achieve all the goal of this work, the studies of the chamber parameters carried out in section 6.2 showed that a low pressure condition is important in terms of particle trajectory reconstruction and the choice of a mixture $Ar - CO_2$ inside the chamber allows an efficient ionization of the particles.

Considering these studies, we use the PAOOLA code to simulate a gas chamber with dimensions of the order of 4 cm and an Ar-CO_2 mixture at a pressure of 50-100 mbar
The ionized ENAs enter into a first gas-cell stage, the drift gap of about 2 cm, where the particles lose energy by interaction with the gas mixture and

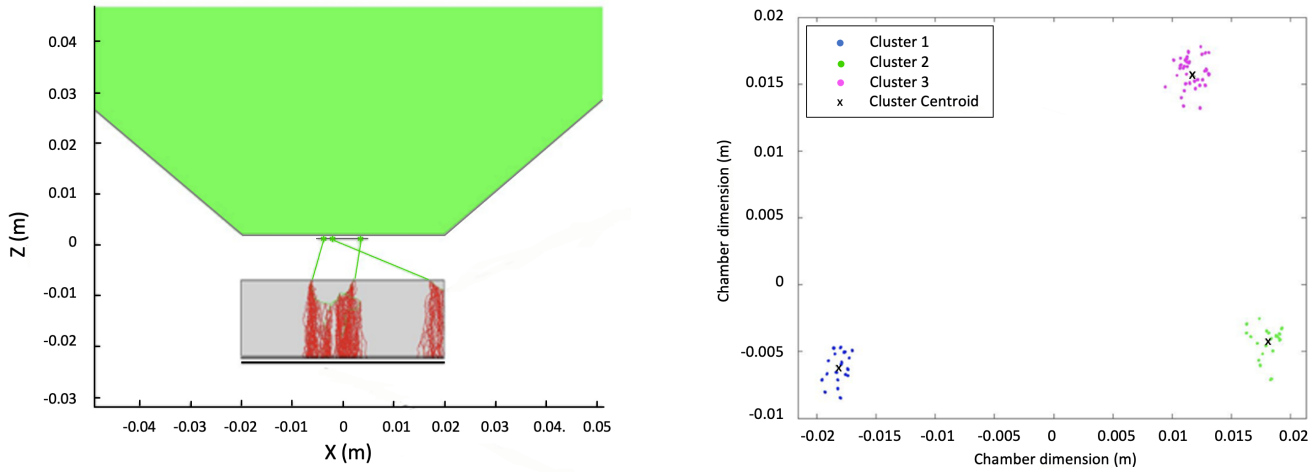

Figure 6.8: Simulations of ions 5 keV into the gas-cell: left illustration shows the ions track (green line) and the drift electrons that are brought down (red lines); right plot shows how the electron are distributed on the anode plane of the gas detector in this specific example

a specific drift field allows the generation of electrons that continue downwards. The amplification gap of about 192 μm is characterized by a strong electric field, there is a multiplication of electrons which can be of the order of 10^3.
The processing of the trajectory of the ions and electrons inside the chamber is carried out considering the cross sections: the trajectory is divided into steps and for each step it is considered the probability of having a collision and therefore of producing a secondary electron or of being deviated is considered (Fig. 6.8). The track reconstruction is important in order to have information about the direction of arrival ENA. These simulations are carried out to provide information on instrument gain and beam characteristics, such as the position and dimensions of the cascade at different pressures and electric fields. Based on these studies and simulations, we focus on a prototype that will be tested at the Ion/ENA facility.

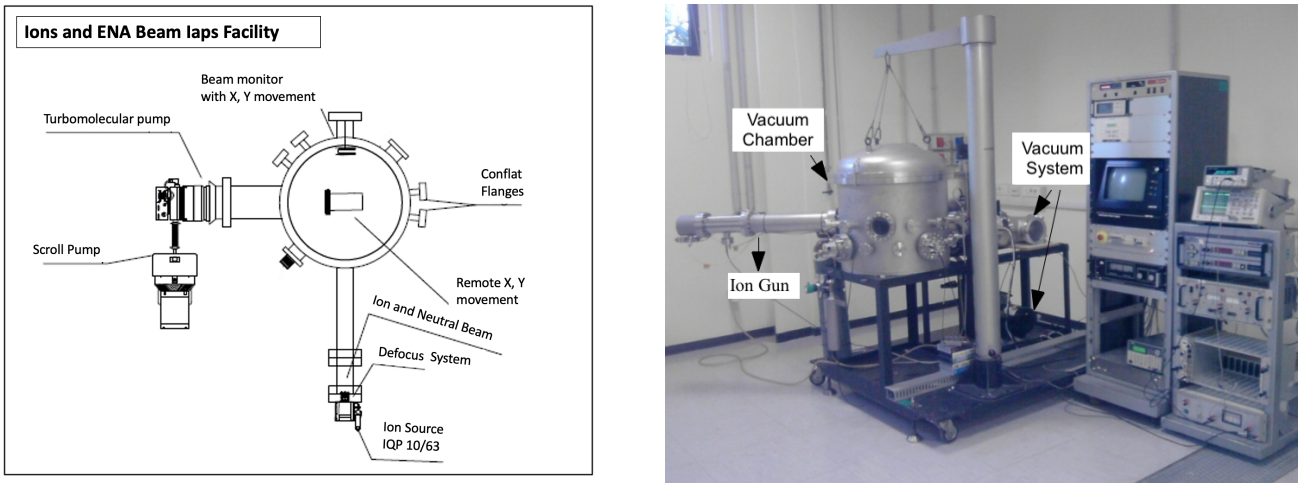

Figure 6.9: IAPS-INAF Ion and ENA Beam Facility: left panel is a scheme of the facility; right panel shows a picture of the ion beam and high vacuum chamber for instrument testing

6.4 Feasibility Test of μ-megas detector

6.4.1 Ion Beam Test facility at IAPS

At INAF/IAPS laboratory there is a facility of Ion and ENA beam (Fig. 6.9) that provide the opportunity to investigate the interaction of selectable ion/neutral beam with several samples and detectors *(De Angelis et al., 2016)*.
The vacuum system is composed by a scroll pump and a turbo-molecular pump that allow reaching pressure up to 10^{-7} mbar in the chamber. A system of controlled valves and gas inlets allow also to have differential pressure to generate the right condition for beam neutralization.
The beam line is generated by a Penning discharge type ion source (SPECS IQP 10/63), which allows the production of an accelerated Ion Helium (or Argon) beam, 8 mm wide, in the energy range of 0.1-5 keV. The Penning ion source operates on the principle of a self-sustained plasma discharge due to the ionization of an introduced gas, in this case He or Ar. The Penning-source establishes a Penning-discharge. The discharge between the cathode and the anode generates the plasma and the ions collisions on the cold cathode cause electrons emission. A magnetic field forces the electrons to follow a cycloidal

path. Because of the low pressure in the discharge chamber, the mean free path length is long enough to allow the electrons to gather the high energy required for efficient ionization of the gas. The Penning discharge starts easily and will run very stably for many hours.
In the ion beam line a charge exchange processes can take place thanks to a dedicated cell-tube volume, where interactions between ions and gas can have the right cross-section to generate ENA. So, Ion and ENA collimated beam runs the length of the gun and at the end it is slightly diverged by less than one degree. The energy of the beam can be easily controlled by setting the discharge bias on a dedicate power supply. Inside the testing vacuum chamber Ion or ENA beam can be selected thanks to electrostatic plates at the end of the ion gun.
The beam dimension and intensity can be regulated with a Einzel lens system and with pinholes of different diameters on the line. The Einzel lens system, located after beam generator, consists of three separated cylindrical electrodes *(Kalvas, 2014)*. On the central lens segment a bi-polar high voltage can be applied to generate both focusing and defocusing lens effect on the charged beam.
The cylindric vacuum chamber has a diameter of 60 cm and is equipped with several flanges that allows to introduce several devices useful for the test. Inside the vacuum chamber there are two vacuum motion system that can be controlled: a rotation (0°- 360°) and X (0-100 mm) and Y (0-50mm) translation stages that allow to put on the beam line all the subunits that have to be tested. We can also arrange in front of the beam or in the x-y motion system different beam monitor (such as MCP or Faraday Cup) to reconstruct beam profile.

6.4.2 μ-megas test setup

The feasibility tests of MICROMEGAS prototype have been performed at the Ion-ENA beam facility. Figure 6.10 shows our schematic test setup with the system of particle generation, the vacuum chamber and the detector mounted in front of the beam line. A gas system controls the gas mixture inside the chamber while the read-out and data acquisition system focus on reading the charge signal. The interface between the chamber and MICROMEGAS allows to impact on the detector with ions (through a calibrated pinhole) or with ENAs (passing through a Carbon Foil).
Taking into account the study and simulation described in previous para-

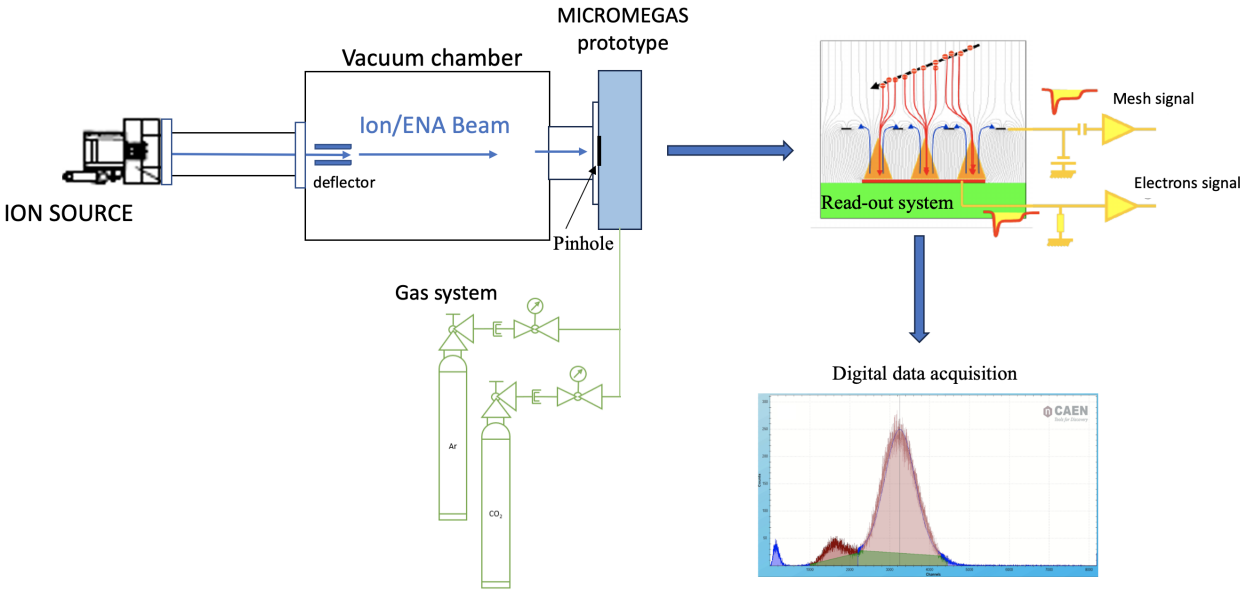

Figure 6.10: Scheme of the experiment: μ-megas test setup at the IAPS-INAF Ion Beam Facility

graphs, the following characteristics have been selected. The MICROMEGAS prototype (Fig.6.11) is composed by a gas chamber 16,6 x 16,6 cm^2 with a conversion gap of 2 cm. This drift distance between the cathode and the mesh is large enough to include the tracks of particles with energies up to 5 keV at atmospheric pressure and also at low pressure. The thin metallic mesh, supported by cylindrical pillars (25 μm), is above the anode plane, creating a narrow gap of 192 μm that defines the amplification region.
The detector is connected with an output flange of the vacuum chamber with a custom interface where a pin-hole is glued on the detector entrance to reduce the amount of gas flowing inside the chamber and maintain the low test pressure at 30, 50 and 100 mbar inside the gas cell. The dedicated gas system is able to regulate the flow of gases inside the cell with a mixture of 90 % Ar and 10 % CO_2 gases. The gas pressure and mixture inside the chamber, the ambient temperature and pressure, the vacuum level into in the detector are monitored to ensure the correct operation of the instrument.
When He beam in range of 1-5 keV is generated and ions interact with gas cell, electrons produced by these interactions are affected by the drift fields of drift and amplification zones and the signals are due to the electric charge

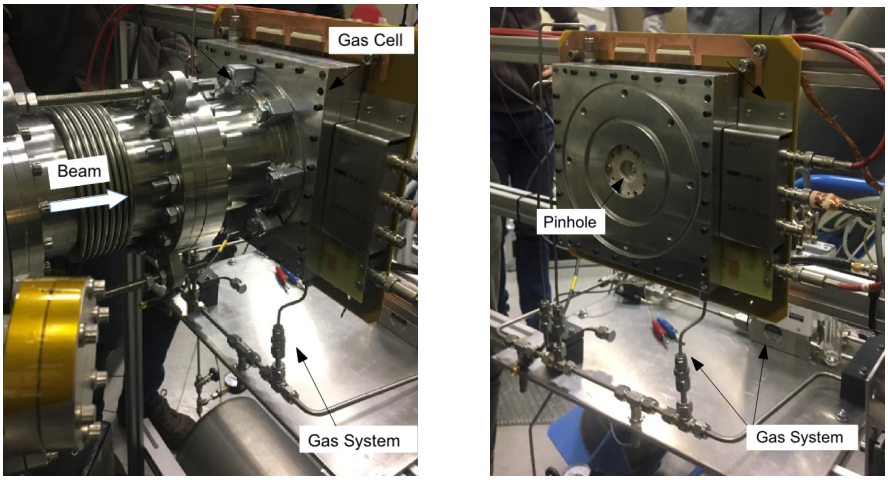

Figure 6.11: Details MICROMEGAS assembly sequence

collected on electrodes. These signals are amplified and read thanks to an electronic chain made up of front-end and read-out electronics and of the Data AcQuisition (DAQ) system. The readout circuit is a crucial element of the whole electronic chain for investigating the gas cell performance in terms of 3D track reconstruction, energy and angular resolution for ionizing particles in the 1-100 keV energy range. It typically converts and arranges the analog signal coming from the front-end into digital data read by the DAQ. The DAQ allows to reconstruct the X-Y position and the intensity of the signal, it collects the digital data from all readout devices and stores it into a suitable memory device. To better understand the energy spectra, a dedicated readout chain for analogic signal acquisition has been used to directly collect energy spectra from the mesh with custom charge-preamplifier and multi-channel analyser.
With this setup, we are able to demonstrate the ability of MICROMEGAS to detect particles in an energetic range and pressure condition never used before.

6.4.3 Preliminary result with ^{55}Fe source

Being the MICROMEGAS response well known for X-ray source in standard condition, testing the detector performance with the ^{55}Fe source is the first step to verify our set-up and capability to distinguish energies. This source emits X-Rays at energy that it is possible to reproduce with ion beam at the laboratory. ^{55}Fe decays producing X-rays at 5.89 and 6.49 keV, but in gaseous detectors the two energies tend to be indistinguishable due to the relatively large statistics-limited energy resolution. In most of the cases the whole photon's energy is absorbed and used to produce primary ionization electrons.
All tests with the prototype instrument are performed with the Ar/CO_2 - 93/7 % gas mixture, both at ambient pressure and at 100 mbar with a 148 MBq source, located at the detector entrance. In some cases the photon extracts an electron from Ar and the vacancy is filled by an outer electron, with the emission of another X-Ray photon of $\sim$ 3 keV. It is possible to observe another peak in the ^{55}Fe spectrum, called escape peak *(Giomataris et al., 1996)*.
We use an individual power supply for each electrode, cathode and anode, allowing the different fields to be independent. The signals are processed by the analogue readout and amplified by a dedicated charge sensitive preamplifier. Each signal is visualized on an oscilloscope to monitor the single impulse, sent to the CAEN multichannel analyzer to acquire and storage the data, and for a quick data analysis getting the value of peak positions and the energy resolution for each spectrum. For example, high resolution is for narrow peaks in the spectrum and can be estimated as the ratio between the Full Width Half Maximum (FWHM), i.e. the width of a curve at half of its maximum amplitude, and peak position.
Top plot of Figure 6.12 shows the ^{55}Fe spectrum obtained by setting the electric field at 25 V/cm and 30 kV/cm in the drift and amplification gap, respectively, at atmospheric pressure. It can be observed the single peak of ^{55}Fe at 5,89 keV and it is also possible to distinguish the escape peak of Ar at 2.9 keV. We perform a gaussian fit on the ^{55}Fe spectrum estimating the peak value and the deviation standard σ and a resolution of about 30 % on the principal ^{55}Fe peak.
At $P = 100$ mbar the working point changes in term of electric fields value in the gaps, we set the drift electric field at 50 V/cm, while we assume a value of 15 kV/cm in the amplification gap. The output signals from pre-amplifier

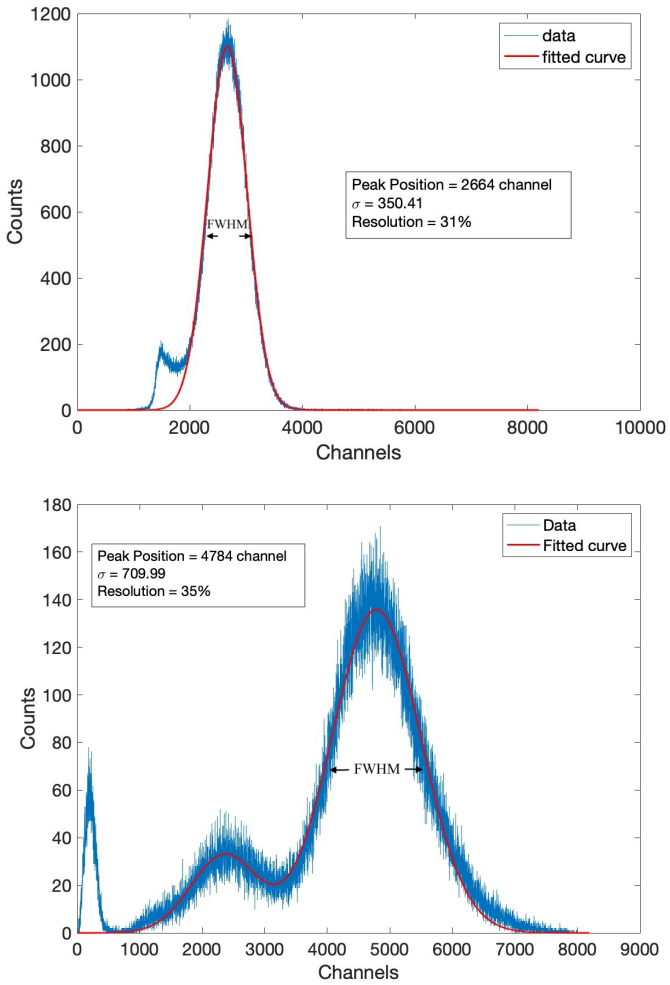

Figure 6.12: Fe^{55} Spectrum for a source 148 MBq at atmospheric pressure (top panel) and 100 mbar (bottom panel)

send to the CAEN show the spectrum in the bottom of figure 6.12. At low pressure, it is possible to better distinguish the ^{55}Fe peak and escape peak of Ar and this permit to perform the gaussian fit for both the curve. The spectrum appears more spread out than the measurements of atmospheric pressure and the resolution of ^{55}Fe peak gets little beat worse reaching a value of the order of 35%. This effect is connected with the low pressure conditions: low pressure means a low gas density in the chamber, therefore there is few interactions between ion particles and gas, few ionization process, and as consequence the electron signal will be smaller.
These preliminary results show the capability to distinguish energies, but also the importance to have a good compromise between pressure and electric field values for a detectable signal respect to particle energy.
Testing the MICROMEGAS with an X-ray source is the first step to explore the detector response before proceeding with the ion beam validation test in the similar energy range of 1- 5 keV.

6.4.4 He Beam Test

In the following set of tests, we examine the signal generated by He ion beam at selected energies between 0.5 and 5 keV.
The setup is the same as that used in the preliminary tests. Thanks the dedicated gas system, we obtain the correct mixture of Ar/CO_2 - 93/7 % inside the chamber at both atmospheric pressure and low pressure. Each incoming particle induces a variation in the mesh current, which is detected as a signal generated by the particles in the detector. The signals are amplified by a system of filters and amplifiers, as we have already described in section 6.4.3, and successively processed by the dedicated readout system. Each pulse is visualized on an oscilloscope and sent to CAEN data multichannel for the storage and quick analysis.
A complete set of measurements are performed with a He beam at 3 - 5 keV energy setting a low pressure of 100 - 50 - 30 mbar inside the chamber. For each run, we save information from CAEN about the peak position of the count distribution, the FWHM and the count rate. Figure 6.13 shows the pulse height distribution, plotting the peak position of the signal as a function of the He^+ beam energy. The instrument performance has a linear trend with the beam energy.

The following test provides the CF assembly in our setup with a sample of thickness about 0.5 μg cm^{-2} (*courtesy by F. Allegrini - SWRI (Southwest*

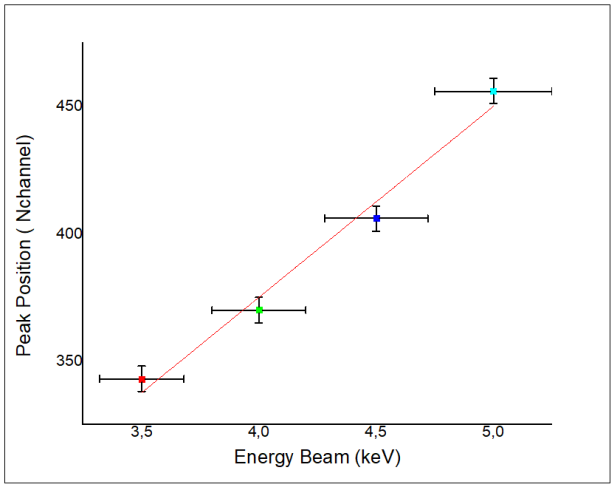

Figure 6.13: Peak position of the He^+ beam spectrum as a function of energy in the range 3-5 keV at pressure of 100 mbar

Research Institute)). The aim is to evaluate the capability of MICROMEGAS to detect ENA signal after CF passage. A preliminary test is performed with a He beam of 4 keV, the chamber at $P = 100$ mbar, the drift electric field set at 25 V/cm and a value of 15 kV/cm in the amplification gap. Figure 6.14 shows the beam spectrum comparing the test with and without the CF assembly in the setup at the same energy and pressure conditions. For now, we have verified the capability of our setup to detect ions and ENA particles. However, this is a first test and further investigations are needed, for example to study the characteristics of the neutral and charged beam after the CF and inside the chamber or to evaluate thin membranes with different thickness for different pressures maintenance.

It can be concluded that the results of the tests on our prototype confirm the capability of gas detector to measure ENA and provide important information about the detector parameters and its performance. Three different pressure values were investigated and the best results in terms of count rate, gain and dynamic range were obtained at $P = 100$ mbar. However, a lower pressure is more advisable to ensure a longer path of the particle inside the detector, which is essential to be able to reconstruct the track of the incident particle. The FWHM could be optimized and there are several possibilities for improvement (tuning readout chain, gas miscellaneous, detector parameters, design). However, this preliminary prototype detector

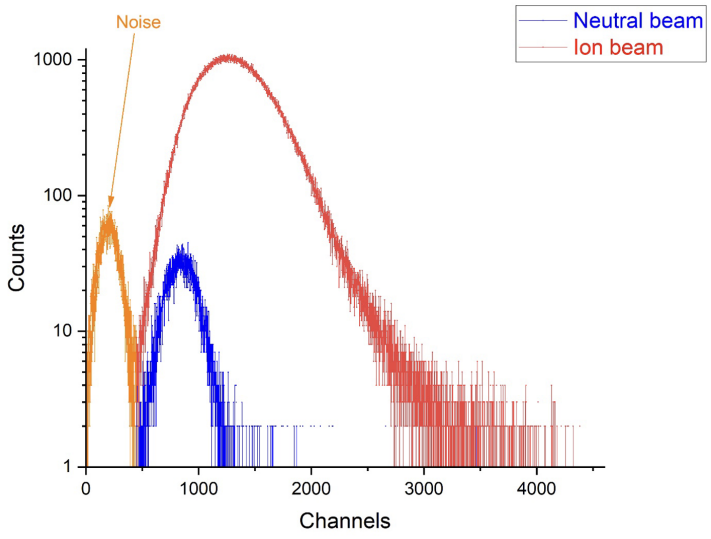

Figure 6.14: First comparison of MICROMEGAS detection of ion signal directly impacting on the detector (red line) and neutral beam passing through CF entrance (blue line)

can well discriminate different energies of the beam in the 1-5 keV range. Furthermore, the preliminary test with the carbon foil assembly shows the ability of the MICROMEGAS to detect the neutral atoms impacting on the CF entrance. Take into account that the system efficiency can improve for higher energy range, we can conclude that the gas detector is a good candidate to reach the goal of an instrument able to acquire ENA signal in a large energy range as for Earth study application and population discrimination as described on previous chapters.

Conclusion

This thesis presents a study of the Mercury and Earth exospheres. In detail, the work gives a comprehensive study of the source and loss processes of Mercury's exosphere introducing different models to study the planet environment. In addition, the thesis investigates the interactions between the plasma and Earth's exosphere using the ENA imaging technique and we present a new innovative sensor used for the first time for ENA applications. We use the 3D Monte Carlo model of the Hermean exosphere from *Mura et al. (2007)* to investigate Mercury's exosphere. We upgrade the model to better describe the MMIV process as source of Mercury's Ca. First of all, we verify that a uniform meteoroid precipitation cannot reproduce the dawn–dusk asymmetry observed in-situ in the Ca exosphere with the MESSENGER/MASCS sensor. The hypothesis of an asymmetric precipitation of micro-meteoroids that is higher in the dawn side (*Pokorny et al. (2018)*) is needed to explain the observed distribution. The derived CaO exospheric densities are up to $10^7\ m^{-3}$ maximizing on the dawn-side hemisphere, that is where the dust preferentially impacts the planet's surface. Following previous studies *(Killen et al 2016; Plainaki et al. 2017)*, we consider that the atomic Ca in Mercury's exosphere may be produced in a sequence of different processes: the exospheric energetic Ca component derives from the shock-induced non-equilibrium dissociative ionization and neutralization of Ca^+ during the vapor cloud expansion, while a low energy Ca component is generated later by the photo-dissociation of the CaO molecules released by micro-meteoroid impact vaporization.
We simulate the MMIV process comparing two different set of parameters. In the approximation of a vapor cloud quenching temperature ≤ 3750 K, we suppose that the CaO in the exosphere is produced by a subsequent pho-

tolysis processes of $Ca(OH)_2$, the dominant compound, then Ca(OH) and finally CaO, estimating a final $\tau_{Ca-bearing} \sim 270$ s. In a second case, we simulated the Ca exosphere assuming CaO as the predominant form of the initial Ca-bearing molecules ejecta at ≥ 3750 K with CaO lifetime equal $\tau_{CaO} \sim 10^4$ s, as considered in previous papers, like *Killen et al. (2016)* and *Plainaki et al. (2017)*. We simulated total Ca distribution in terms of atoms in the exosphere at different TAAs to reproduce the exospheric variability along the planet orbit and compared the results with the MESSENGER/MASCS observations including the contributions due to possible comet 2P/Encke (Figure 8). We lead to a conclusion that theoretical calculations agree better with observations at shorter photolysis lifetimes and lower quenching temperatures, which produce an higher excess energy of Ca atoms obtained during photolysis of Ca-bearing species. In that case we can emphasize the presence of two different Ca components where the energetic Ca component is more intense than the other at high altitudes, but in the post-dawn low altitudes we can see a substantial contribution of the low energy component to the global Ca exospheric content, as shown in Figures 3.11 and 3.12. The simulated Ca emission due to the possible comet contribution is underestimated compared to the observations at TAA equal to 25° and 150°. Since the MMIV contribution in refilling the exosphere is strongly dependent on the impact velocity, the total stream mass influx and also the arrival geometry of the meteoroids onto planetary surface, this study requires further investigation of the model parameters.

This study is a meant to be a step forward in the understanding of the MMIV process at Mercury; furthermore, the model is a strong and useful tool to the scientific community for the interpretation for data as well a for observational strategies of the ESA/JAXA BepiColombo mission, that will start its nominal mission phase in 2026. In particular, the resulting molecular distributions will be compared to the measurements of the MPO/SERENA-STROFIO mass spectrometer *(Orsini et al., 2010)* that will be the only instrument able to identify the molecular components, as CaO, and will permit to obtain simultaneous observations of different molecular and atomic components of the exosphere. These measurements coupled with the dust measurements by Mio/MDM instrument will allow for the first time a full investigation of the effect of MMIV at a planet.

The second part of this thesis gives an overview of the ENA imaging technique for the study of Earth's environment. In order to carry out an analysis of the expected ENA signals at a possible location of an instrument on board

a LEO spacecraft, a model has been constructed to simulate the ENA sources in the ring current and the front shock regions. From the simulation results, we derive possible instrument requirements: the instrument should be able to shield and filter the UV signals; a minimum angular accuracy of about 10 degrees is required to distinguish between the ENA flux coming from the bow shock and that coming from the ring current; in the case of overlapping signals, the ENA detector must be able to measure the different energies of the particles and reconstruct their direction in the energy range from a few keV up to hundreds of keV. With the aim of finding a single detector capable of providing the required information on the energy, mass and direction of ENA particles in a wide energy range, we study and evaluate the well-consolidated MICROMEGAS detector technologies. These detectors have been used with great success for High Energy Particles (HEP) instruments and for the first time it is proposed to use them for ENA applications. This innovative project needs to be well investigated in terms of parameters optimization. A detailed studies and instrument simulations are carried out with the aim to optimize the instrument performance at different beam energies, by varying the pressure of the gas cell. From our simulations, we conclude that the gas parameters, such as the pressure and gas mixture inside the chamber, can affect the path and the generation of the electron cascade: a low pressure is required to stretch the particle tracks; high drift fields inside the chamber increase the opacity of the mesh and the consequence could be the charged signal decreasing. Thanks to these studies, a prototype instrument is realized and tested in Ion-ENA beam facility at IAPS, demonstrating the capability of our setup to detect ions and ENA particles in the low energy range of 1-5 keV. We test the MICROMEGAS performance at different pressures, both at atmospheric pressure and at low pressure of 100 - 50 - 30 mbar inside the chamber, demonstrating that the detector can discriminate well between different energies of the beam.

A crucial point for ENA MICROMEGAS application is the detector entrance window, which first of all has to be able to ionize the ENA, it has to allow the entrance of the particles in the requested energy range 1-100 keV and it has to maintain the required pressure in the chamber. For our specific applications, the best candidate is an ultra-thin carbon foil. The preliminary test with the carbon foil assembly shows the ability of the MICROMEGAS to detect the neutral atoms, confirming that the gas detector could be a good solution for ENA applications. The successful demonstration of the feasibility of this innovative instrument for ENA/Ion detection makes it ex-

tremely attractive for a future space mission and open to new technological and scientific development.

APPENDIX A

Ground-based observations of Mercury's exosphere with THEMIS

An extended dataset of exospheric Na emission images has been collected by the THEMIS ground-based telescope from 2007 up to the present day. The analysis of these data has provided a comprehensive statistical study of the recurrent Na emission patterns and their possible relationship to IMF variability. Long campaigns of Na exospheric observations have been performed with remarkable results *(Leblanc et al.,2008, 2009, 2013; Leblanc andJohnson, 2010; Mangano et al.,2013)*.
THEMIS is a solar telescope *(López Ariste et al.,2000)* located on the Teide volcano in Tenerife, the Canary Islands. The telescope has a 0.9 m primary mirror and a focal length of 15.04 m. It can be used in daylight to image the Na exosphere above Mercury's disk for several hours a day. Like most ground-based observers, THEMIS uses high-resolution spectrographs to measure Mercury's spectrum. High resolution is necessary to remove backgrounds from the exospheric signal caused by sunlight reflected from the planet's surface and sunlight scattered by Earth's atmosphere.
In Mercury observations, the bright Na doublet emissions at 588.995 nm and 589.592 nm are referred to as D_2 and D_1, respectively. Two individual

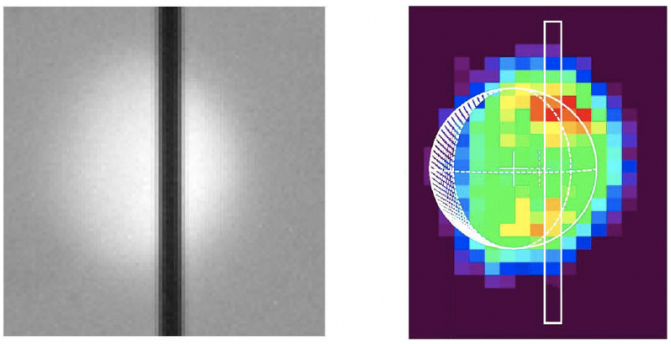

Figure A.1: Method of observation: (left) image of the spectrograph's slit on the planetary disk perpendicular to the planet's equator (dashed line); (right) reconstruction of the planetary disk image through a sequence of slit acquisitions plotted side by side

cameras on the THEMIS telescope are used to simultaneously measure the spectral regions around the D_2 and D_1 Na emission lines.
The approach to the observations is that the telescope images Mercury directly onto the entrance slit of the spectrograph (Fig. A.1), and the resulting spectra are analyzed to extract the intensities of the exosphere along the slit.

Mercury's north/south axis and Mercury's exosphere are scanned with the slit moving automatically between each position in a direction perpendicular to the slit. This method makes it possible to construct a two-dimensional image of the planet's exosphere.
An adaptive optics system is implemented on the telescope in order to provide the best possible correction in all atmospheric conditions, such us the correct tracking the seeing-affected image of the planetary disk. Spectra are dark corrected and flat fielded to remove camera and optical artefacts from the images. The former are images taken with a short exposure time, that are subtracted to reduce the amount of noise in the final images, while the flat field was obtained by observing the Sun using a special mode that avoids solar bright or dark spots.
Spectral calibration is performed by using the telluric lines on a sky spectrum taken during the observations. Resulting exospheric emission line (Fih. A.2) is fitted and integrated to derive the emission intensity.

From this analysis, it is possible to derive the Doppler shift and the spectral full width at half maximum (FWHM) of the emission line after correction for the effect of the point spread function of the telescope. Finally, a two-

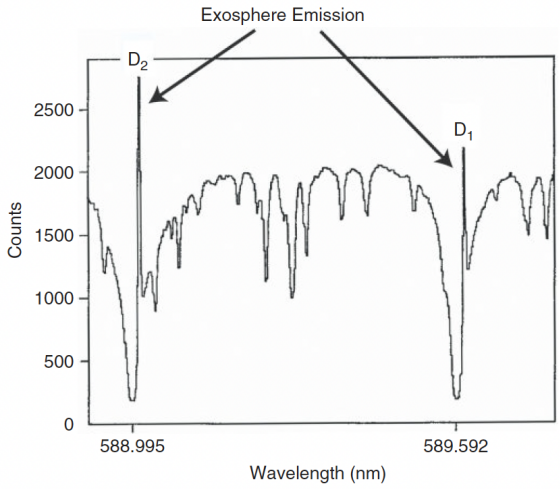

Figure A.2: Exospheric Na emission lines (D_2 and D_1) appear as narrow peaks above the solar reflected spectrum and on a side of the solar D lines

dimensional maps of the Na component of the exosphere are obtained (about 1 map/hour).

Thanks to the observations performed at THEMIS in recent years, the Na exosphere often shows a two-peak usually located at mid/high latitudes in both hemispheres of Mercury, which can often differ in intensity and extent (see Fig. 1.1 and details in the text).

Whitin this thesis, it is included the participation in the last campaign to monitor the evolution of Mercury's exosphere, which was carried out during the days of the BepiColombo's third flyby (19 June 2023). During this event a wide range of instruments on board the spacecraft provided high-resolution data on the planetary environment in terms of interplanetary and planetary magnetic fields, ions and electrons populations, their composition and their energies. This flyby, thanks to the favourable Earth-Sun-Mercury configuration, provided a unique opportunity to observe Mercury's exosphere as a whole from Earth-based telescopes and to obtain timely in-situ data from the spacecraft.

As done for the previous campaigns, the images will be analyzed with available tools. The in-situ measurements of the magnetic and plasma environment performed by BepiColombo during the flybys, which provide the quantitative environment parameters that produced the observed exosphere, i.e. its morphology and its dynamics, will be used to interpret the image profiles.

Scientific production

- Moroni, M., Mura, A., Milillo, A, Plainaki, C., Mangano, V., Alberti, T., Andre, N., Aronica, A., De Angelis, E., Del Moro, D., Kazakov, A., Massetti, S., Orsini, S., Rispoli, R. Sordini, R., 2023, "Micro-meteoroids impact vaporization as source for Ca and CaO exosphere along Mercury's orbit", Icarus, Vol. 401, https://doi.org/10.1016/j.icarus.2023.115616

- Mura, A., Plainaki, C., Milillo, A, Mangano, V., Alberti, T., Massetti, S., Orsini, S., Moroni, M, De Angelis, E., Rispoli, R. Sordini, R., 2023, "The yearly variability of the sodium exosphere of Mercury: A toy model", Icarus, Vol. 394, https://doi.org/10.1016/j.icarus.2023.115441

- Alberti, T., Sun, W., Varsani, A., Heyner, D., Orsini, S. Milillo, A, Slavin, J. A., Raines, J. M., Aronica, A., Auster, H. -U., Barabash, S., De Angelis, E., Dandouras, I., Jarvinen, R., Jeszenszky, H., Kallio, E., Kazakov, A., Laky, G., Livi, S., Mangano, V., Massetti, S., Moroni, M., Mura, A., Noschese, R., Plainaki, C., Plaschke, F., Richter, I., Rispoli, R., Sordini, R., Wurz, P, 2023, "High-energy particle enhancements in the solar wind upstream Mercury during the first BepiColombo flyby: SERENA/PICAM and MPO-MAG observations", A&A, Vol. 669, pg. 8, https://doi.org/10.1051/0004-6361/202244662

- Orsini, S., Milillo, A., Lichtenegger, H. et al., 2022, "Inner southern magnetosphere observation of Mercury via SERENA ion sensors in BepiColombo mission", 2022, Nat. Commun. 13, 7390, https://doi.org/10.1038/s41467-022-34988-x

Acknowledgements

This work has been supported by

- ASI-INAF agreement no. 2018-8-HH.O "Partecipazione scientifica alla missione BEPICOLOMBO SERENA Fase El" and Addendum no. 2018-8-HH.1-2022
- ASI-INAF agreement n. 2020-14-HH.0 "Partecipazione scientifica al progetto SWEATERS (Space WEAThER Ena Sensors)"

References

Allegrini, F., Ebert, R. W., Fuselier, S. A., Nicolaou, G., Bedworth, P., Sinton, S., & Trattner, K. J., 2014, Charge state of $\sim$ 1 to 50 keV ions after passing through graphene and ultrathin carbon foils, Optical Engineering, 53(2)

Allegrini, F., Bedworth, P., Ebert, R. W., Fuselier, S. A., Nicolaou, G., & Sinton, S., 2015, Energy loss and straggling of 1-50 keV H, He, C, N, and O ions passing through few layer graphene, Nuclear Instruments and Methods in Physics Research Section B: Beam Interactions with Materials and Atoms, 358, 223-228

Bailey, J., & Gruntman, M., 2011, Experimental study of exospheric hydrogen atom distributions by Lyman-alpha detectors on the TWINS mission, Journal of Geophysical Research, 116

Baliukin, I. I., Bertaux, J. L., Quémerais, E., Izmodenov, V. V., & Schmidt, W., 2019, SWAN/SOHO Lyman-α mapping: The hydrogen geocorona extends well beyond the Moon, Journal of Geophysical Research: Space Physics, 124(2), 861-885

Barabash, S. R. Lundin, H. Andersson, J. Gimholt, M. Holmstrom, O. Norberg, M. Yamauchi, K. Asamura, A. J. Coates, D. R. Linder, D. O. Kataria, C. C. Curtis, K. C. Hsieh, B. R. Sandel, A. Fedorov, A. Grigoriev, E. Budnik, M. Grande, M. Carter, D.H. Reading, H. Koskinen, E. Kallio, P. Riihela, T. Sales, J. Kozyra, N.Krupp, S. Livi, J. Woch, J. Luhmann, S. McKenna-Lawlor, S. Orsini, R. Cerulli-Irelli, M. Maggi, A. Morbidini, A.

Mura, A. Milillo, E. Roelof, D. Williams, J.-A. Sauvaud, J.-J. Thocaven, T. Moreau, D. Winningham, R. Frahm, J. Scherrer, J. Sharber, P. Wurz, P. Bochsler, 2004, ASPERA-3: Analyser of Space Plasmas and Energetic Ions for Mars Express, MARS EXPRESS: The Scientific Payload, edited by A. Wilson, ESA Publications Division, European Space Research & Technology Centre, SP-1240, 121-139

Barabash, S. R., J.-A. Sauvaud, H. Gunell, H. Andersson, A. Grigoriev, K. Brinkfeldt, M. Holmstrom, R. Lundin, M. Yamauchi, K. Asamura, W. Baumjohann, T.L. Zhang, A.J. Coates, D.R. Linder, D.O. Kataria, C.C. Curtis, K.C. Hsieh, B.R. Sandel, A. Fedorov, C. Mazelle, J.-J. Thocaven, M. Grande, Hannu E.J. Koskinen, E. Kallio, T. Sales, P. Riihela, J. Kozyra, N. Krupp, J. Woch, J. Luhmann, S. McKenna-Lawlor, S. Orsini, R. Cerullirelli, M. Mura, M. Milillo, M. Maggi, E. Roelof, P. Brandt, C.T. Russell, K. Szego, J.D. Winningham, R.A. Frahm, J. Scherrer, J.R. Sharber, P. Wurz, P. Bochsler, 2007, The Analyser of Space Plasmas and Energetic Atoms (ASPERA-4) for the Venus Express mission, Planetary and Space Science, Vol. 55, 1772-1792

Baumgardner, J., Wilson, J., & Mendillo, M., 2008, Imaging the sources and full extent of the sodium tail of the planet Mercury, Geophysical Research Letters, 35(3)

Berezhnoy, A.A, Mangano, V., Mura, A., Milillo, A., S. Orsini, S., 2011, Density distribution of metal-containing species in the exosphere of Mercury after meteoroids impacts, EPSC Abstracts, Vol. 6, EPSC-DPS2011-1793, 2011, EPSC-DPS Joint Meeting 2011

Berezhnoy, A. A. 2013, Chemistry of impact events on the Moon, Icarus, 226, 205–211

Berezhnoy, A.A, 2018, Chemistry of impact events on Mercury, Icarus 300, 210–222

Bertollini G. and Coche A., 1968, Semiconductor Detectors, Wiley, New York

Beth, A., Garnier, P., Toublanc, D., Dandouras, I., & Mazelle, C., 2016,

Theory for planetary exospheres: II. Radiation pressure effect on exospheric density profiles, Icarus, 266, 423-432

Bhardwaj, A. et al., 2005, Low energy neutral atom imaging on the Moon with the SARA Instrument aboard Chandrayaan-1 mission, J. Earth Sys. Sci., 114, 749–760

Bhardwaj, A., Dhanya, M. B., Sridharan, R., et al., 2010, The Sub-keV Atom Reflecting Analyzer (SARA) experiment aboard Chandrayaan-1 mission: instrument and observations, Advances in Geosciences: Volume 19: Planetary Science (PS), pp. 151-161

Bida, T.A., Killen, R.M., Morgan, T.H., 2000, Discovery of calcium in Mercury's atmosphere. Nature 404 (9), 159–161

Bortfeldt J., 2014, Development of Floating Strip Micromegas Detectors, PhD thesis, Ludwig-Maximilians-Universitat Munchen

Brandt, P. C. S., Barabash, S., Norberg, O., Lundin, R., Roelof, E. C., & Chase, C. J., 1999, Energetic neutral atom imaging at low altitudes from the Swedish microsatellite Astrid: Images and spectral analysis, Journal of Geophysical Research: Space Physics, 104(A2), 2367-2379

Brandt, P. C., Mitchell, D. G., Roelof, E. C., Krimigis, S. M., Paranicas, C. P., Mauk, B. H., et al., 2005, ENA imaging: Seeing the invisible, Johns Hopkins APL technical digest, 26(2), 143-155

Broadfoot, A. L., Shemansky, D.E., & Kumar, S., 1976, Mariner 10: Mercury atmosphere, Geophysical Research Letters, 3(10), 577–580

Burch, J. L., 2000, IMAGE mission overview, Space Science Reviews, 91(1-2), 1-14

Burger, M.H., Killen, R.M., McClintock, W.E., Vervack, R.J., Merkel, A.W., Sprague, A.L., Sarantos, M., 2012. Modeling MESSENGER observations of calcium in Mercury's exosphere. J. Geophys J. Res. 117

Burger, M.H., Killen, R.M., McClintock, W.E., et al., 2014. Seasonal

variations in Mercury's dayside calcium exosphere. Icarus 238, 51–58

Burlaga,L.F., 2001, Magnetic fields and plasmas in the inner heliosphere: Helios results, Planet. Space Sci. 49, 1619–1627

Burrows, Lieber and Zaviantse, 1967, Detection efficiency of a continuous channel electron multiplier for positive ions

Carpenter, D. L., Whistler evidence of a 'knee' in the magnetospheric ionization density profile, J. Geophys. Res., 68, 1675-1682, 1963

Carruthers, G. R., & Page, T., 1972, Apollo 16 far-ultraviolet camera/spectrograph: Earth observations, Science, 177(4051), 788-791

Carruthers, G. R., Page, T., & Meier, R. R., 1976, Apollo 16 Lyman alpha imagery of the hydrogen geocorona, Journal of Geophysical Research, 81(10), 1664-1672

Cassidy, T.A., Merkel, A.W., Burger, M.H., Sarantos, M., Killen, R.M., McClintock, W.E., Vervack, R.J., 2015, Mercury's seasonal sodium exosphere: MESSENGER orbital observations. Icarus 248, 547–559

Cassidy, T.A., McClintock, W.E., Killen, R.M., Sarantos, M., Merkel, A.W., Vervack, R.J., Burger, M.H., 2016, A cold pole enhancement in Mercury's sodium exosphere. Geophys. Res. Lett. 43, 11,121–11,128

Cassidy, T.A., Schmidt, C.A., Merkel, A.W., Jasinski, J.M., Burger, M.H., 2021, Detection of large exospheric enhancements at Mercury due to meteoroid impacts, Planet. Sci. 2, 175

Ceplecha, Z., 1992, Influx of interplanetary bodies onto Earth, Astron. Astrophys. 263(1–2), 361–366

Chamberlain, J. W., 1963, Planetary coronae and atmospheric evaporation. Planet. Space Sci. 11,901

Chapman, S. and Cowling, T.G., 1952, The Mathematical Theory of Non-Uniform Gases, Cambridge University Press

Chaufray, J. Y., Leblanc, F., Werner, A. I. E., Modolo, R., & Aizawa, S., 2022, Seasonal variations of Mg and Ca in the exosphere of Mercury, Icarus, 384, 115081

Cintala, 1992, Impact-induced thermal effects in the lunar and Mercurian regoliths, J. Geophys. Res. 97, 947–973

Christou, A. A., Asher, D. J., Ireland, N., Exosphere, H., & IWF, G., 2009, Possible meteoroid streams at Mercury. In 5th European Strategic Meteor Workshop-Meteoroid effects on the Hermean Exosphere: Observations, Models and Predictions for Future Missions, Graz, Austria, pp. 12-13

Christou, A. A., Killen, R. M., & Burger, M. H., 2015, The meteoroid stream of comet Encke at Mercury: Implications for MErcury Surface, Space ENvironment, GEochemistry, and Ranging observations of the exosphere, Geophysical Research Letters, 42(18), 7311-7318

Connor, H. K., Sibeck, D. G., Collier, M. R., Baliukin, I. I., Branduardi-Raymont, G., Brandt, P. C., .et al., 2021, Soft X-ray and ENA Imaging of the Earth's Dayside Magnetosphere, Journal of Geophysical Research: Space Physics, 126(3)

Dandouras, I., 2021, Ion outflow and escape in the Terrestrial Magnetosphere: Cluster Advances, J. Geophys. Res

De Angelis E. et al., 2016, Ion and ENA beam Laboratory at INAF/IAPS: a facility for plasma-environment simulation and space instrument development, Meeting of the Italian SOlar and HEliospheric community (SOHE)

De Simone, A.J., Orlando, T.M., 2014, Photodissociation of water and $O(^3PJ)$ formation on a lunar impact melt breccia, J. Geophys. Res., Planets 119, 894–904

De Simone, A.J., Orlando, T.M., 2015, H_2O and $O(^3PJ)$ photo-desorption from amorphous solid water deposited on a lunar mare basalt, Icarus 255, 44–50

Escoubet, C. P., Masson, A., Laakso, H., & Goldstein, M. L., 2015, Recent highlights from Cluster, the first 3-D magnetospheric mission. In Annales Geophysicae, Vol. 33, No. 10, pp. 1221-1235

Fairfield, D. H., 1971, Average and unusual locations of the Earth's magnetopause and bow shock, Journal of Geophysical Research, 76(28), 6700-6716

Feldstein YI, Galperin YI, 1985, The auroral luminosity structure in the high-latitude upper atmosphere: its dynamics and relationship to the large-scale structure of the Earth's magnetosphere, Rev Geophys 23:217–275

Fok, M.C., Kozyra, J.U., Nagy, A.F., Cravens, T.E., 1991, Lifetime of ring current particles due to coulomb collisions in the plasmasphere. J. Geophys. Res. 96, 7861–7867

Fok, M. C., Moore, T. E., Wilson, G. R., Perez, J. D., Zhang, X. X., Brandt, P. C. S., et al., 2003, Global ENA image simulations, Magnetospheric Imaging-The Image Prime Mission, 77-103

Fuselier, S. A., Burch, J. L., Lewis, W. S., & Reiff, P. H., 2000, Overview of the image science objectives and mission phases, Space Science Reviews, 91, 51-66

Futaana, Y., Chaufray, J.Y., Smith, H.T., Garnier, P., Lichtenegger, H., Delva, M, 2011, Exospheres and Energetic Neutral Atoms of Mars, Venus and Titan, Space Sci. Rev., pages 213-266

Gershman, D.J., Raines, J.M., Slavin, J.A., Zurbuchen, T.H., Anderson, B.J., Korth, H., Ho, G.C., Boardsen, S.A., Cassidy, T.A., Walsh, B.M., Solomon, S.C., 2015, MESSENGER observations of solar energetic electrons within Mercury's magnetosphere, J. Geophys. Res. Space Phys. 120, 8559–8571

Giomataris, Y.; Rebourgeard, P.; Robert, J.; Charpak, G., 1966, MICROMEGAS: A high-granularity position-sensitive gaseous detector for high particle-flux environments. Nucl. Instrum. Methods, 376, 29–35

Grignon, C., G. Bernard, J. Billard1, G. Bosson, O. Bourrion, O. Guillaudin, C. Koumeir, F. Mayet, D. Santos, P. Colas, E. Ferrer, I. Giomataris, A. Allaoua and L. Lebreton, 2009, A prototype of a directional detector for non-baryonic dark matter search: MIMAC (Micro-TPC Matrix of Chambers), Journal of Instrumentation, Vol. 4

Gronoff, G., Arras, P., Baraka, S., Bell, J. M., Cessateur, G., Cohen, O., et al., 2020, Atmospheric escape processes and planetary atmospheric evolution. J. Geophysi

Gruntman, M., 1997, Neutral Atom Imaging, Review of Scientific Instrum., 68 (10), 3617-3656

Hastings, D., & Garrett, H., 1996, The Ambient Space Environment, Cambridge Atmospheric and Space Science Series, pp. 44-99, Cambridge: Cambridge University Press

Hodges, R. R., 1994, Monte Carlo simulation of the terrestrial hydrogen exosphere, J. Geophys. Res., 99, 23,229– 23,247

Hunten, D. M., Morgan, T. H., & Shemansky, D. E., 1988, The Mercury atmosphere. Mercury, 562

Hunten, D. M., & Sprague, A. L., 2002, Diurnal variation of sodium and potassium at Mercury, Meteoritics & Planetary Science, 37(9), 1191-1195

Ip, W. H., 1986, The sodium exosphere and magnetosphere of Mercury. Geophysical research letters, 13(5), 423-426

Ip, W. H., 1993, On the surface sputtering effects of magnetospheric charged particles at Mercury, Astrophys. J. 418, 451–456

Janches, D., Berezhnoy, A. A., Christou, A. A., et al., 2021, Meteoroids as one of the sources for exosphere formation on airless bodies in the inner solar system, Space Science Reviews, 217, 1-41

Jasinski, J. M., Regoli, L. H., Cassidy, T. A., Dewey, R. M., Raines, J. M., Slavin, et al., 2020, A transient enhancement of Mercury's exosphere at

extremely high altitudes inferred from pickup ions, Nature Communications, 11(1), 4350

Kalvas T., 2014, Beam Extraction and Transport, Department of Physics, University of Jyvaskyla

Kameda, S., Ikezawa, S., Sato, M., Kuwabara, M., Osada, N., Murakami, 2017, Ecliptic north-south symmetry of hydrogen geocorona, Geophysical Research Letters, 44(23), 11-706

Killen, R. M., Potter, A., Fitzsimmons, A. and Morgan, T. H., 1999, Sodium D2 line profiles: Clues to the temperature structure of Mercury's exosphere. Planet. Space Sci., 47, 1449–1458

Killen, R.M., Potter, A.E., Reiff, P., Sarantos, M., Jackson, B.V., Hick, P., Giles, B., 2001, Evidence of space weather at Mercury, J.Geophys.Res.106 (E9), 20509–20525

Killen, R. M., Sarantos, M., Potter, A. E., & Reiff, P., 2004, Source rates and ion recycling rates for Na and K in Mercury's atmosphere, Icarus, 171(1), 1-19

Killen, R. M., Bida, T. A., Morgan, T. H., 2005.The calcium exosphere of Mercury, Icarus, 173, 300–311

Killen, R. M. D. E., Shemansky, D., & Mouawad, N., 2009, Expected emission from Mercury's exospheric species, and their ultraviolet–visible signatures, The Astrophysical Journal Supplement Series, 181(2), 351

Killen, R.M., Potter, A.E., Vervack, R.J., Bradley, E.T., McClintock, W.E., Anderson, C.M., Burger, M.H, 2010, Observations of metallic species in Mercury's exosphere, Icarus 209, 75–87

Killen, R. M., and J. M. Hahn, 2015, Impact vaporization as a possible source of Mercury's calcium exosphere, Icarus, 250, 230–237

Killen, R. M., 2016, Pathways for energization of Ca in Mercury's exosphere, Icarus, 268, 32–36

Killen, R. M., Vervack, R.J., Burger, M. H., 2022, Updated Photon Scattering Coefficients (g-values) for Mercury's Exospheric Species, ApJS, 263, 37

Kivelson G. and Russell T., 1995, Introduction of Space Physics, University of Callifornia

Lammer, H., & Bauer, S. J., 1997, Mercury's exosphere: origin of surface sputtering and implications, Planetary and space science, 45(1), 73-79

Lavraud, B., E. Larroque, E. Budnik, V. Génot, J. Borovsky, M. Dunlop, C. Foullon, H. Hasegawa, C. Jacquey, K. Nykyri, A. Ruffenach, M. Taylor, I. Dandouras, and H. Rème, 2013, Asymmetry of magnetosheath flows and magnetopause shape during low Alfven Mach number solar wind, J. Geophys. Res.

Leblanc, F. and Johnson, R. E., 2003, Mercury's sodium exosphere, Icarus, 164, 261–281

Leblanc, F., Doressoundiram, A., Schneider, N., Mangano, V., López Ariste, A., Lemen, C., Gelly, B., Barbieri, C., Cremonese, G., 2008, High latitude peaks in Mercury's sodium exosphere: spectral signature using THEMIS solar telescope. Geophys. Res.Lett.35,18

Leblanc, F., Doressoundiram, A., Schneider, N., Massetti, S., Wedlund, M., López Ariste, A., Barbieri, C., Mangano,V., Cremonese, G., 2009, Short term variations of Mercury's Na exosphere observed with very high spectral resolution, Geophys. Res. Lett. 36, 7

Leblanc, F., Johnson, R.E., 2010, Mercury exosphere I. Global circulation model of its sodium component, Icarus 209,280–300

Lemaire, J. F. and Gringauz, K. I., 1998, The Earth's Plasmasphere, Cambridge University Press, Cambridge

Lindsay, B. G., & Stebbings, R. F., 2005, Charge transfer cross sections for energetic neutral atom data analysis, Journal of Geophysical Research: Space Physics, 110(A12)

Longmore, M., Schwartz, S. J., Geach, J., Cooling, B. M. A., Dandouras, I., Lucek, E. A., & Fazakerley, A. N., 2005, Dawn-dusk asymmetries and sub-Alfvenic flow in the high and low latitude magnetosheath, in Annales Geophysicae, Vol. 23, No. 10, pp. 3351-3364

Madey, T.E., Yakshinskiy, B.V., Ageev, V.N., Johnson, R.E., 1998, Desorption of alkali atoms and ions from oxide surfaces: relevance to origins of Na and K in atmospheres of Mercury and the Moon, J. Geophys. Res. 103, 5873–5887

Mangano, V., Leblanc, F., Barbieri, C., Massetti, S., Milillo, A., Cremonese, G. and Grava, C., 2009, Detection of a southern peak in Mercury's sodium exosphere with the TNG in 2005, Icarus, 201, 424–431

Mangano, V., Milillo, A., Mura, A., Orsini, S., De Angelis, E., Di Lellis, A. M., Wurz, P., 2007, The contribution of impulsive meteoritic impact vaporization to the Hermean exosphere, Planet. Space Sci., 55(11), 1541–1556

Mangano, V., Massetti, S., Milillo, A., Plainaki, C., Orsini, S., Rispoli, R., Leblanc, F., 2015, THEMIS Na exosphere observations of Mercury and their correlation with in-situ magnetic field measurements by MESSENGER, Planet. Space Sci. 115, 102–109

Marchi, S., Morbidelli, A., Cremonese, G., 2005, Flux of meteoroid impacts on Mercury, Astron. Astrophys. 431 (I. 3), 1123–1127

Massetti, S., Orsini, S., Milillo, A., Mura, A., DeAngelis, E., Lammer, H., Wurz, P., 2003, Mapping of the cusp plasma precipitation on the surface of Mercury, Icarus 166, 229–237

Massetti, S., Mangano, V., Milillo, A., Mura, A., Orsini, S., Plainaki, C., 2017, Short-term observations of double peaked Na emission from Mercury's exosphere, Geophys. Res. Lett. 44, 2970–2977

McClintock, W.E., Lankton, M.R., 2007, The Mercury atmospheric and surface composition spectrometer for the MESSENGER mission. Space Sci. Rev. 131 (1–4), 481–521

McClintock, W.E., Bradley, E.T., Vervack, R.J., Killen, R.M., Sprague, A.L., Izenberg, N.R., Solomon, S.C., 2008, Mercury's exosphere: observations during MESSENGER's first Mercury flyby. Science 321, 92

McClintock, W.E., Vervack, R.J., Bradley, E.T., Killen, R.M., Mouawad, N., Sprague, A.L., Burger, M.H., Solomon, S.C., Izenberg, N.R., 2009, Messenger observations of Mercury's exosphere: detection of magnesium and distribution of constituents. Science 324, 610–613

McComas, D. J., Allegrini, F., Bochsler, et al., 2009, Global observations of the interstellar interaction from the Interstellar Boundary Explorer (IBEX), Science, 326(5955), 959-962

McComas, D. J., Allegrini, F., Baldonado, J., Blake, B., Brandt, P. C., Burch, J., et al., 2009, The two wide-angle imaging neutral-atom spectrometers (TWINS) NASA mission-of-opportunity, Space Science Reviews, 142, 157-231

McIlwain, C. E., 1974, Substorm injection boundaries. In Magnetospheric physics: Proceedings of the advanced summer institute held at Sheffield, pp. 143-154

Meinel, A. B., 1951, Doppler-shifted auroral hydrogen emission, Astrophys. J., 113, 50

Merkel, A.W., Cassidy, T.A., Vervack, R.J., McClintock, W.E., Sarantos, M., Burger, M.H., Killen, R.M., 2017, Seasonal variations of Mercury's magnesium dayside exosphere from MESSENGER observations, Icarus 281, 46–54

Merkel, A.W., Vervack, J.R., Killen, R.M., Cassidy, T.A., McClintock, W.E., Nittler, L.R., Burger, M.H., 2018, Evidence of connection Mercury's magnesium exosphere to its magnesium-rich surface terrane, Geophys. Res. Lett. 45, 6790–6797

Merrill R.T. and McElhinny M.W., 1983, The Earth's Magnetic Field: Its History, Origin and Planetary Perspective, Academic Press, Vol. 401

Miles, P., 2015, Study of Mercury's Neutral Molecular Exosphere, PhD Dissertation, University of Texas at San Antonio

Milillo, A., Orsini, S., and Daglis, I. A., 2001, Empirical model of proton fluxes in the equatorial inner magnetosphere: 1. Development, J. Geophys. Res., 106, 25,713–25,730

Milillo, A., Orsini, S., and Daglis, I. A., 2003, Empirical model of proton fluxes in the equatorial inner magnetosphere: 2. Properties and applications, J. Geophys. Res., 108.

Milillo, S. Orsini, S., Mura, A., Massetti, S., 2004, Geomagnetic activity dependence of the inner magnetospheric proton distribution: An empirical approach for the 21–25 April 2001 storm, J. Geophys. Res., 111

Milillo, A., Orsini, S., Wurz, P., Delcourt, D., Kallio, E., Killen, R.M., Lammer, H., Massetti, S., Mura, A., Barabash , S., Cremonese, G., Daglis, I.A.,De Angelis, E., Di Lellis, A.M., Livi, S., Mangano, V., Torkar, K., 2005, Surface–exosphere–magnetosphere system of Mercury. SpaceSci.Rev. 117(3), 397–444

Milillo, A., et al., 2011, Empirical model of proton fluxes in the equatorial inner magnetosphere' Development, Journal of Geophysical Research

Milillo, A., Mangano, V., Massetti, S., Mura, A., Plainaki, C., 2021, Exospheric Na distributions along the Mercury orbit with the THEMIS telescope. Icarus, 355, 114179

Mitchell, D. G., et al., 1993, INCA: The ion neutral camera for energetic atom imaging of the Saturnian magnetosphere, Opt. Eng., 32, 3096

Mitchell, D. G., et al., 2000, High-Energy Neutral Atom (HENA) imager for the IMAGE mission, Space Sci. Rev., 91, 67–112

Moore, T. E., et al., 2000, The low-energy neutral atom imager for IMAGE, Space Sci. Rev., 91, 155–195

Moroni, M., Mura, A., Milillo, A., Plainaki, C., Mangano, V., Alberti, T., Andre, N, Aronica, A., De Angelis, E., Del Moro, D., Kazakov, A., Massetti, S., Orsini, S., Rispoli, R., Sordini, R., 2023, Micro-meteoroids impact vaporization as source for Ca and CaO exosphere along Mercury's orbit, Icarus, 401, 115616

Mura, A., Orsini, S., Milillo, A., Delcourt, D., Massetti, S., & De Angelis, E., 2005, Dayside H+ circulation at Mercury and neutral particle emission, Icarus, 175(2), 305-319

Mura, A., Milillo, A., Orsini, S., Massetti, S., 2007, Numerical and analytical model of Mercury's exosphere: dependence on surface and external conditions, Planet. Space Sci. 55, 1569–1583

Mura, A., Wurz, P., Lichtenegger, H.I.M., Schleicher, H., Lammer, H., Delcourt, D., Milillo, A., Orsini, S., Massetti, S., Khodachenko, M.L., 2009, The sodium exosphere of Mercury: comparison between observations during Mercury's transit and model results, Icarus 200, 1–11

Mura, A., 2012, Loss rates and time scales for sodium at Mercury, Planetary and Space Science, 63, 2-7

Mura, A., Plainaki, C., Milillo, A., Mangano, V., Alberti, T., Massetti, S., Orsini, S., Moroni, M., De Angelis, E., Rispoli, R., Sordini, R., 2023, The yearly variability of the sodium exosphere of Mercury: A toy model. Icarus, 394, 115441

Nesvorny, D., Jenniskens, P., Levison, H.F., Bottke, W.F., Vokrouhlicky, D., Gounelle, M., 2010, Cometary origin of the zodiacal cloud and carbonaceous micrometeorites. Implications for hot debris disks, Astrophys. J. 713, 816–836

Nesvorny, D., Janches, D., Vokrouhlicky, D., Pokorny, P., Bottke, W.F., Jenniskens, P., 2011a, Dynamical model for the zodiacal cloud and sporadic meteors, Astrophys. J. 743, 129

Orsini, S., I. A. Daglis, M. Candidi, K. C. Hsieh, S. Livi, and B. Wilken, 1994, Model calculation of energetic neutral atoms precipitating at low alti-

tudes, Journal of Geophysical Research, Vol. 99, pages 13,489-13,49J

Orsini, S., Cerulli-Irelli, P., Ma & M., Milillo, A., Baldetti, P., Bellucci, G., Candidi, M., Chionchio, G., Orfei, R., Livi, S., Daglis, I. A., Wilken, B., GiittIer, W., Curtis, C. C., Hsieh, K. C., Sabbagh, J., Flamini, E., Roelof, E. C., Chase, C. C., Grande M., 1998, Imaging Earth's Magnetosphere: Measuring Energy, Mass, and Direction of Energetic Neutral Atoms With the ISENA Instrument, Measurement Techniques for Space Plasmas: Fields; Geophys. Monograph. Vol. 102, ed. by J. E. Borovsky and R. F. Pfaff, AGU, Washington, DC

Orsini, S.,Milillo, A. and Mura, A., 2004, Modeling the time-evolving plasma in the inner magnetosphere: An empirical approach, J. Geophys. Res., 109

Orsini, S., et al, 2009, Prospects of Solar System environment observations by means of ENA detection, Advances in Geosciences, pp. 263-291

Orsini, S. et al. 2010 , SERENA: a suite of four instruments (ELENA, STROFIO, PICAM and MIPA) on board BepiColombo-MPO for particle detection in the Hermean Environment, BepiColombo Special Issue on Planetary and Space Science, 58, 166-181

Orsini, S., Mangano, V., Milillo, A., Plainaki, C., Mura, A., et al., 2018, Mercury sodium exospheric emission as a proxy for solar perturbations transit, Scientific reports, 8(1), 928

Plainaki C., Milillo A., Mura A., Orsini S., Cassidy T., 2010, Neutral particle release from Europa's surface, Icarus 210, 385-395

Plainaki, C., Mura, A., Milillo, A., Orsini, et al., 2017, Investigation of the possible effects of comet Encke's meteoroid stream on the Ca exosphere of Mercury, Journal of Geophysical Research: Planets, 122(6), 1217-1226

Pokorny, P., Sarantos, M., & Janches, D., 2017, Reconciling the dawn–dusk asymmetry in Mercury's exosphere with the micrometeoroid impact directionality, The Astrophysical Journal Letters, 842(2), L17

Pokorny, P., Sarantos, M., Janches, D., 2018, A comprehensive model of the meteoroid environment around Mercury, Astrophys. J. 863(1), 31

Pollock, C. J., et al., 2000, Medium-Energy Neutral Atom (MENA) imager for the IMAGE mission, Space Sci. Rev., 91, 113–154

Porubcan, V., L. Kornos, and I. P. Williams, 2006, The Taurid complex meteor showers and asteroids, Contrib. Astron. Obs. Skalnaté Pleso, 36, 103–117

Potter, A.E., Morgan, T.H., 1985, Discovery of sodium in the atmosphere of Mercury, Science 229, 651–653

Potter, A.E., Morgan, T.H., 1986, Potassium in the atmosphere of Mercury, Icarus, Vol. 67, Issue 2, 336-340

Potter, A. E., & Morgan, T., 1990, Evidence for magnetospheric effects on the sodium atmosphere of Mercury, Science, 248(4957), 835-838

Potter, A. E., 1995, Chemical sputtering could produce sodium vapor and ice on Mercury, Geophysical research letters, 22(23), 3289-3292

Potter, A. E., Killen, R. M. and Morgan, T. H., 1999, Rapid changes in the sodium exosphere of Mercury, Planet. Space Sci., 47, 1441–1448

Potter, A. E., Killen, R. M., & Morgan, T. H., 2002, The sodium tail of Mercury, Meteoritics & Planetary Science, 37(9), 1165-1172

Potter, A.E., Killen, R.M., Sarantos, M., 2006, Spatial distribution of sodium on Mercury, Icarus 181(1), 1–12

Potter, A. E., & Killen, R. M., 2008, Observations of the sodium tail of Mercury. Icarus, 194(1), 1-12

Raines, J. M., Gershman, D. J., Slavin, J. A., Zurbuchen, T. H., Korth, H., Anderson, B. J., & Solomon, S. C., 2014, Structure and dynamics of Mercury's magnetospheric cusp: MESSENGER measurements of protons and planetary ions, Journal of Geophysical Research: Space Physics, 119(8),

6587-6602

Raines, J. M., Dewey, R. M., Staudacher, 2022, Proton precipitation in Mercury's northern magnetospheric cusp, Journal of Geophysical Research: Space Physics, 127(11), e2022JA030397

Rangarajan G., 1989, Indices of geomagnetic activity, Geomagnetism 3: 323–384

Rinaldi G. and Mura A., 2011, Report to cross sections related to plasma-planetary atmosphere interaction processes

Rispoli R. et al., 2013, ELENA microchannel plate detector: absolute detection efficiency for low energy neutral atoms, Optical Engineering, 52(5)

Roelof, E. C., 1987, Energetic Neutral Atom image of a storm-time ring current. Geophys. Res. Lett., 14, 652-655

Safrankova, J., Nemecek, Z., Dusik, S., Prech, L., Sibeck, D. G., & Borodkova, N. N., 2002, The magnetopause shape and location: A comparison of the Interball and Geotail observations with models, Annales Geophysicae, Vol. 20, No. 3, pp. 301-309

Sandahl I., 2003, The cusp as a source of plasma for the magnetosphere, Adv Space Res 31:1195–1205

Sarantos, M., Killen, R. M., Sharma, A. S., & Slavin, J. A., 2008, Correlation between lunar prospector measurements and the lunar exosphere during passage through the Earth's magnetosphere, Geophys. Res. Lett, 35, L04105

Sarantos, M., Killen, R. M., Sharma, A. S., & Slavin, J. A., 2010, Sources of sodium in the lunar exosphere: Modeling using ground-based observations of sodium emission and spacecraft data of the plasma, Icarus, 205(2), 364-374

Schleicher, H., Widemann, G., Woehl, H., Berkefeld, T., Soltau, D., 2004, Detection of neutral sodium above Mercury during the transiton 2003 May 7, Astron. Astrophys, 425, 1119 -1124

Schmidt, C.A.,Wilson, J.K., Baumgardner, J., Mendillo, M., 2010, Orbital effects on Mercury's escaping sodium exosphere, Icarus 207,9–16

Schmidt, C. A., Baumgardner, J., Mendillo, M., & Wilson, J. K., 2012, Escape rates and variability constraints for high-energy sodium sources at Mercury, Journal of Geophysical Research: Space Physics, 117(A3)

Shklovsky, I. S.,1959, On hydrogen emission in the night glow. Planetary and Space Science, 1(1), 63– 65

Sigmund, P., 1969, Theory of sputtering. I. Sputtering yield of amorphous and polycrystalline targets, Physical review, 184(2), 383

Slavin, J.A., Holzer, R.E., 1981, Solar wind flow about the terrestrial planets, 1. Modeling bow shock position and shape, J. Geophys. Res. 86(A13), 11401–11418

Slavin, J. A., Tsurutani, B. T., Smith, E. J., Jones, D. E., & Sibeck, D. G., 1983, Average configuration of the distant ($<$ 220 Re) magnetotail: Initial ISEE-3 magnetic field results. Geophysical research letters, 10(10), 973-976

Smyth, W. H., 1986, Nature and variability of Mercury's sodium atmosphere, Nature, 323(6090), 696-699

Smyth, W.H., Marconi, M.L., 1995, Theoretical overview and modeling of the sodium and potassium atmospheres of Mercury, Astrophys. J. 441, 839–864

Snyder L. et al., 2017, Performance of a MICROMEGAS-based TPC in a high-energy neutron beam,The NIFFTE Collaboration

Solomon, S.C., McNuttJr., R.L., Gold, R.E., Domingue, D.L., 2007, MESSENGER mission overview, SpaceSci.Rev.131,3–39

Solomon, S. C., Nittler, L. R.,& Anderson, B. J., 2018, Mercury: The view after MESSENGER (Vol. 21), Cambridge University Press

Sprague, A.L., 1992, Mercury's atmospheric sodium bright spots and potassium variation: A possible cause, J. Geophys. Res. 97, 18257–18264

Sugiura, M., 1964, Hourly values of equatorial Dst for the IGY, Annals of the International Geophysical Year, 35: 945–9

Tsyganenko, N. A., and Andreeva, V.A., 2015, A forecasting model of the magnetosphere driven by an optimal solar wind coupling function, J. Geophys. Res.: Space Phys. 120, 8401–8425

Valek, P., Brandt, P. C., Buzulukova, N., Fok, M.-C., Goldstein, J., McComas, D. J., Perez, J. D., Roelof, E., and Skoug, R., 2010, Evolution of low-altitude and ring current ENA emissions from a moderate magnetospheric storm: Continuousand simultaneous TWINS observations,J. Geophys. Res.,115, A11209

Valiev, R.R., Berezhnoy, A.A., Minaev, B.F., Chernov, V.E., Cherepanov, V.N., 2016, Ab initio study of electronic states of astrophysically important molecules, Russ. Phys. J. 59, 536–543

Valiev, R.R, Berezhnoy, A.A., Sidorenko, A.D., Merzlikin, B.S., Cherepanov, V.N., 2017, Photolysis of metal oxides as a source of atoms in planetary exospheres, Planet. Space Sci., 145, 38–48

Vallat, C., Dandouras, I., C: son Brandt, P., DeMajistre, R., Mitchell, D. G., Roelof, E. C., et al., 2004, First comparisons of local ion measurements in the inner magnetosphere with energetic neutral atom magnetospheric image inversions: Cluster-CIS and IMAGE-HENA observations, Journal of Geophysical Research: Space Physics, 109

Vervack, Jr, R. J., McClintock, W. E., Killen, R. M., Sprague, A. L., Anderson, B. J., Burger, M. H., Bradley, E. T., Mouawad, N., Solomon, S. C., and Izenberg, N. R., 2010, Mercury's complex exosphere: Results from MESSENGER's third flyby, Science, 329, 672–675

Vervack Jr, R. J., Killen, R. M., McClintock, W. E., Merkel, A. W., Burger, M. H., Cassidy, T. A., & Sarantos, M., 2016, New discoveries from MESSENGER and insights into Mercury's exosphere. Geophysical Research

Letters, 43(22), 11-545

Vorburger, A., Wurz, P., Barabash, S., et al., 2012, Energetic neutral atom observations of magnetic anomalies on the lunar surface, Journal of Geophysical Research: Space Physics, 117(A7)

Vorburger, A., Wurz, P., Barabash, S., Wieser, M., Futaana, Y., Lue, C., Holmström, M., Bhardwaj, A., Dhanya, M.B., Asamura, K., 2013, Energetic neutral atom imaging of the lunar surface, J. Geophys. Res. 118, 3937–3945

Zoennchen, J. H., Nass, U., Lay, G., and Fahr, H. J., 2010, 3D geocoronal hydrogen density derived from TWINS Ly-α-data, Ann. Geophys., 28, 1221–1228

Zoennchen, J. H., Nass, U., and Fahr, H. J., 2015, Terrestrial exospheric hydrogen density distributions under solar minimum and solar maximum conditions observed by the TWINS stereo mission, Ann. Geophys., 33, 413–426

Zurbuchen, T.H., Raines, J.M., Gloeckler, G., Krimigis, S.M., Slavin, J.A., Patrick, L., Koehn, R.M., Killen, A.L., Sprague, R.L., McNutt Jr., Solomon, S.C., 2008, MESSENGER observations of the composition of Mercury's ionized exosphere and plasma environment. Science 321, 90–92

Wallace, L., Barth, C. A., Pearce, J. B., Kelly, K. K., Anderson, D. E., Jr., and W.G. Fastie, 1970, Mariner 5 measurements of the earth's Lyman alpha emission, J. Geophys. Res., 75, 3769

Weider, S. Z., et al., 2015, Evidence for geochemical terranes on Mercury: Global mapping of major elements with MESSENGER's X-Ray Spectrometer, Earth Planet. Sci. Lett., 416, 109–120

Wieser, M., Barabash, S., Futaana, Y., et al., 2010, First observation of a mini-magnetosphere above a lunar magnetic anomaly using energetic neutral atoms, Geophysical Research Letters, 37(5)

West, H. I., Buck, R. M., and Walton, J. R.,1973, Electron Pitch Angle Distributions throughout the Magnetosphere as Observed on Ogo 5. J. Geophys. Res. 78, 1064–1081

Whipple, F. L., 1940, Photographic meteor studies. III. The Taurid shower, Proceedings of the American Philosophical Society, 711-745

Wiza J.L., 1979, Micro-channel plate detectors, Nucl. Instr. Meth., 587-601

Wurz P, 2000, Detection of Energetic Neutral Atoms, Group for Space Research and Planetary Sciences,Bern

Wurz, P., Lammer, H., 2003. Monte Carlo simulation of Mercury's exosphere, Icarus 164 (1), 1–13

Wurz, P., Fatemi, S., Galli, A., Halekas, J., 2022, Particles and Photons as Drivers for Particle Release from the Surfaces of the Moon and Mercury, Space science reviews, 218(3), 10

Yakshinskiy, B.V., & Madey, T.E., 1999, Photon-stimulated desorption as a substantial source of sodium in the lunar atmosphere, Nature 400, 642–644

Yakshinskiy, B. V., & Madey, T. E., 2000, Desorption induced by electronic transitions of Na from SiO_2: Relevance to tenuous planetary atmospheres, Surface Science, 451(1-3), 160-165

Yakshinskiy, B. V., & Madey, T. E., 2004, Photon-stimulated desorption of Na from a lunar sample: Temperature-dependent effects, Icarus, 168(1), 53-59

Yamauchi, M., De Keyser, J., Parks, G., Oyama, S. I., Wurz, P., Abe, T., et al., 2022, Plasma-neutral gas interactions in various space environments: Assessment beyond simplified approximations as a Voyage 2050 theme. Experimental astronomy, 54(2-3), 521-559